FLOW-INDUCED VIBRATIONS

OF A ROTARY MIXING BLADE

FLOW-INDUCED VIBRATIONS
OF A ROTARY MIXING BLADE

By

IVAN VELJKOVIC, B. ENG.

A Thesis

Submitted to the School of Graduate Studies

in Partial Fulfilment of the Requirements

for the Degree

Master of Engineering

McMaster University

Hamilton, Ontario, Canada

MASTERS OF ENGINEERING (2001)
(Mechanical Engineering)

McMaster University
Hamilton, Ontario, Canada

TITLE: Flow-Induced Vibrations of a Rotary Mixing Blade

AUTHOR: Ivan Veljkovic, B. Eng. (University of Belgrade)

SUPERVISOR: Dr. D.S. Weaver

NUMBER OF PAGES: xvii, 138

Abstract

Bluff bodies immersed in a fluid stream are susceptible to flow-induced vibrations. Depending on the body dynamic characteristics and flow conditions, different types of flow-induced vibrations may occur. The failure of a blade in a large mixing vessel in a chemical plant raised the question of the response of a parabolic cross-section bluff body to the flow excitation. Experiments were conducted in a wind tunnel using two-dimensional "sectional" models. Models with parabolic, semi-elliptic and semi-circular cross-section were investigated. In the dynamic experiments, flow velocity was increased from 0 to 22 m\s, and the oscillating amplitude and wake response were monitored. Vortex-induced vibrations were observed with Strouhal numbers for parabolic and semi-circular cross-sections of 0.13 and 0.12, respectively. Steady lift force and fluid moment for different angles of attack were monitored in the static experiments. From these results, lift and moment coefficients were calculated. For the closed semi-circular cross-section, Reynolds number had a strong influence on the lift coefficient. With an increase in Reynolds number, the lift coefficient decreased. The largest difference was noted at an angle of attack α = 45°. In contrast, the open semi-circular model lift coefficient was independent of Reynolds number. In the experiments where the elastic

axis of the model coincided with the model centre of gravity, galloping was not observed in the plunge mode. When the model elastic axis was moved to a position 90 mm behind the test model centre of gravity, galloping was observed for the semi-elliptic and parabolic models. The onset of galloping coincided with the vortex-induced resonance. Changing the model elastic axis position introduced a combination of plunge and torsional motion, and latter is believed to be responsible for the existence of galloping. The parabolic model was modified in an attempt to eliminate galloping instability. Fins were added at the separation points to widen the wake and prevent the reattachment of the flow to the afterbody. With these changes, galloping was not observed, although the oscillation amplitudes remained unacceptably high.

The present investigation revealed previously unknown characteristics of semi-elliptical and parabolic cross-section bluff body behaviour in fluid flow. At the same time, it laid a foundation for the solution to the practical problem encountered when a parabolic cross-section bluff body was used as a mixing blade.

Acknowledgements

I wish to express my gratitude to my supervisor, Dr. D. S. Weaver, for his guidance and encouragement during these studies. I am extremely grateful for the opportunity to have been his graduate student.

It is with warm thoughts that I acknowledge my friends, mentors and peers in the FIV group, especially Dr. R. L. Judd, Dr. S. Ziada, Dr. M. Hassan and Dr. P. Feenstra. Their advice, insight and encouragement are sincerely appreciated.

I would like to thank the technicians in the Mechanical Engineering Department: Dave Schick, Ron Lodewyks, Joe Verhaeghe and Andrew Buyers for their invaluable knowledge and assistance.

I would also like to express my appreciation to the many individuals involved in McMaster University Graduate Programme for providing wonderful academic environment in which to learn, especially Dr. D. R. Metzger and Mrs. R. Clifford.

Lastly, I would like to thank to my parents Dusan and Lepojka Veljkovic, family, and, especially, my Kika, who always believed in my abilities and whose love and support were a constant source of renewal.

"Whatever does not cause pain – is not life,
whatever does not pass – is not joy."
Ivo Andric

Table of contents

List of figures

List of tables

Nomenclature

Symbol	Description	Unit
A	plunge rms amplitude	mm
A_r	rocking rms amplitude	mm
a	rms amplitude	V_{rms}
b	model depth	mm
C_L	lift coefficient	-
C_M	moment coefficient	-
C_y	lateral force lift coefficient	-
d	model characteristic width	mm
d'	corrected model characteristic width	mm
d_m	modified model characteristic width	mm
F_L	lift force	N
F_y	Aerodynamic force component in the y direction	N
f_n	natural frequency	Hz
f_v	vortex shedding frequency	Hz
K	model plunge stiffness	N/m
L	model length	mm

l_b	elastic beam length	mm
M	moment exerted on the body from the fluid force	Nm
m_{a1}	added mass, semi-circular mode	grams
m_{a2}	added mass, semi-elliptic & parabolic model	grams
m_c	semi-circle model mass	grams
m_e	semi-ellipse model mass	grams
m_p	parabola model mass	grams
R_e	Reynolds number	-
S_t	Strouhal number	-
V	flow velocity	m/s
V_r	reduced flow velocity	-
V_{rel}	relative flow velocity felt by the body in motion	m/s
$\dot{y}$	velocity of the vibrating body	m/s
α	angle of attack	°
β	damping = logarithmic decrement/(2π)	%
ρ_{air}	air density	kg\m^3
ξ_{fv}	flow velocity measurement error	%
ξ_{cta}	constant temperature anemometer error	%
ξ_{cp}	calibration error coming from the Pitot static pressure probe	%
ξ_{cB}	calibration error coming from the Baetz micromanometer resolution	%
ξ_v	error in the digital voltmeter read out	%

Chapter 1

Introduction

The drive, always present in industry, to acquire new manufacturing techniques and new technologies that would make products better and more affordable, often leads to the use of ideas that are not tested and validated in the scientific world. The result is often problems that may be both expensive to solve and potentially dangerous to people and the environment. Once a problem occurs, it may happen repeatedly if it is not thoroughly investigated and the solution is not based on sound engineering and scientific grounds.

One such problem located in a chemical plant presents the basis for this research. As a part of the production process, mixing of certain chemicals is required. The mixing takes place in a 10 m high cylindrical vessel (*1*), with a vertical cross section and vertically oriented mixing shaft (*2*) as shown in ***Figure 1.1***. The shaft is driven by an electrical motor through a gearbox and rotates counter-clock-wise, looking from the vessel top. Two different types of mixing devices (*3* and *4*) are attached to the shaft, each consisting of four blades.

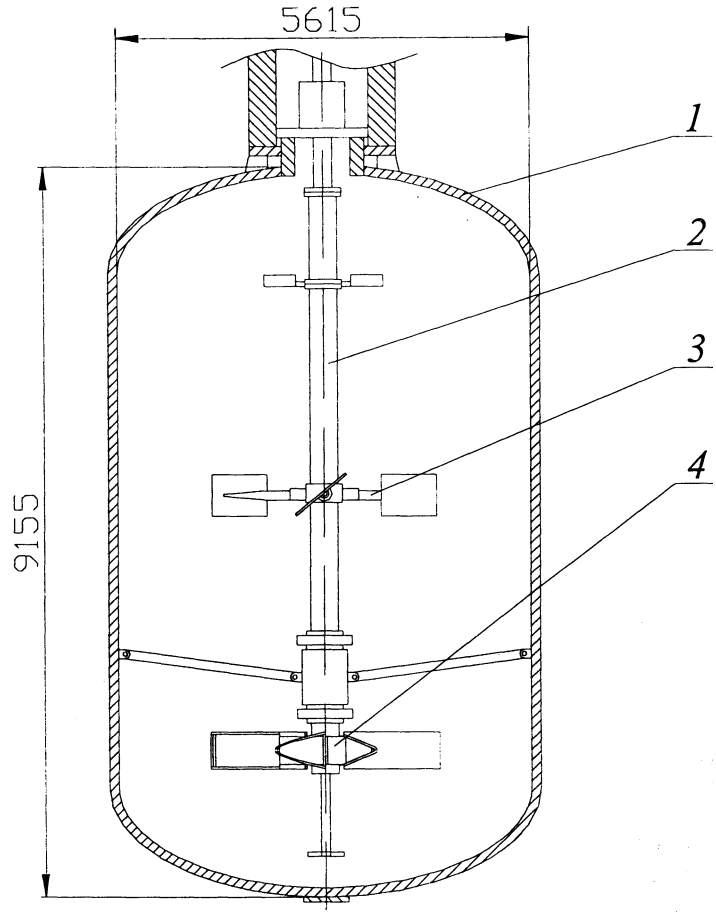

Figure 1.1

Vertical cross section of the mixing vessel with basic dimensions

1 – vessel, 2 – shaft, 3 – mixing device,

4 – mixing device with four blades having parabolic cross section

Prior to mixing, chemicals are filled from the top of the vessel. After filling the vessel, the shaft starts rotating and the blades begin to mix the components. As the mixing device (*3*) rotates, the blades push the fluid down towards the mixing device (*4*), which acts as centrifugal pump, driving the fluid further out and away from the vessel

centre. The fluid then follows the wall line up, and, at the top, becomes drawn down by the mixing blade (*3*) to the vessel centre, completing the cycle. Vertical baffles on the vessel wall, not shown in ***Figure 1.1***, make the mixing more efficient. When the mixing process is completed, the fluid is drawn out of the vessel to the next processing stage. Due to the corrosive nature of the chemicals in the mixing process, the vessel, shaft and blades are made of titanium.

After the vessel had been in use for a short period of time, one of the blades in the mixing device (*4*), ***Figure 1.1***, failed, causing the whole process to be shut down. When the vessel was opened, pieces of the blade were found at the bottom. Inspection showed that the failure starts as a crack at the end of the weld between the blade (*5*) and the supporting plate (*4*), from the points marked as ***"stress concentration points"*** in ***Figure 1.2***, and propagates down the back of the blade on both upper and lower side. When the blade structure is weakened to the point that it cannot withstand the combined dynamic and fluid forces, a breakage occurs. Only one of the four blades had actually broken off, but cracks at stress concentration points were found on the others, indicating that the same destructive process was taking place on all of the blades.

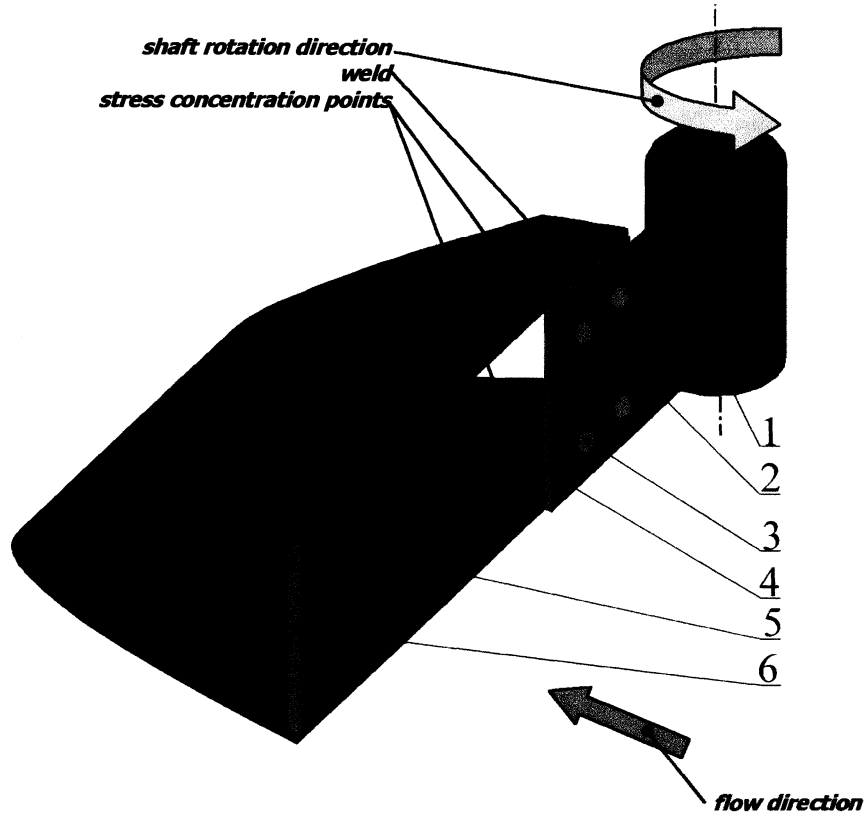

Figure 1.2

Schematic of the blade and shaft with rotation and flow direction indicated

1 – shaft, 2 – connecting plate, 3 –bolts holding supporting and connecting plates together,

4 – supporting plate, 5 – blade, 6 – supporting beam

Figure 1.2 presents the way the blade is attached to the shaft. The supporting plate (***4***) is welded full length to the upper and lover edge of the blade (***5***), acting as a stiffener. On the other side, the connecting plate (***2***) is welded to the shaft (***1***). The supporting and connecting plates are bolted together (***3***). The blade rotation and flow directions are also indicated in ***Figure 1.2***.

The midline of the blade cross section follows the parabolic equation:

$$x = 0.01365 \cdot y^2$$

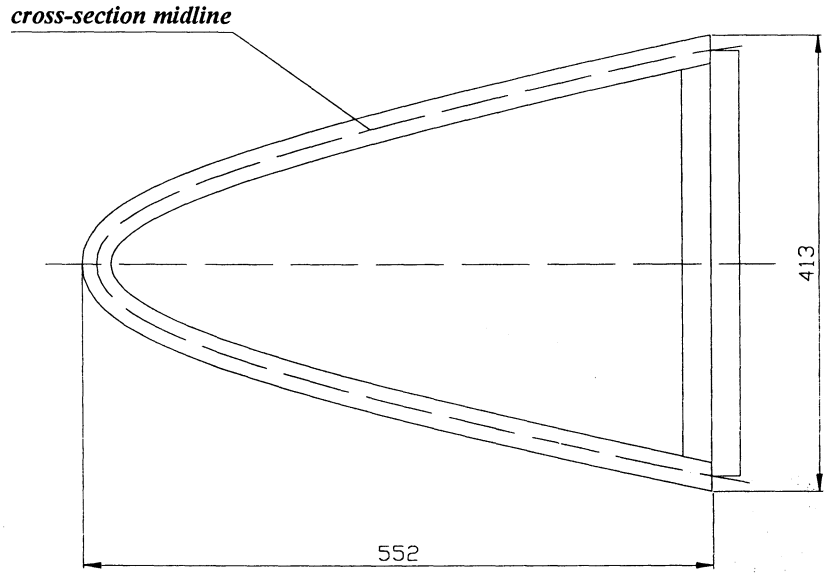

Figure 1.3

Mixing blade side view

The thickness of the parabolic cross-section blade is 12.7 mm. Blade technical drawings may be found in ***Appendix I.***

1.1 Motivation for the research

Structures in a flowing fluid, like the above mentioned blades, with well defined boundary layer separation points and a large after-body, represent a bluff body from an aerodynamics point of view. A flexible bluff body in the fluid stream may interact with the fluid and the energy from the flow may be transmitted to the body causing flow-induced vibrations. If the conditions are favourable, i.e. the body has light damping and the flow velocity reaches the critical value for galloping, or the vortex shedding frequency coincides with a natural frequency, the body will vibrate with a large amplitude which may cause structural failure at the weakest point.

The unexpected failure of the mixing blade raised the question of the susceptibility of a bluff body with a parabolic cross-section to flow induced vibrations. A parabolic shaped body in a fluid stream represents an unknown subject, as it has not been studied to date. Thus, it is worthwhile investigating its behaviour in fluid flow. There are at least two good reasons for such investigation. The first one is purely scientific – the investigation of the susceptibility of the parabolic cross-section body to vortex shedding and galloping phenomena increases our knowledge of flow-induced vibrations. The second reason is practical – to solve the problem that occurred in the actual mixing vessel and to propose a modified design of the blade in order to avoid future failures. These two aspects of the investigation, which relate the quest for knowledge with everyday industrial design, were the major motive for this thesis project.

1.2 Scope of the research

To learn more about bluff body behaviour in a fluid stream, experiments in the wind tunnel were conducted. The experimental set-up was designed to permit control over the dynamic characteristics of the model representing the bluff body. The flexibility of the model support allowed regulation of the model mode shapes and frequencies. Also, the support allowed model angle of attack adjustments from 0° to 180°. Three test models with a semi-circular, semi-elliptical and parabolic cross-section, were built. Since the semi-circular and parabolic models were modified, five different model layouts were tested. The tests were performed utilizing two-dimensional "sectional" principles.

The dynamic and static responses of the models to the flow excitation were monitored in the first group of the experiments. The first model to be tested was a closed semi-circular model. In the dynamic experiments, the model oscillating amplitude, frequency and wake response at different flow velocities were recorded. Fluid moment and lift force over the model angle of attack at several flow velocities were monitored in the static experiments. The results were compared against previously published results to verify the test set-up. The same experiments were repeated with the open semi-circular, semi-elliptic and parabolic cross-section models.

For the second group of experiments, the model mode shape was changed from a plain plunge to a combination of plunge and torsional motions. The coupling of the two modes was achieved by changing the model elastic axis position, relative to the centre of

gravity. Dynamic experiments were conducted on the open semi-circular, semi-elliptic and parabolic cross-section test models.

The focus of the third group of experiments was the parabolic model. Modifications to the cross-section were introduced to change the model dynamic response to the flow excitation.

The first part of this thesis explains the problem encountered in industry that brought attention to the behaviour of a bluff body with parabolic cross-section in fluid flow. An overview of the available literature on the response of bluff bodies with well defined separation points is discussed in ***Chapter 2***. The emphasis of the literature review is on the closed semi-circular cross-section. The experimental set-up is presented in ***Chapter 3***, including the model cross-sectional characteristics and the test set-up advantages and disadvantages. ***Chapter 4*** is focused on the experimental techniques used in this investigation. The experimental results are presented in ***Chapter 5***. Conclusions based on the experimental results together with the recommendations for future work are discussed in ***Chapter 6***.

Chapter 2

Literature Review

The presence of a solid body in a fluid stream deforms the fluid pattern adapting it to the body surface boundaries. The disturbed flow imposes forces on the solid body surface and if the body is elastic, vibrations may occur. With innovations in material science and structural design, modern engineering structures become lighter, thus increasing their susceptibility to fluid-structure interaction. The structural vibrations caused by the flowing fluid are called flow-induced vibrations and are encountered in many engineering fields, like marine structures, heat exchangers, pipelines, buildings and bridges. An extensive classification and explanation of all types of the fluid-structure interaction is presented in the book by Naudascher and Rockwell 1994.

The engineering structures of interest in this investigation are slender bluff bodies in a fluid stream. Parkinson (1989), defined a bluff body in steady flow: "a bluff section is understood to mean one from which the flow separates, producing two shear layers bounding a relatively broad wake, and steady incident flow is meant to rule out any organized transient or oscillatory character, although random turbulence may be

allowed". Depending on the cross-section geometry, separation points may be steady or fluctuating. An example of the former is a rectangular cross-section where the shear layers separate from the body at sharp edges. An example of the latter is a circular cross-section, where the separation points move along the body surface depending on the Reynolds number. The literature reviewed here is focused on flow-induced vibrations of bluff bodies with fixed separation points, as this is the focus of the present research. Since a bluff body may be susceptible to vortex-induced and galloping vibrations, these types of flow-induced vibrations are reviewed.

2.1 Vortex-induced vibrations

For a circular cylinder in a fluid stream, the fluid is forced to pass around the cylinder and, For Reynolds number grater than about 90, the boundary layers separate from each side of the cylinder surface near the widest section (Blevins, 1990). Alternating vortices are shed from each side of the cylinder, producing a regular wake called a von Karman vortex street. This periodic shedding of vortices produces a fluctuating lift force at the frequency of each vortex pair and smaller fluctuating drag force at twice this frequency. Usually, the bluff body is an elastic structure with specific dynamic characteristics, such as mode shape, frequency, damping etc. When the frequency of the alternating vortices coincides with a structural natural, resonance occurs. When the body is in motion, it interacts with the fluid, organizing the flow structure across the body span, increasing the vortex shedding influence on the body, thus

increasing the oscillating amplitude. If the oscillating amplitude becomes sufficiently large, the structural motion dominates the fluid mechanics and the vortex shedding frequency remains constant at the oscillating body frequency. This interaction between the fluid and the body is called "lock-in" (Blevins, 1990; Weaver, 2000).

The Strouhal number, S_t, is used to relate the vortex shedding frequency, flow velocity and the cross-section shape characteristic (Bearman, 1984; Parkinson, 1989; Blevins, 1990):

$$S_t = \frac{f_v \cdot d}{V}$$

where: f_v – vortex shedding frequency

d – characteristic dimension of the cross-section

V – flow velocity

The Strouhal number is also dependent on the surface roughness, Reynolds number and, to lesser extent, to the turbulence level in the flow stream (Blevins, 1990).

Several principles are used to avoid vortex-induced vibrations in industry (Blevins, 1990). For the shapes with the known Strouhal number, a critical flow velocity that causes a coincidence between the vortex shedding and structural natural frequency may be calculated. Then, the characteristic dimension of the cross-section can be chosen to avoid frequency coincidence. If this approach is not acceptable, i.e. the Strouhal number is unknown or there is little flexibility in changing the structural shape or dimensions, the structural characteristics like damping, mass and stiffness, may be changed in order to

influence the dynamic response of the body. A change in the damping affects the body oscillating amplitude, consequently influencing the fluid-body interaction and minimizing the vortex-induced vibrations. The change in the structural mass or stiffness changes the natural frequencies and thereby changes the flow velocity necessary for coincidence of the vortex shedding and structural frequencies. Another method for reducing or eliminating vortex-induced vibrations is to reduce the correlation between vortices over the body span or to destroy the regular shedding of vortices. This may be achieved by aerodynamical changes to the body cross-section as shown in ***Figure 2.1***, (Blevins, 1990). The effectiveness or practicality of these devices is very much dependent on the particular application. Helical strakes are probably the most widely used in the wind engineering applications.

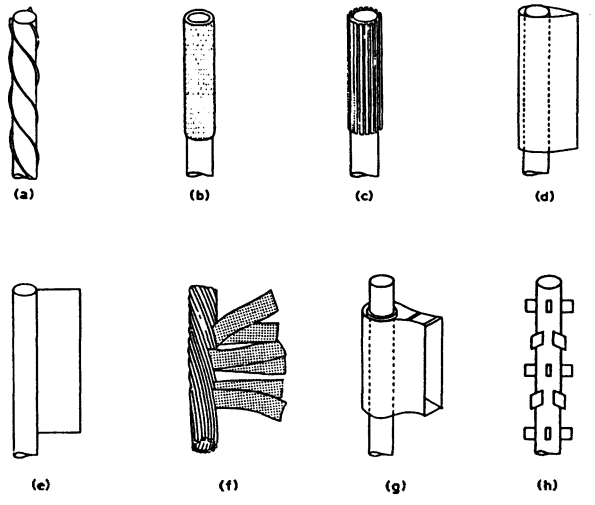

Figure 2.1

Add-on devices for suppression of vortex induced vibration of cylinders: (a) helical strake, (b) shroud, (c) axial slats, (d) streamlined fairing, (e) splitter, (f) ribboned cable, (g) pivoted guiding vane, (h) spoiler plates. From Blevins (1990)

2.2 Galloping

As opposed to vortex-induced vibrations, which are considered to be a case of resonance excitation, galloping is an instability phenomenon. When a bluff body is in a fluid stream, a fluid force is exerted on it. If the body moves transverse to the flow direction, the fluid force changes orientation too. When the body movement induces forces which are in the direction of the motion and in the phase with the body velocity, instability may occur. This type of instability is called galloping. Unlike vortex-induced vibrations, which may be caused in both circular and non-circular bluff bodies, galloping may be induced only in bodies with non-circular cross-section. Generally, instability in one degree-of-freedom systems is called galloping. In two degree-of-freedom systems, the modes may be aerodynamically coupled and the instability is referred to as flutter.

Parkinson and Brooks (1961) and Parkinson and Smith (1964) developed a procedure that predicts the onset of galloping. They measured the resultant of the lift and drag forces on a square prismatic body in the direction perpendicular to the flow. An aerodynamic force coefficient, C_y, in the direction of motion was calculated from the resultant and plotted as shown in ***Figure 2.2***. The obtained force coefficient values for different angles of attack were used to fit a seventh order polynomial, and den Hartog's criterion for the galloping of electric transmission lines, $\frac{\partial C_L}{\partial \alpha}$ (den Hartog, 1956), was

used in the form of $\frac{\partial C_y}{\partial \alpha}$. They suggested that a bluff body would be unstable when $\frac{\partial C_y}{\partial \alpha} > 0$.

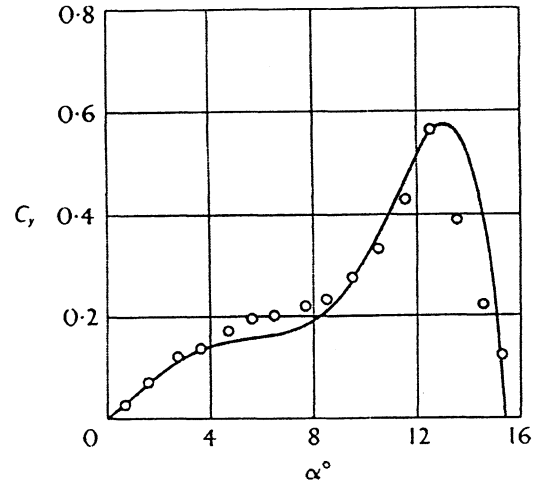

Figure 2.2

Lateral force coefficient plotted against angle of attack, Parkinson and Smith (1964)

The underlying assumption for this approach was that the excitation force, F_{yd}, acting on the bluff body experiencing galloping could be approximated with a static force, F_{sd}, measured in the wind tunnel on the stationary model. The angle α between the flow direction, V, and relative flow direction, V_{rel}, which is a result of the body motion, corresponds to the body inclination to the flow direction in the static experiments, as depicted in ***Figure 2.3***. This approach to galloping is known as the quasi-steady approach.

Blevins (1990) used the same approach, expressing the results in a form more useful to practicing engineers. The relation between the lift coefficient, C_L, and drag coefficient, C_D, of the bluff body to the lateral force coefficient, C_y, is:

$$a_1 = \frac{\partial C_y}{\partial \alpha} = -\left(\frac{\partial C_L}{\partial \alpha} + C_D\right)$$

Consequently, Blevins showed that as long as $\frac{\partial C_L}{\partial \alpha} + C_D > 0$, the body would not gallop.

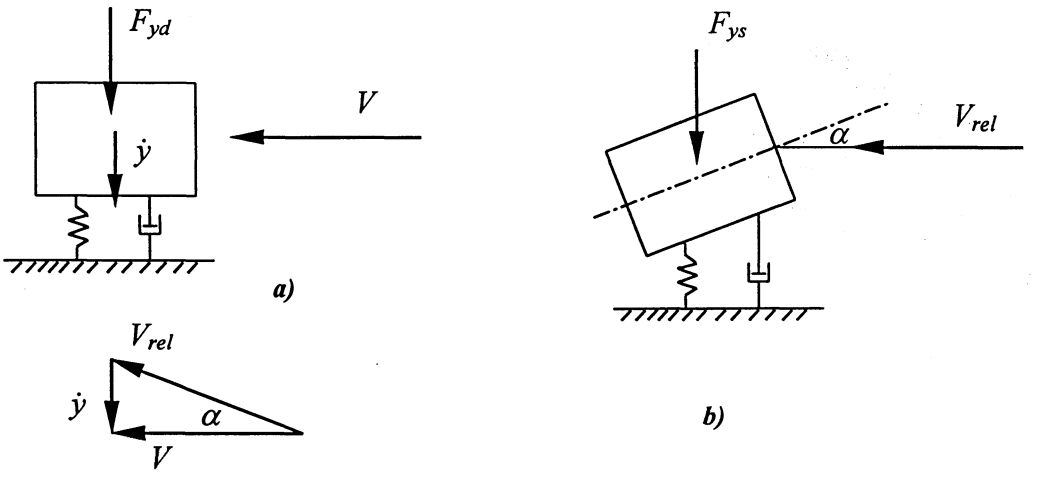

Figure 2.3

Schematic of the assumption of the quasi-steady approach

a) body in flow stream exhibiting galloping with excitation force, F_{yd}

b) static experiment on the body: force, F_{ys}, exerted on the body

Assumption of the quasi-steady approach: $F_{yd} \approx F_{ys}$

The square prism investigated by Parkinson and Smith (1964) is unstable since $\frac{\partial C_y}{\partial \alpha} > 0$ at zero angle of attack, and it would gallop from rest at sufficiently high flow velocities. Bodies that gallop from rest are classified as "soft" oscillators. In contrast, bodies that have $\frac{\partial C_y}{\partial \alpha} < 0$ at an angle of attack $\alpha = 0°$, and have a positive gradient of C_y with increasing angle of attack α, will gallop only if sufficient triggering amplitude exists at flow velocities exceeding the critical flow velocity. These bodies are called "hard" oscillators. Typical lateral force coefficients for rectangular cross-sections and corresponding types of the galloping responses are presented in ***Figure 2.4***.

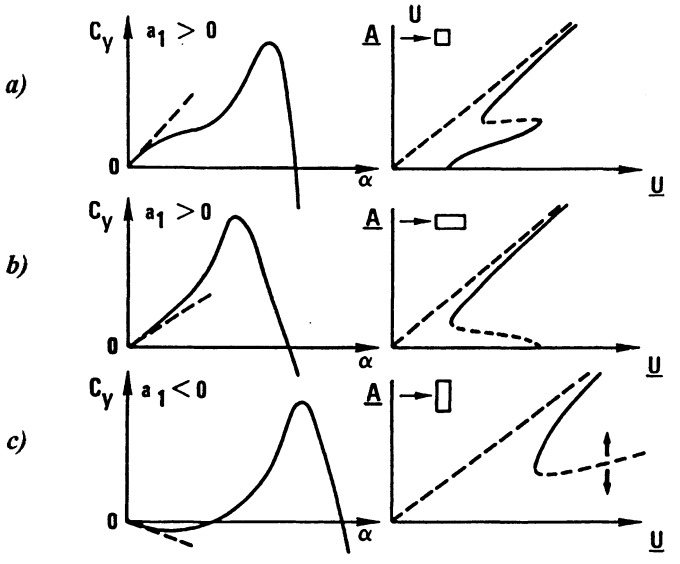

Figure 2.4

Three basic types of the lateral force coefficients and corresponding galloping response: a) soft oscillator, b) soft oscillator, c) hard oscillator, Blevins (1990), originally Novak (1972)

Another example of a hard oscillator is a body with a semi-circular cross-section. Novak and Tanaka (1974) investigated the behaviour of a semi-circular and two types of rectangular and cruciform cross-sections in the smooth and turbulent flows. The results of the semi-circular cross-section investigations are presented in ***Figures 2.5-2.8***.

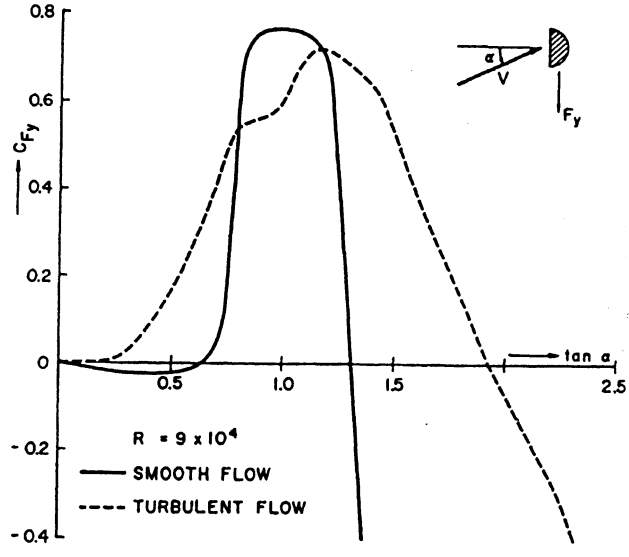

Figure 2.5

Lateral force coefficient in smooth and turbulent flows for semi circular cross-section, Novak and Tanaka (1974)

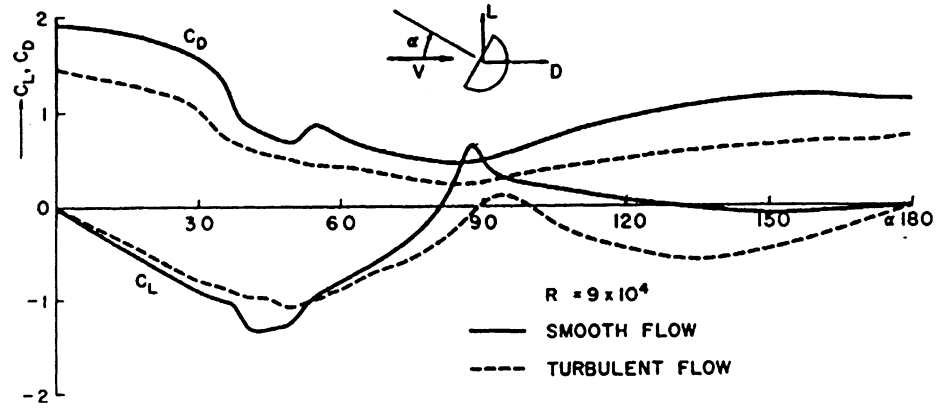

Figure 2.6

Lift and drag coefficients in smooth and turbulent flow for semi-circular cross-section, Novak and Tanaka (1974)

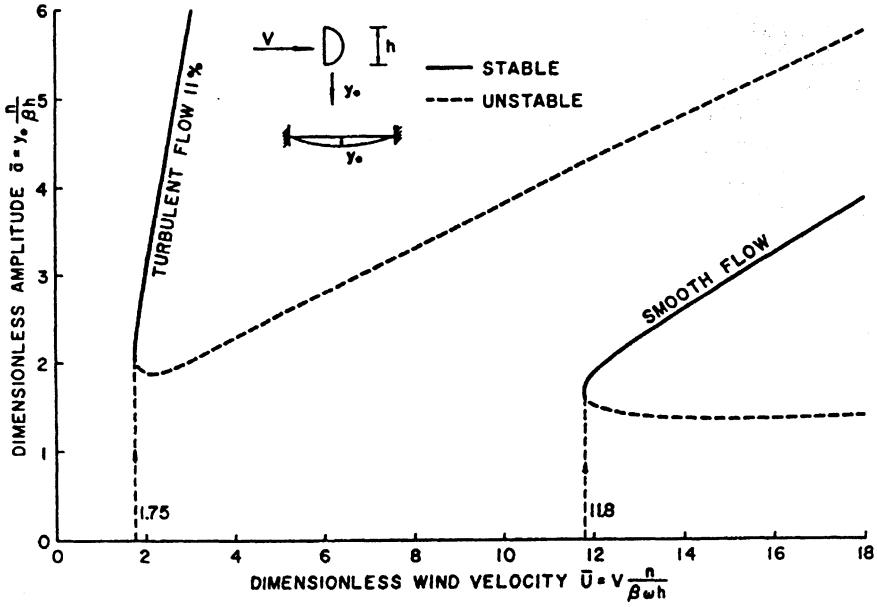

Figure 2.7

Galloping response curves in smooth and turbulent flow for semi-circular cross-section, Novak and Tanaka (1974)

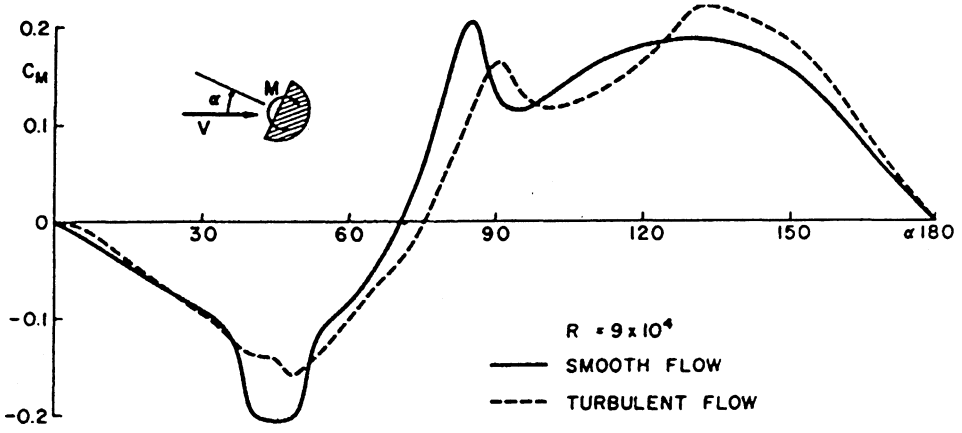

Figure 2.8

Moment coefficient in smooth and turbulent flow for semi-circular cross-section, Novak and Tanaka (1974)

The results for the semi-circular cross-section in smooth flow, ***Figure 2.6*** and ***Figure 2.8***, were particularly interesting, as experiments with the same cross-section were performed in the current investigation. A comparison between the results served as a verification for the experimental set-up and procedures (see later, ***Figure 5.4***).

The study by Novak and Tanaka (1974) was in agreement with the results from Parkinson and Brooks (1961), confirming that a body with semi-circular cross-section would not gallop from rest in neither smooth nor turbulent flows. The smooth and turbulent flows differed in critical flow velocity and triggering amplitude for the onset of galloping. A turbulence intensity of 11% in flow at $R_e = 9{\cdot}10^4$ significantly decreased critical flow velocity needed for the onset of galloping. According to Novak and Tanaka (1974), the critical reduced velocity of 11.8 for the smooth flow dropped to 1.75 in turbulent flow, while minimal dimensionless triggering amplitude slightly increased from

1.4 in smooth flow to 1.85 in turbulent flow (see ***Figure 2.7***). The same conclusion could be drawn from the lateral force coefficient diagram, ***Figure 2.5***, where the presence of turbulence in the flow significantly reduces the negative $\frac{\partial C_y}{\partial \alpha}$, and positive slope values are introduced at smaller angles of attack compared to smooth flow. Also, a significant influence of the Reynolds number on the lift and drag coefficients was noticed, but the difference between smooth and turbulence lift and drag coefficients did not change.

A rectangular cross-section with a 2/3 depth/height ratio was investigated in the same study. Responses to flow excitation with two different orientations of the rectangular section were examined. When the broader side was facing the flow, turbulence enhanced galloping, resulting in a slope of the lateral force coefficient of 0.75 at zero angle of attack. When the same model was rotated 90°, and the narrower side was facing the flow, turbulence increased model stability with a slope of the lateral force coefficient of 0 at zero angle of attack. The model with the cruciform cross-section was stable in both smooth and turbulent flows in this study.

Modi and Slater (1983; 1994) investigated the response to flow excitation of an angle section. The angle section is interesting because its elastic axis does not coincide with its centre of gravity. This may result in coupling between the plunge and torsional oscillations. The investigation was carried out in smooth flow with the Reynolds number range $2 \cdot 10^4$-10^5. The results from this static experiments are presented in ***Figure 2.9***, and include drag, lift and moment coefficient distribution as a function of angle of attack.

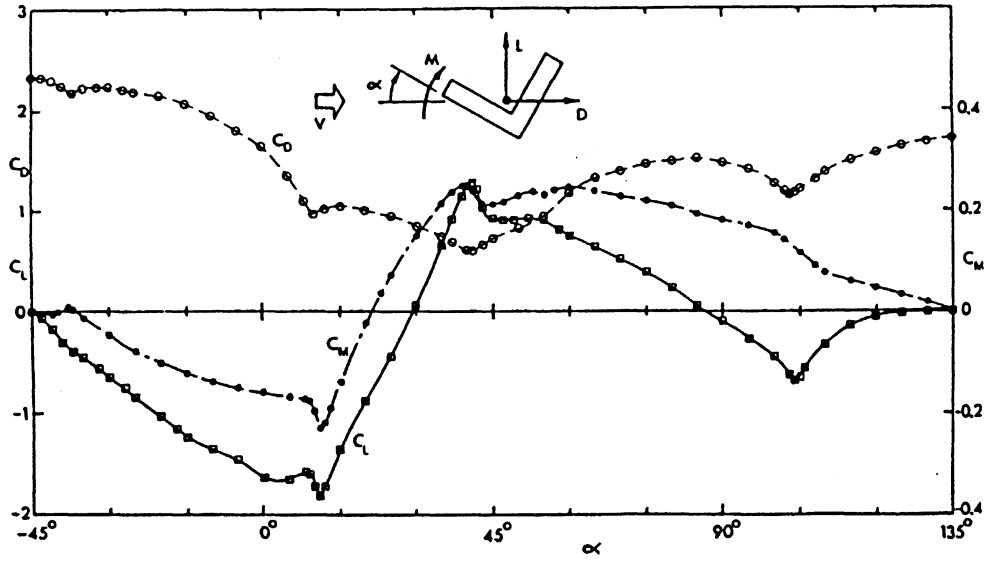

Figure 2.9

Distribution of steady lift, drag and moment coefficients, Modi and Slater (1994)

In contrast to the semi-circular cross-section with its flat side facing the flow (Novak and Tanaka, 1974), the angle section lift and drag coefficients did not depend on the Reynolds number. The Strouhal number for angle of attack α = - 45° (for angle section position see ***Figure 2.9***) was 0.16.

In their dynamic experiments, pure-plunge, pure-torsion and combined plunge-torsion responses were investigated. Galloping was not observed in the pure-plunge and pure-torsion experiments. While vortex-induced vibrations were present in both these experiments, a lock-in phenomenon was present only in the pure-plunge motion. Galloping was observed in coupled plunge-torsion motion. In the case of galloping with dominant plunge mode, plunge and rotation motions were in phase, while in the torsion dominant galloping response these two motions were out of phase. This observation

suggested that, depending on the dominant mode, coupled oscillations may be considered as a rotation around two different points. The coupled plunge-torsion with dominant plunge motion may be considered as a rotation around the point 30 characteristic lengths downstream of the model centre of gravity. Coupled plunge-torsion motion with dominant torsion motion may be approximated with rotation of the model around the point located just forward from the centroidal axis. The dynamic response of the coupled plunge-torsion motion arrangement to flow excitation is shown in the ***Figure 2.10***. Observations made by Modi and Slater (1994) were used as a basis for the experiments in the current research where elastic axis position was changed.

Modi and Slater (1994) used two different damping values for their experiments with dominant plunge motion. As a result, galloping occurred at different reduced velocities. For lower damping value in the plunge mode β_y = 0.002375, galloping coincided with vortex resonance, as presented in ***Figure 2.10a***. For higher damping value in the plunge mode β_y = 0.004125, vortex shedding resonance and galloping were significantly separated, as shown in ***Figure 2.10b***. Hysteretic response was observed for the galloping instability. Other dynamic parameters, such as dimensionless mass parameter n_y, dimensionless mass moment of inertia parameter n_θ and dimensionless damping parameterβ_θ for torsional support set-up were constant.

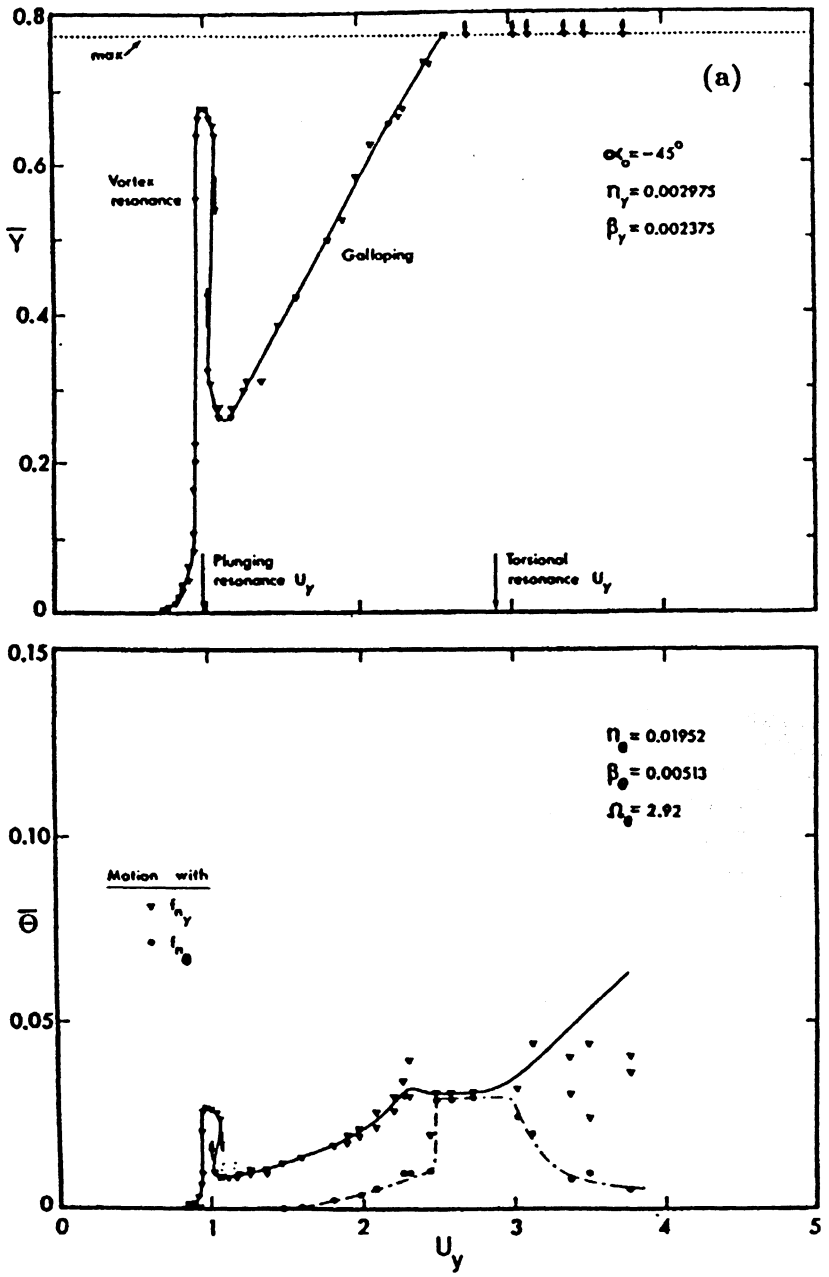

Figure 2.10 a)

Displacement measurements for model angle of attack $\alpha = -45°$ with combined plunge and torsion degrees-of-freedom, damping $\beta_y = 0.002375$, Modi and Slater (1994)

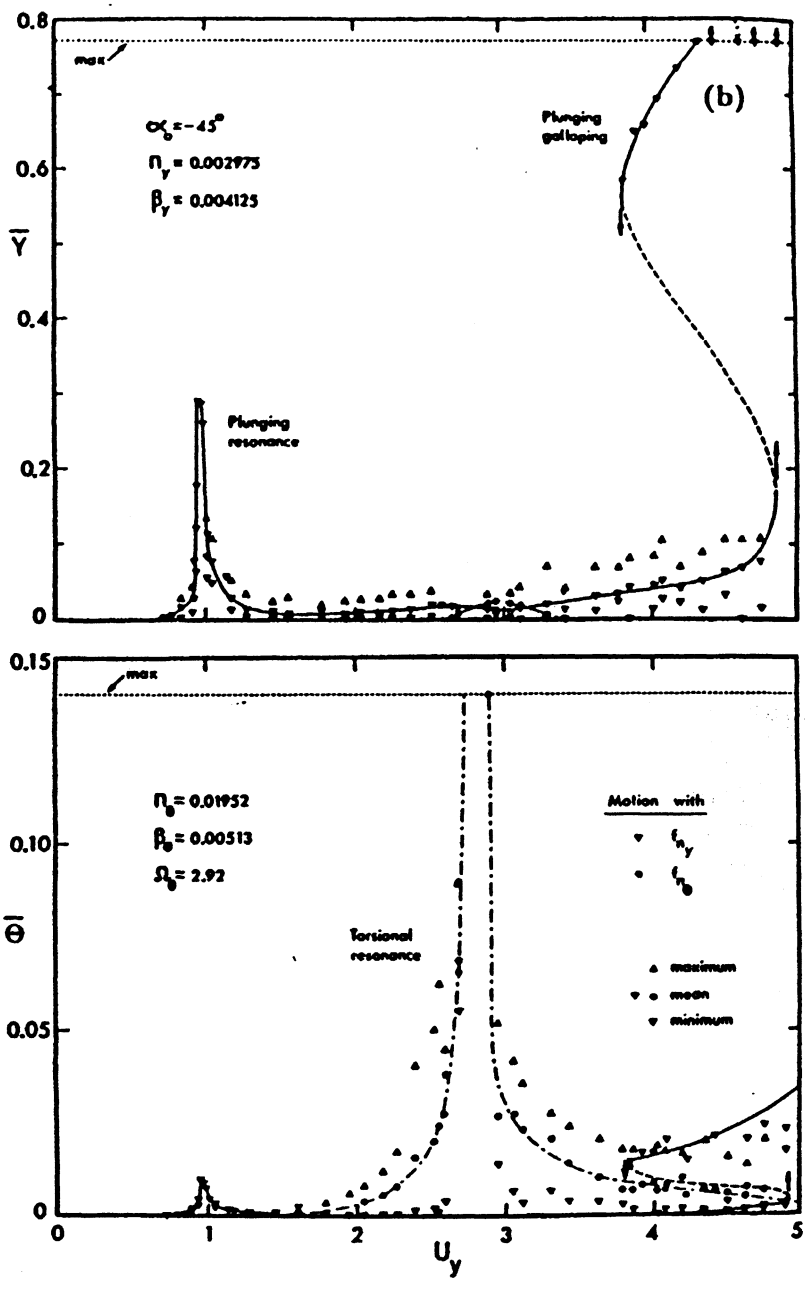

Figure 2.10 b)

Displacement measurements for model angle of attack α = - 45 ° with combined plunge and torsion degrees-of-freedom, damping β_y = 0.004125, Modi and Slater (1994)

The quasi-steady approach used to model galloping has been proven to give good results with some limitations (Parkinson and Smith, 1964; Novak and Tanaka, 1974; Modi and Slater 1994). The assumption that there is no phase difference between the body oscillations and the excitation fluid force is the major limitation. It dictates that galloping is the most powerful phenomenon that influences the body response. Therefore, the quasi-steady approach would give poor predictions in the presence of vortex shedding. Vortex induced vibrations are separated from galloping for reduced velocities 20 and higher (Blevins, 1990). Also, turbulence significantly influences the galloping response to flow excitation (Novak and Davenport, 1970; Novak and Tanaka, 1974; Bokaian and Geoola, 1984).

Although there have been attempts to theoretically model combined vortex induced and galloping vibrations of a bluff body and predict its response to flow excitation, (Corless and Parkinson, 1988), Blevins (1990) recommends conducting experimental research in a wind tunnel. The experimental approach to this complex flow influence on a bluff body broadens our understanding of the flow excitation phenomena, in term of both physical insights and practical application.

Chapter 3

Experimental set-up

One of the characteristics of the problem presented in ***Chapter 1*** is the high three-dimensionality of the investigated structure. The flow velocity felt by the blades increases with distance from the rotation axis. The blade cross-section is non-uniform and has a complex dynamic response, which is not easy to model.

Prior to this investigation, a group of forth year students at McMaster University conducted experiments using the same cross-sections that were used in current research. These models were supported at one side only and, as a result, the first mode of the model was a combined plunge and warping motion at same frequency. Thus, introducing three-dimensionality into the experimental set-up resulted in poor control of the experiments and finally destroyed the models.

Based on conclusions from the above mentioned experiments, a decision was made to build a two-dimensional, "sectional", model, having full control of the model behaviour.

3.1 Wind tunnel

Experiments were conducted in the open-circuit wind tunnel located in the John Hodgins Engineering Building at McMaster University. The wind tunnel is approximately 10.5 meters long, with a 1.1 m diameter fan and motor located at the downstream end. Air is drawn from the room through the tunnel inlet, having an octagonal cross-section with 1.22 m between parallel sides. At the tunnel entrance, before entering the contraction connected to the test section, air passes through a honeycomb and screen. With this flow arrangement, the upstream turbulence intensity is less a 1% for the flow velocity range from 2 m/s to 30 m/s, which is the velocity limit within an empty test section.

3.2 Test section

Fluid enters the test section through the contraction. The test section also has an octagonal cross-section with 620 mm between parallel sides. It is 2 m long and consists of three parts. The upstream and downstream parts of the test section are 650 mm long and are integrated into the wind tunnel structure. The central part of the test section is 700 mm long and is removable. The test section used in this investigation is constructed of eight 19mm-thick acrylic plates, the edges of which are bevelled and bolted together to form octagonal cross-section.

3.3 Test models

One of the most important model characteristics is its cross-section dimension perpendicular to the flow, i.e. characteristic length *d*. *d* influences several experimental parameters, such as vortex shedding frequency and test section blockage ratio.

The test section blockage is the ratio between characteristic length *d* and test section distance between parallel plates. This dimension presents the starting point for the model dimension choice. In the test section, the model presents an obstacle, which the flow must pass. If the obstacle dimensions are too large, flow deviations produced by the tunnel walls may significantly influence the test results. There is a general recommendation that the blockage of the test section should be 10 % or less.

Since the distance between parallel sides of the test section is 620 mm, in order to follow the above recommendation, the model characteristic dimension *d* of 62 mm was chosen for this investigation.

The model length *L* was 560 mm, leaving 30 mm between each side of the model and the test section wall. The purpose of this gap, together with endplates (see paragraph ***3.5***), was to ensure the two-dimensionality of the flow across the model and avoid wind tunnel boundary layer effect.

As presented in ***Chapter 1***, the structure of interest has a parabolic cross-section. The parabolic shape of the model cross-section was a replica of the blade outer line, with a 1 : 6⅔ scale.

Additional models with a semi-circular and semi-elliptic cross-section were built, both having the same characteristic width. Cross-sections of the models are shown in *Figure 3.1*.

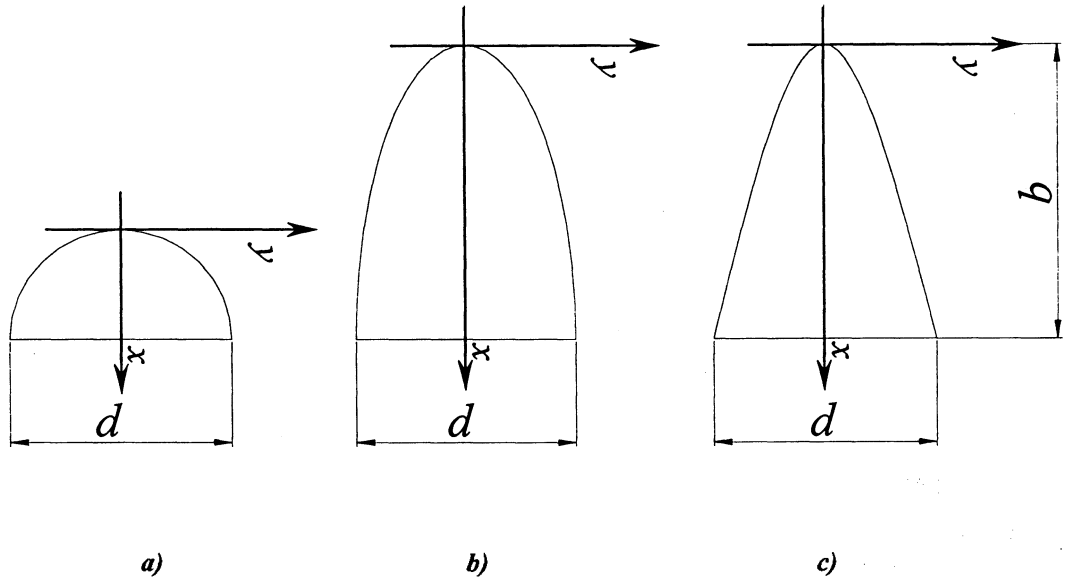

a) *b)* *c)*

Figure 3.1

Model cross-sections with dimensions and coordinate system

a) semi-circular, b) semi-elliptical, c) parabolic

The parabolic model follows the equation:

$$(x - 83) = 0.0864\, y^2,$$

The semi-circular model follows the equation:

$$(x - 31)^2 + y^2 = (31)^2,$$

Semi-elliptical model follows the equation:

$$\frac{(x-83)^2}{(83)^2}+\frac{y^2}{(31)^2}=1,$$

where 83 mm was the model depth b of the parabolic and semi-elliptical models. The semi-circular model, as a result of the circular shape, had 31 mm model depth.

These equations were used in the model manufacturing.

Figure 3.2 shows a photograph of the three models.

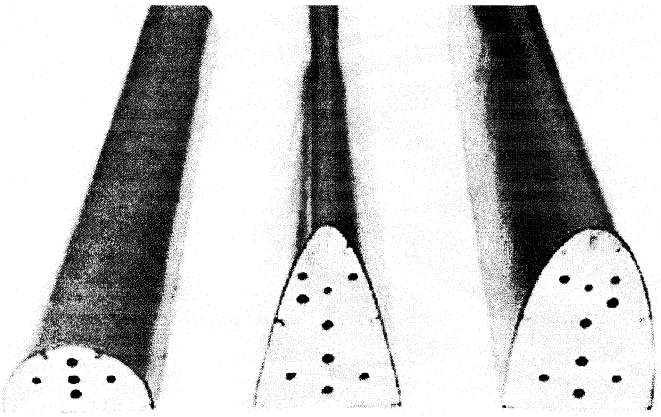

Figure 3.2

Photograph of the models

From left to right: semi-circular, parabolic and semi-elliptical model

During the design and manufacturing of the models, special care was taken of the following:

- model cross-section shape
- model weight
- after-body surface quality

Supporting ribs (*3*), ***Figure 3.3***, were the elements that determined the *model cross-section shape*. They were manufactured on the CNC machine where high accuracy can be achieved. Model shapes closely followed the mathematical equation, the lines were smooth and the models were perfectly symmetrical.

The next step was to cut grooves in the supporting ribs, which would house the struts (*2*). Subsequently, the supporting ribs were positioned in the jig and struts were glued to the ribs forming the skeleton of the model. 12-hour epoxy was used as glue.

As a following step, glue was applied onto surface where contact between the skin and skeleton would occur. The skin (*1*) came as a sheet of 3-layer, less than 1 mm thick, plywood with great ability to bend without breaking. Resistance to cracking was increased when the material was soaked in hot water. The soaked sheet of plywood was then pressed against the model skeleton and pressure was applied until glue dried. Heat was applied simultaneously, permanently deforming the sheet into the desired shape. Cracking of the skin was possible especially in the parabolic model, which had a very small tip radius. This was avoided by the combined application of humidity, pressure and heat.

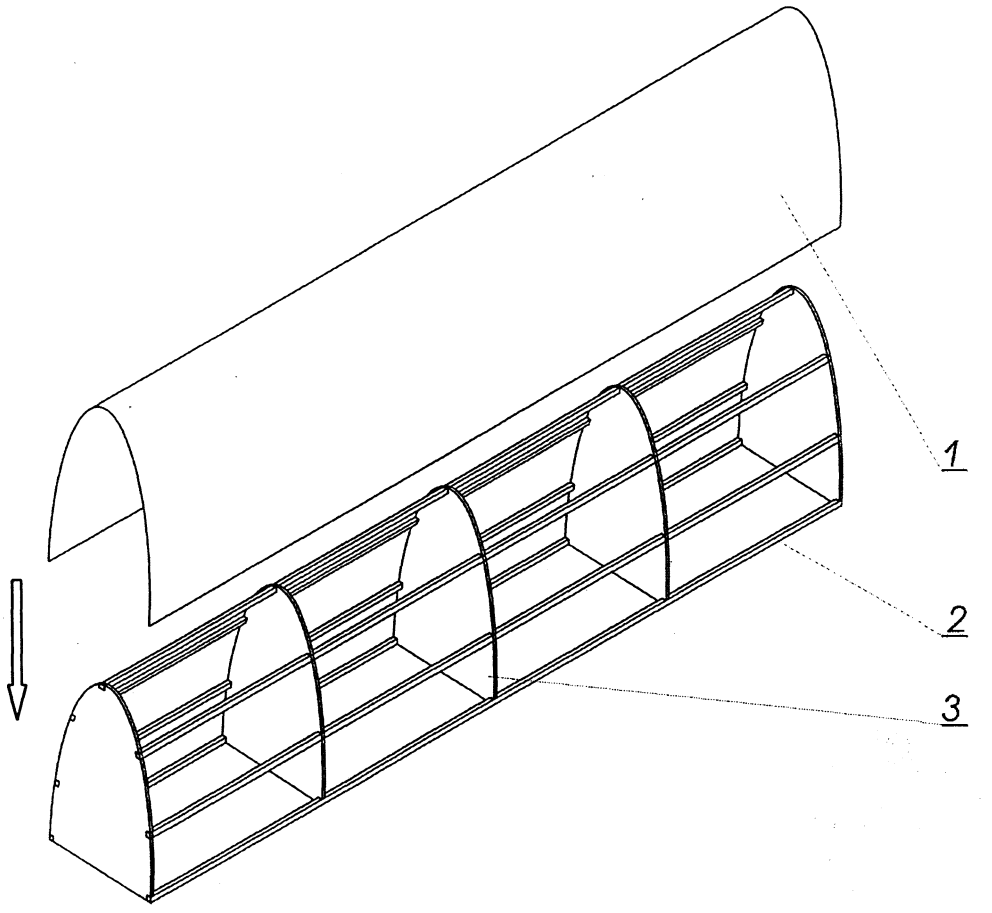

Figure 3.3

Schematic view of the model structure

1 – skin, 2 – struts, 3 – supporting ribs

4.5 mm 5-layer plywood was used as the material for supporting ribs. Rectangular 2x4 mm birch stripes were used for struts. The actual structure of the model is shown in *Figure 3.4*.

This model design provided a strong but light structure. *Model weight* has a direct impact on the dynamic response of the model. Thus, plywood was chosen as the model structure material. Also, handling wood is much easier than working with other materials, such as metal or plastic. Test set-up part masses are presented in ***Appendix II***.

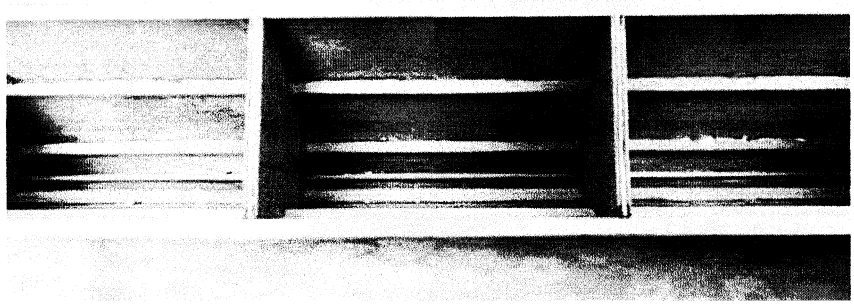

Figure 3.4

Photograph of the model segment

After-body surface finish was another very important model characteristic. Slight irregularities in the after-body surface could affect the aerodynamic loading and therefore adversely affect the model behaviour. A wrinkle-free skin surface was achieved by deforming the skin as explained above. The final step was to accomplish an almost mirror-like after-body surface finish. Three layers of airplane dope were applied to the model skin. Except for the last layer, the surface was smoothed with very fine sand paper, thus achieving a very smooth surface.

3.4 Parabolic cross-section model geometry modification

In the attempt to improve parabolic cross-section model dynamic response to the fluid excitation (see ***Chapter 5***), thus to improve the stability of the mixing blade, changes in the cross section were introduced.

Cross-section modifications introduced fins at the model separation points. Fins were perpendicular to the flow direction and had dimensions of 0.1 *d* and 0.2 *d*.

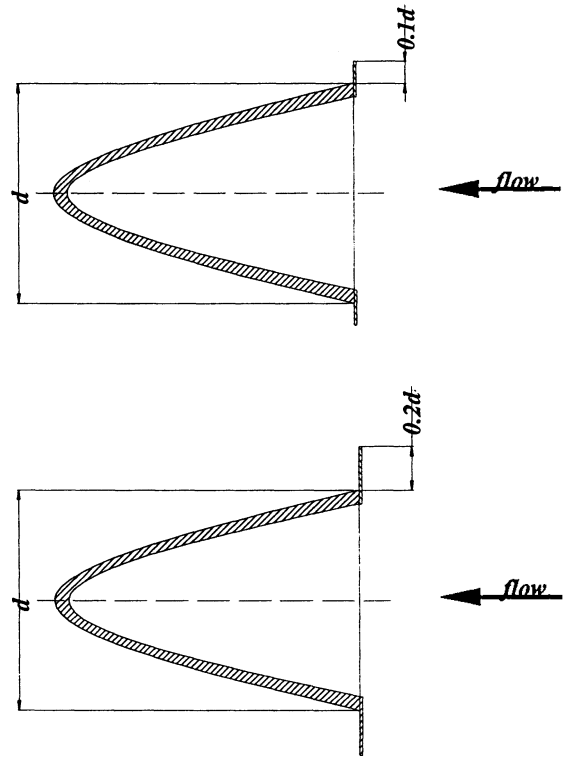

Figure 3.5

Parabolic cross-section modifications

Summary of cross-section shapes with applied modifications used in this investigation is depicted in ***Figure 3.6***.

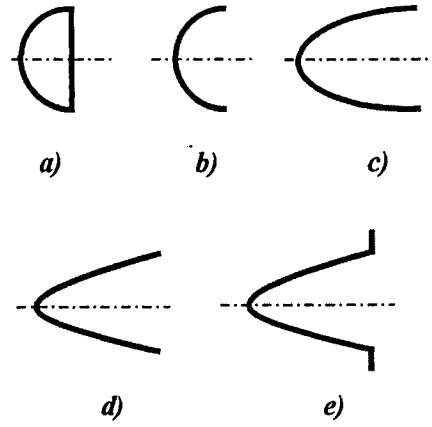

Figure 3.6

The model cross-sections used in the experiments

a) closed semi-circular, b) open semi-circular, c) semi-elliptical,

d) parabolic, e) modified parabolic

3.5 Endplates

Several scientists (Stansby, 1974; Kubo et al., 1989) suggested the use of endplates in order to preserve two-dimensional flow across the model.

Disturbance of the flow in the test section comes from the test model itself and from the test section wall boundary layers. Test section wall boundary layer disruption is unwanted influence on the rest of the flow. Separation of this flow region from the flow

across the test model is achieved by endplates. Kubo et al. (1989) recommended circular endplates with a diameter larger than 8.5 *d*, but this is not practical in the present study. Following the literature recommendation and accommodating the limitations of the test facility, it was decided to use endplates with 3.5 *d* diameter. The leading and trailing edges of the endplates were rounded for better flow separation, while the top and bottom were flattened to prevent interference with octagonal tunnel walls as shown in ***Figure 3.7***.

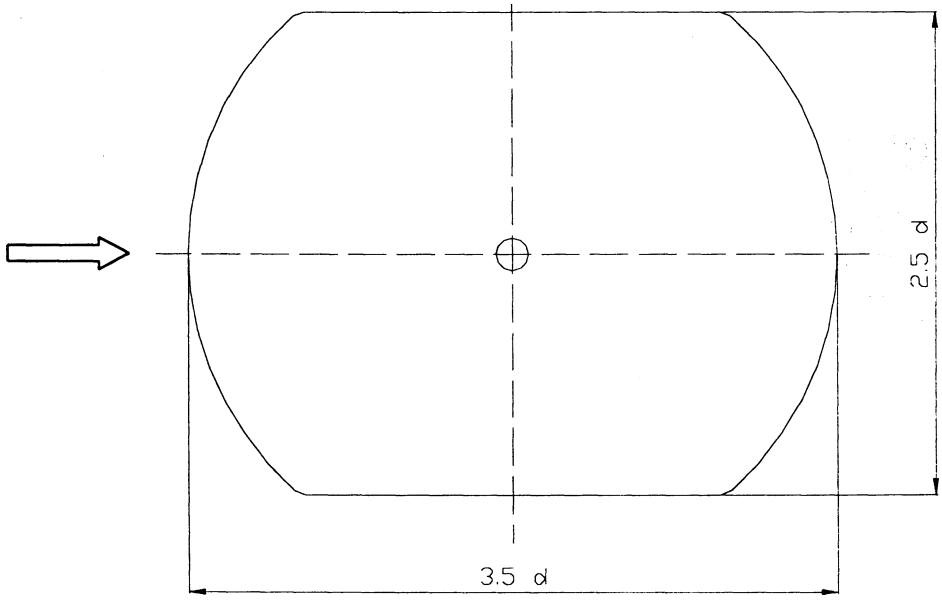

Figure 3.7

Endplate schematic view with dimensions and flow direction

The endplates were made from 3mm-thick balsa wood sheet. Since balsa wood is a very weak material, the endplate central region was strengthened with a glued patch of the 1mm-thick plywood, also used for the model skin. This reinforcement helped to prevent endplate bending and deterioration.

3.6 Supports

The design of the support structure significantly influences model response to the excitation, as well as response detection and results interpretation. The supports for the planned experiments in this investigation were flexible in the vertical direction, allowing natural mode and frequency control, and at the same time rigid in the stream wise direction, to avoid any unwanted motion.

Referring to ***Figure 3.8***, connecting rods (*4*) were fixed to the model endplates (*2*) and passed through the test-section walls to support bar (*5*). The connecting rods (*4*) were designed in a way that, when bolts are tightened, no relative rotation was possible between the model (*1*), the connecting rod (*4*) and the support bar (*5*). The aluminum support bars (*5*) had a box cross-section, which was perforated so that it was both stiff and as light as possible. While manufacturing the support bars, special care was taken to make them as light and stiff as possible. They were made from the 19 mm square, 3 mm thick aluminium tubing. The tubing was drilled on all sides, and the connecting rods were hollowed in order to minimize mass.

Prior to the beginning of an experiment, the model angle of attack could be adjusted using the protractor (**3**). The support bars (*5*) were connected to rigid supports (*6*), using two elastic beams (*8*) made from high quality spring steel, which permitted significant vertical deflection without plastic deformation.

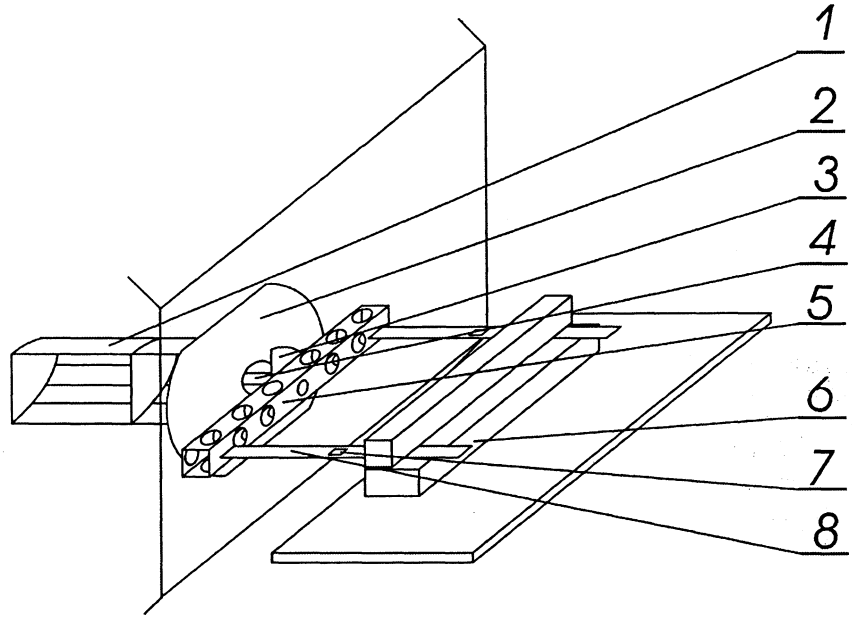

Figure 3.8

Schematic view of the model support

1 – test model, 2 – endplate, 3 – protractor, 4 – connecting rod,

5 – supporting bar, 6 – rigid support, 7 – strain gauge, 8 – elastic beam

The orientation of the beams enabled high stiffness in the drag direction while permitting motion in the lift direction. The dimensions of the beam (*8*) cross-section were chosen to withstand vertical deflections of 0.3 d without damage. The design of the

supports also enabled the beam (***8***) length to be changed, thereby permitting control of the natural frequency and the position of the elastic axis relative to the centre of gravity of the model.

The beam length could be changed from 63 mm to 120 mm. The beams were 0.635 mm thick and 15 mm wide, and they were clamped on both ends.

Test model response to the flow excitation was detected using strain gauges (*7*) that were glued to the surface of the beams (***8***). The strain gauges were positioned on the upper surface in the middle of the beam, 59 mm from the supporting bar clamp device edge. This was 4 mm from the rigid support edge, when the beam length was 63 mm (at its shortest). This arrangement permitted the greatest sensitivity for measuring element response.

Since the rigid parts of the support (*6*) do not affect the model mass, they were made of the solid steel components. This also served to minimize the transmission of vibrations between the model and the environment. The rigid supports (*6*) could be translated horizontally away from the model, thus changing the length of the beams and thereby lowering the model natural frequency.

Figure 3.9 shows the actual support structure.

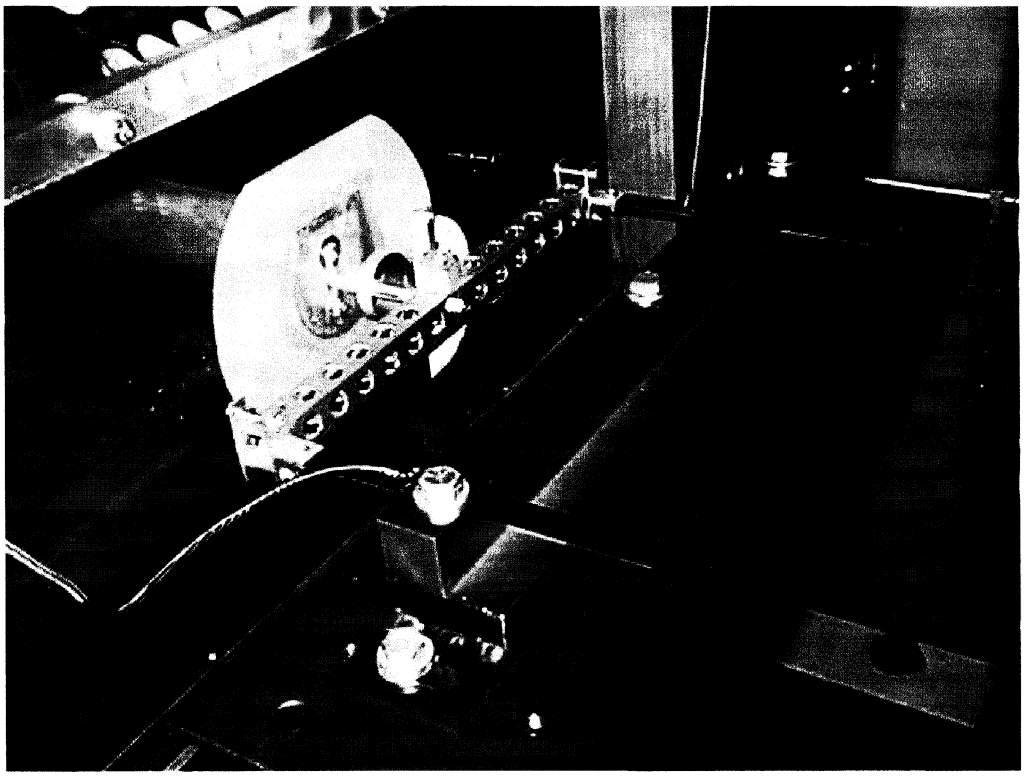

Figure 3.9

Photograph of the model support structure

Maximum displacement of the model was 0.22 *d*. This limitation was set up by distance between connecting rod (***4***) and hole in the test section wall.

3.7 Test set-up

All test model parts were combined in the experimental set-up. A schematic view of the experimental set-up is presented on the ***Figure 3.10***.

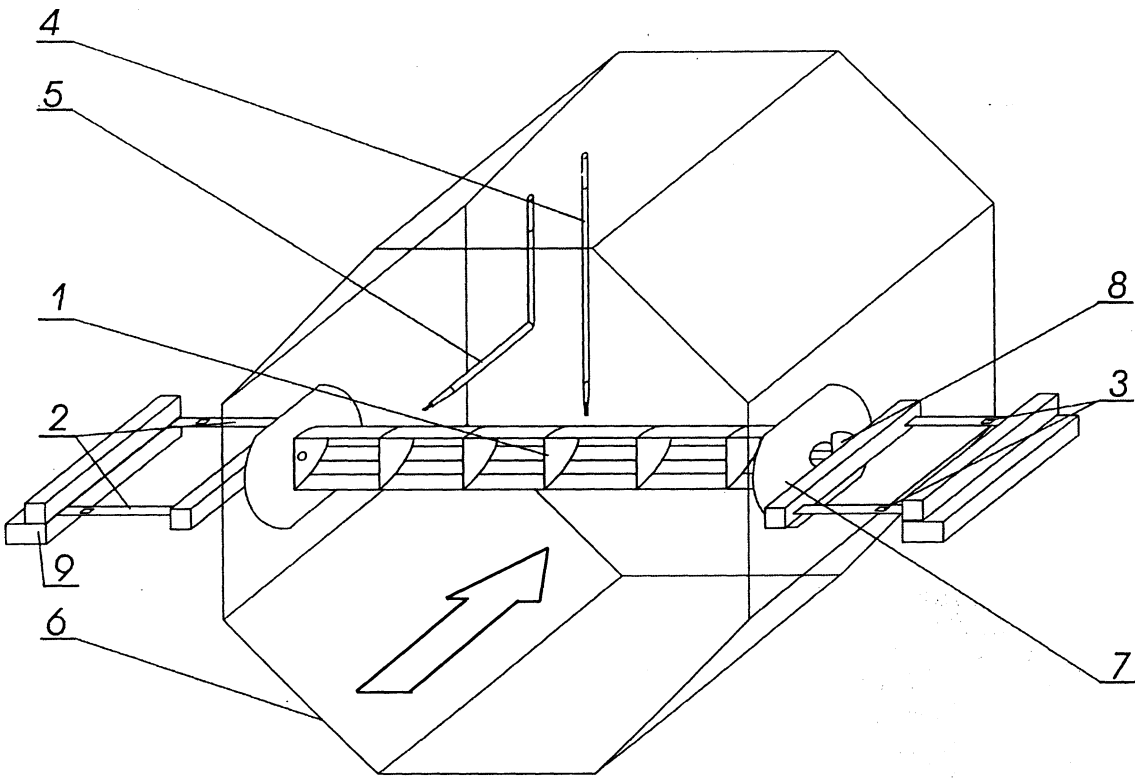

Figure 3.10

Experimental set-up with arrow indicating flow direction

1 – test model, 2 – elastic beams, 3 – strain gauges, 4 –wake response hot wire, 5 – flow velocity hot wire, 6 – wind tunnel test section, 7 – end plate, 8 – protractor, 9 – rigid support

The test model (*1*), centred between the test section parallel sides, was placed up-stream in the test section (*6*), at approximately 1/6 of the test section length from the upstream end. Four strain gauges (*3*), one for each elastic beam (*2*), were used for monitoring the test model response.

Flow velocity was measured by the hot wire (*5*), while the wake response frequency was monitored by the hot wire (*4*). The flow velocity hot wire was 6 d in front of the model leading edge. The vortex shedding hot wire was placed approximately 2 d behind the model leading edge, in order to ensure that it could not be contacted by the model during large amplitude vibrations.

The support set-up enabled clear differentiation between three principal force directions: lift, drag and moment. As a result, the response of the model due to aerodynamic lift and moment could be clearly detected by the strain gauges. Moreover, information retrieved from the strain gauge signals could be used to obtain both the frequency content and amplitude of the oscillations. Translation and rotation could be distinguished by comparing the phase of the each strain gauge signal.

Another advantage of this experimental set-up was that model could be rotated around the centre of gravity, thus establishing any desired initial angle of attack.

A further characteristic of this set-up was that position of the model elastic axis relative to its centre of gravity could be changed, thus introducing a coupled plunge-torsion motion. The model elastic axis position was changed by moving the elastic beams as illustrated in ***Figure 3.11***.

Dynamic experiments were conducted for three different elastic axis positions. In the first set of experiments, elastic axis coincided with the centre of gravity. In the second and third set of the dynamic experiments, model elastic axis was positioned 50 mm and 95 mm, respectively, behind the line coinciding with the model centre of gravity.

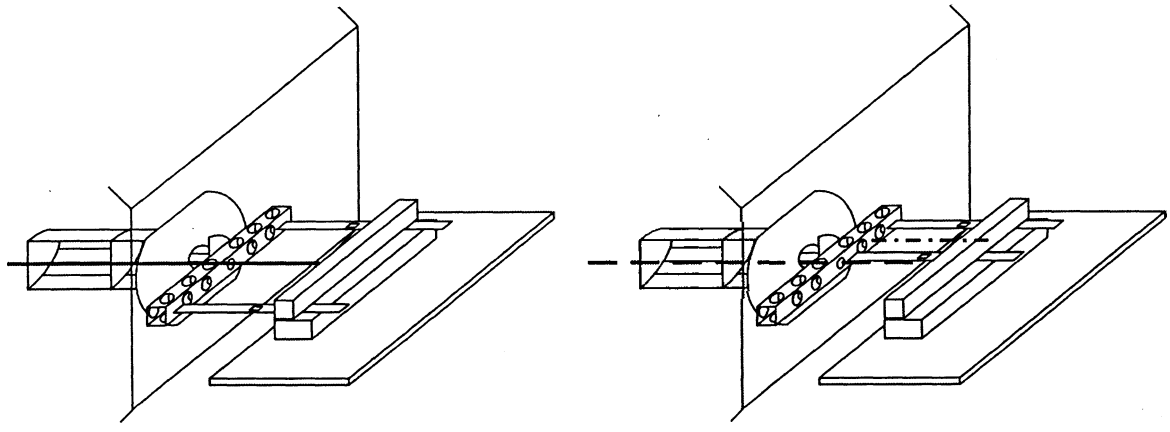

a) *b)*

—— centre of gravity coincides with system elastic axis

— – line passing trough model centre of gravity

–·–· system elastic axis

Figure 3.11

Change of the model elastic axis

a) elastic axis coincides with model centre of gravity

b) elastic axis behind the model centre of gravity

However, in spite of all the effort to reduce mass of the supports, they were heavier than each test model (***Appendix II***). This resulted in the mass being concentrated at the sides of the model, thus introducing an unwanted rocking mode, not present in the prototype mixing blade. To separate the rocking mode frequency from the plunge mode frequency, mass in the form of a lead parallelepiped was added to the model centre of gravity. This resulted in the separation between two frequencies by factor of two.

Chapter 4

Experimental techniques

4.1 Signal detecting

Two different types of signals were detected in this investigation:

- strain gauge signals
- hot wire signals

Strain gauges were used to detect the model response. Four strain gauges were used, each being connected through a Wheatstone bridge to an amplifier. The amplified strain gauge signals were then routed to a dynamic signal analyzer or data acquisition system, depending on the type of the experiment.

To determine the flow behaviour in the experiments, *hot wire probes* were used. Two hot wire probes were placed in the test section, connected to a constant temperature anemometer and then, in case of the flow velocity measurements, to a digital voltmeter. In case of the vortex shedding frequency measurements, the hot wire signals were

directed to the dynamic signal analyzer. A schematic of this instrumentation is shown in *Figure 4.1*.

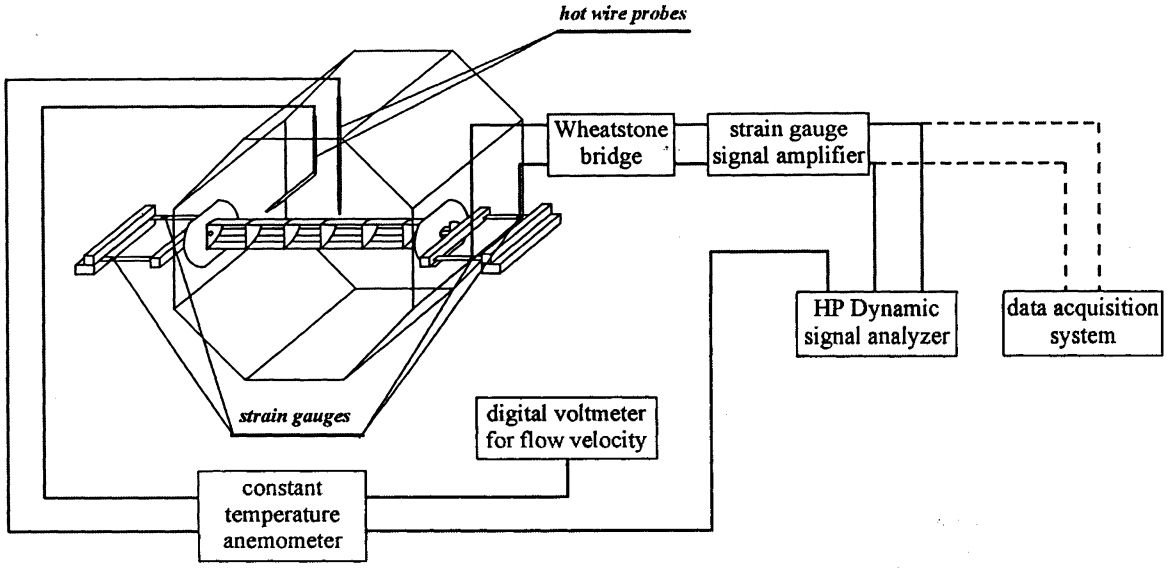

Figure 4.1

Schematic of instrumentation

4.2 Experimental equipment

The following equipment was used in the investigation:

- Strain gauges

  Strain gauges by MICRO-MEASUREMENTS INC., type CEA-06-125UN-350 were used in the experiments. They are open-faced general-purpose gauges, with 3 mm gauge length and 350 Ω resistance.

- Strain gauge signal amplifier

  Signal amplifier by VISHAY INSTRUMENTS, type 2130 Signal Conditioning Amplifier was used in the experiments. The signal conditioner settings were the following:

  - low-pass cut off filter: 100 Hz
  - excitation: 10 V
  - gain: 10000

The strain gauge resistance and Wheatstone bridge excitation level was set according to the recommendation from Window and Holister (1982).

- Hot wire probes

  Tungsten, 5 μm-diameter wires were used. 2 mm-long wires were connected to the constant temperature anemometer by 5 m-long connecting cables. The wire and connecting cable combined resistance was 5 Ω.

- Constant temperature anemometer

  Two-channel amplifier by DISA, type CTA BRIDGE 56C01was used in the experiments.

- Dynamic signal analyzer

  HEWLETT PACKARD type 35670A four-channel dynamic analyzer was used to detect model frequency and amplitude response as well as the vortex shedding frequency in the experiments.

- Flow velocity readout

  HEWLETT PACKARD multimeter type E2373A was used to read hot wire voltage output, calibrated to read flow velocity.

- Data acquisition system

  A PC equipped with data acquisition board was used to detect steady model response in the static experiments.

4.3 Experimental procedure

In the course of this investigation, following variables were monitored:

- flow velocity
- vortex shedding frequency
- model frequency
- model oscillatory amplitude
- model lift and moment

Flow velocity and vortex shedding measurements were taken simultaneously with the dynamic or static model response.

4.3.1 Flow velocity measurements

To determine the flow velocity, the upstream hot wire was used. The correlation between the flow velocity and the voltage output of the constant temperature anemometer was determined by calibrating the hot wire against the Baetz micromanometer. More than 20 points for each calibration curve were taken and used to fit the curve mathematically. The flow velocity in each experiment was then determined from the calibration curve mathematical equation, using the measured hot wire voltage output.

A sample calibration curve is presented in the ***Figure 4. 2.***

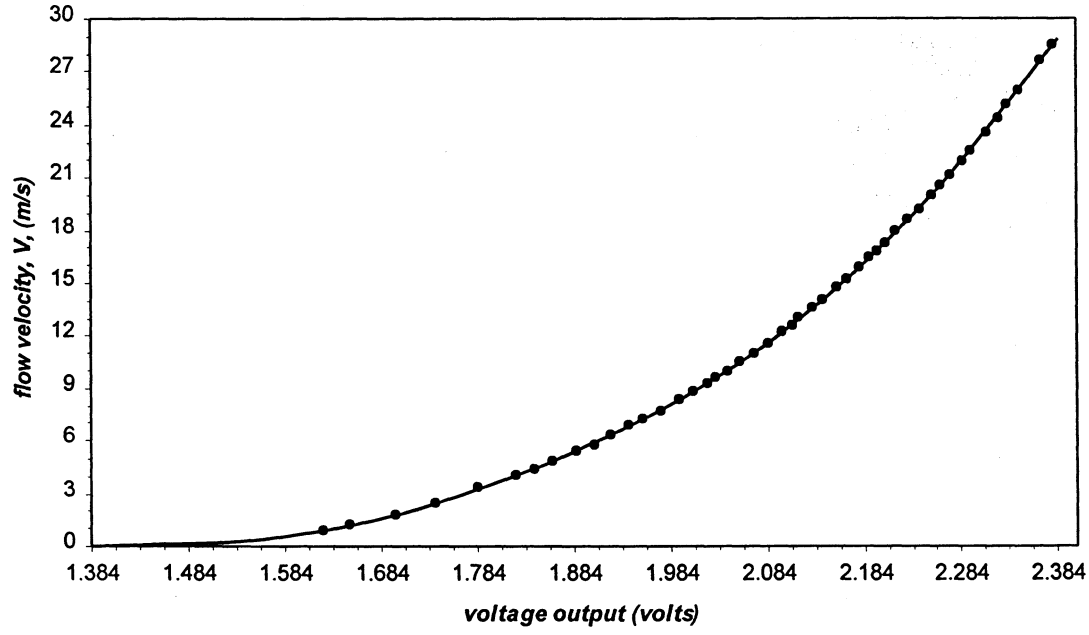

Figure 4.2

Sample hot wire calibration curve

The hot wire calibration curve for the example in ***Figure 4.2*** is given by:

$$Velocity,\ V = 17.902 \cdot (volts)^4 - 114.99 \cdot (volts)^3 + 300.76 \cdot (volts)^2 - 363.65 \cdot (volts) + 166.32$$

During the experimentation, the hot wire characteristics changed slightly resulting in a calibration error. To avoid the error, the hot wire was calibrated after every 15 experiments.

The digital voltmeter used for signal readout had a resolution of 1 millivolt. The estimated error in velocity measurements above 3m/s was about 4%.

4.3.2 Vortex shedding frequency measurements

While monitoring the flow response to the bluff body presence, the measurement of interest was vortex shedding frequency, not the oscillation amplitude. Therefore, no calibration was needed for these measurements.

The signal from the vortex shedding hot wire was analyzed using the HP Dynamic Signal Analyzer using the settings:

- resolution: 0.25 Hz
- average type: RMS
- number of sample averages: 25
- window: Hanning

The vortex shedding frequency was recorded from the HP analyzer at each flow velocity and later entered into a spreadsheet for analysis and plotting. ***Figure 4.3*** presents a typical vortex shedding spectrum from the HP analyzer screen. The vortex shedding response peak frequency was the value of interest. This example diagram presents the frequency spectrum for the semi-elliptic model with 0° angle of attack and a flow velocity of 2.95 m/s. The vortex shedding peak is seen to occur at a frequency of 6.25 Hz.

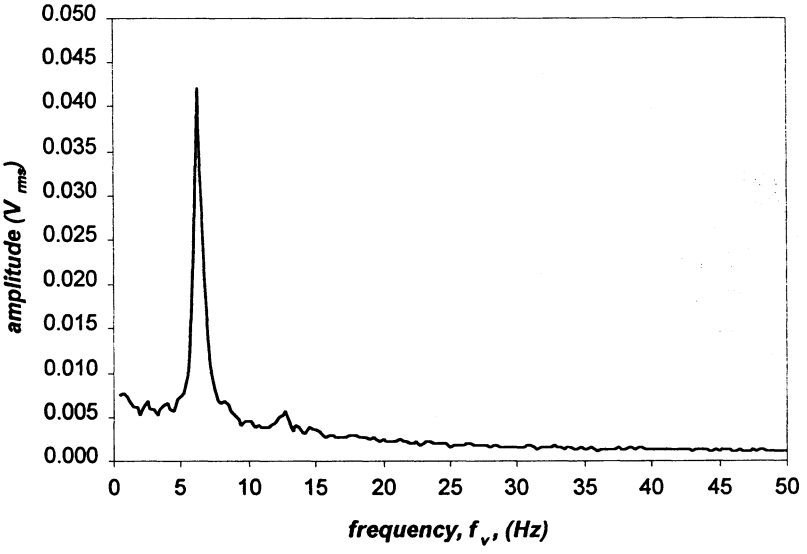

Figure 4.3

Typical frequency spectrum showing vortex shedding peak

4.3.3 Model response

Two different groups of experiments were performed during the course of this investigation. The first group consisted of dynamic experiments where the model

oscillation amplitude and frequency were of primary interest. Thus, the strain gauge signals were dynamically analyzed. The second group of experiments were static experiments, in which the steady lift force and moment for a given flow velocity and angle of attack were of primary interest.

4.3.3.1 Dynamic experiments – procedure and related calibration

With the model in the test section, the mode shapes and associated natural frequencies were detected by perturbing the model in still air. The strain gauge signals were analyzed with the HP analyzer and values for the frequencies were noted. The measured frequency and the known mass of the model were used to calculate the effective stiffness of the system, for use in subsequent calculations.

The flow velocity in the wind tunnel was increased in uneven increments during the course of each experiment. The flow velocity was kept constant during each measurement period. The strain gauge signals were analyzed using the FFT analysis with following parameter settings:

- frequency resolution: 0.25 Hz
- average type: RMS
- number of sample averages: 50
- window: flat top

The 50 sample average was saved on the floppy disk in the binary file. This was repeated for each flow velocity increment during each experiment. The files were

converted to text files using a SDFTOASC program, which was the part of the software package provided with HP Dynamic Signal Analyzer. The amplitude units for the frequency measurements were changed from V_{rms}/Hz to $(V_{rms})^2$/Hz, so that the power spectrum could be used for calculation of the oscillation amplitude. The oscillation amplitude for each flow velocity was calculated by integrating the area of the response power spectrum within the limits of $f_n \pm 1.5$ Hz, where f_n was natural frequency for each mode of interest.

Numerical integration was conducted within the frequency interval, and the amplitude was calculated using the following equation:

$$A = \sum_{1}^{n} \sqrt{S_i \cdot \Delta f_{ni}}$$

where:

A – rms response amplitude

S_i – power spectrum amplitude for frequency resolution increment i

Δf_{ni} – frequency resolution increment

n – number of frequency resolution increments within the integration limits

Examples of the model dynamic response spectra over the range 0 to 50 Hz are presented for a range of flow velocities in ***Figure 4.4***. The semi-circular model was used for this example, with a natural plunge frequency f_n = 13 Hz and natural rocking frequency f_r = 26 Hz. The vortex shedding frequency increased linearly with flow velocity and produced resonance when it coincided with a model natural frequency.

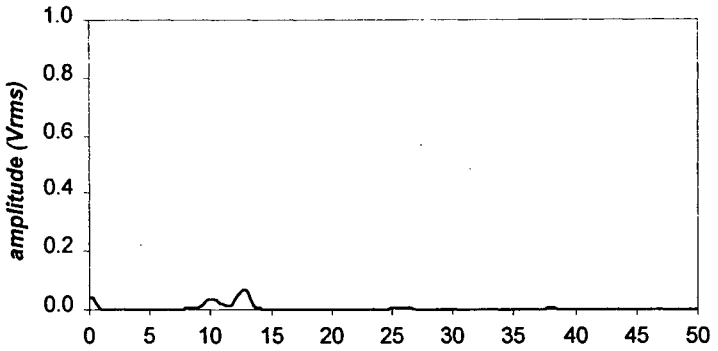

(a) flow velocity 4 m/s, vortex shedding frequency 10 Hz, f_n = 13 Hz, f_r = 26 Hz

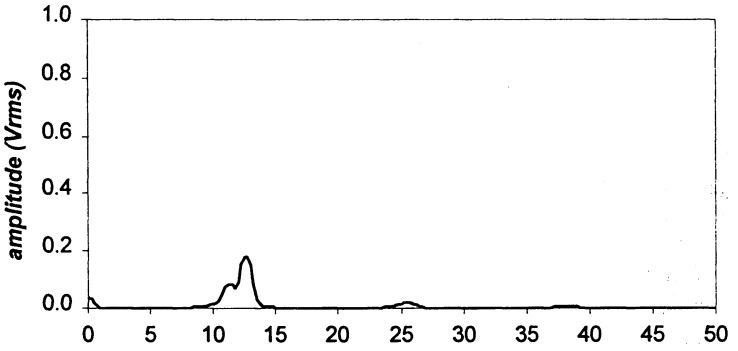

(b) flow velocity 4.5 m/s, vortex shedding frequency 11.25 Hz, f_n = 13 Hz, f_r = 26 Hz

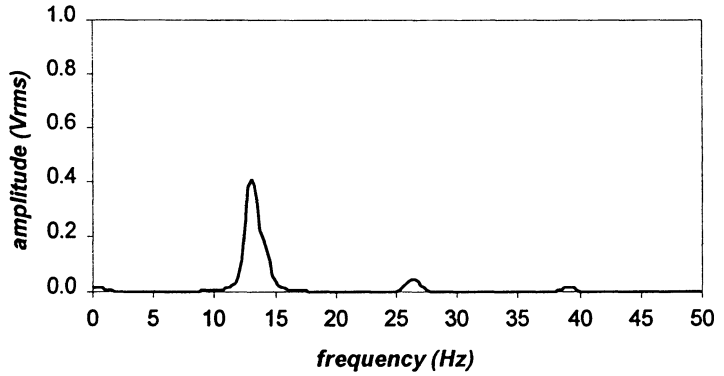

(c) flow velocity 4.75 m/s, vortex shedding frequency 11.75 Hz, f_n = 13 Hz, f_r = 26 Hz

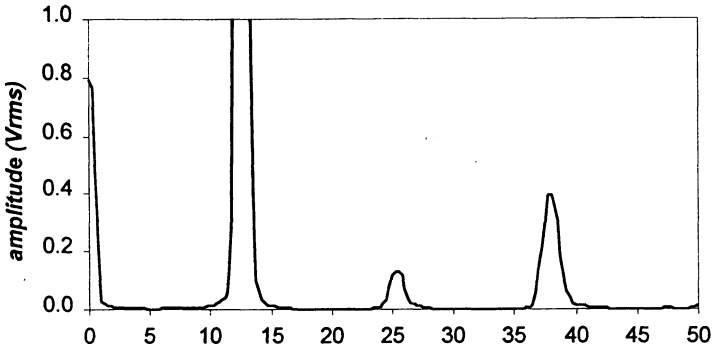

(d) flow velocity 5.3 m/s, vortex shedding frequency 13 Hz, f_n = 13 Hz, f_r = 26 Hz, resonance amplitude 4.23 V_{rms}

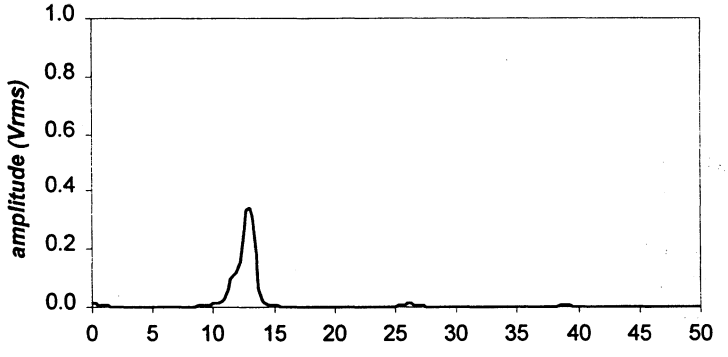

(e) flow velocity 5.75 m/s, vortex shedding frequency 14 Hz, f_n = 13 Hz, f_r = 26 Hz

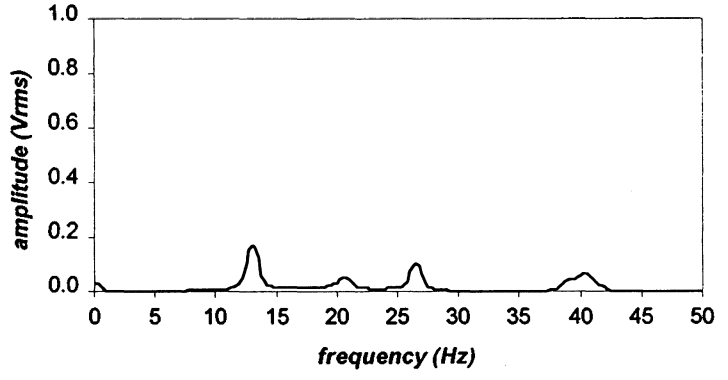

(f) flow velocity 8.6 m/s, vortex shedding frequency 21 Hz, f_n = 13 Hz, f_r = 26 Hz

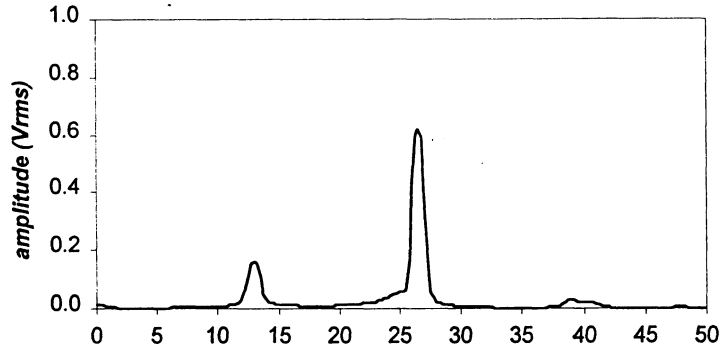

(g) flow velocity 10.75 m/s, vortex shedding frequency 26 Hz, f_n = 13 Hz, f_r = 26 Hz

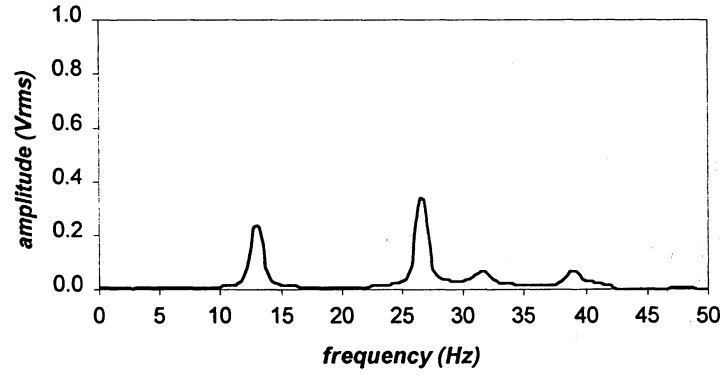

(h) flow velocity 13 m/s, vortex shedding frequency 31.5 Hz, f_n = 13 Hz, f_r = 26 Hz

Figure 4.4

Model rms amplitude response spectrum as a function of flow velocity

There is a noteworthy difference between peak shapes in the vortex shedding frequency and model amplitude response analyses. The difference originates in the FFT window parameter settings. The "Hanning" window was used for the vortex shedding frequency analysis, as it gives more precise determination of the frequency response. This

resulted in sharper peaks, pointing out only one frequency value. In contrast, the "flat top" window was used for the amplitude analysis, since more precise estimation of the amplitude is achieved using this window type (HP 35670A Operator's guide; Dally et al., 1993). With better amplitude estimation, the frequency detection deteriorates, and the resulting peaks were broader. The latter, as well as the small shift in the peak frequency, were the reasons for performing the integration on the broader peaks. The integration was performed for each flow velocity.

In order to convert the oscillation amplitude from V_{rms} to length units, the strain gauges had to be calibrated. Strain gauges may be calibrated against a known force or against a known displacement. Since the stiffness was calculated from the information on the model mass and its natural frequency, the strain gauges were calibrated against a known force. Force was applied in the form of a standardized set of weights hung from the sides of the model. This calibration method is more accurate than calibrating against displacement, since even displacement distribution across the model is much more difficult to achieve. Also, a larger error is introduced with displacement measurement because of the greater uncertainty in measuring displacement than in using a standardized set of weights.

Figure 4.5 depicts the points and directions of the applied forces, represented by arrows.

A pulley system was used to achieve the upward force.

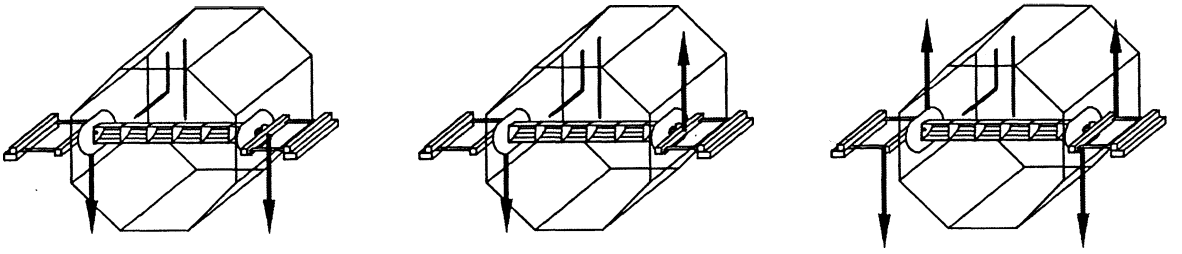

a) *b)* *c)*

Figure 4.5

Locations and directions of applied forces used for strain gauge calibration:

a) plunge mode, b) rocking mode, c) torsion mode

For plunge and rocking mode displacement and lift force calibration, weights were hung from the connecting rod, which coincided with the centre of gravity of the model. To calibrate the moment, weights were hung from the end of the elastic beams. A voltmeter was used to read the strain gauge signals. The calculation curves showed a linear relationship between force and voltage, with deviation from linearity occurring when the deflection exceeded a value of 0.1 *d*.

Calibration equations were obtained from the plotted data. An example of a calibration curve with its mathematical representation is presented in ***Figure 4.6***. This is the calibration of the semi-circular model test set-up in its plunge mode.

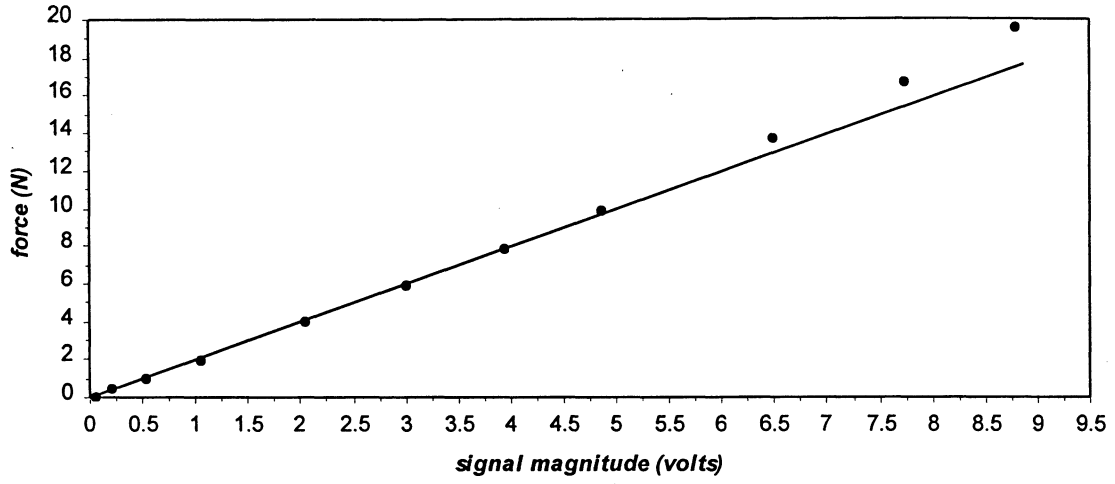

Figure 4.6

Sample calibration curve

Calibration curve for the open semi-circular model

Calibration curve equation y = 1.987 x

Due to the stiffening effect of the elastic beams material, error occurs in the amplitude values above 6 % *d*, which corresponds to the 15 N force for the sample calibration curve presented on the ***Figure 4.6***. Calibration curves are presented in *Appendix III*.

The flow velocity, vortex shedding and response amplitude data were further entered into a MICROSOFT EXCEL worksheet. The response amplitudes obtained by integration were converted into force using the appropriate calibration equation and then divided by stiffness to obtain the rms length units. All data were normalized as follows so that the plotted data were dimensionless:

- vortex shedding frequency f_s was divided by plunge natural frequency f_n.
- flow velocity V was divided by the plunge natural frequency f_n and the characteristic length, d, to produce reduced velocity V_r:

$$V_r = \frac{V}{f_n \cdot d}$$

- amplitude was presented as a percentage of the model characteristic length d.

4.3.3.2 Static experiments – procedure and calibration

Steady lift and moment coefficients with respect to the angle of attack, α, were measured in the second group of experiments. Steady lift forces and moments cause static displacements of the model. To determine the fluid force and moment acting on the body, steady voltage from the two strain gauges located on the same side of the model was monitored. After amplification, the strain gauge signals were directed to the data acquisition board connected to the PC. With flow velocity kept constant, the model response was recorded for 20 seconds and saved on the hard disk. Statistical analysis was performed using Windaq software, and mean values were calculated.

The calibration of the strain gauges was similar to the calibration procedure for dynamic model response (paragraph ***4.3.3.1***). The strain gauge signals were added to obtain the lift force.

The lift coefficient, C_L, was calculated using the equation relating flow velocity V, characteristic dimensions d and L and fluid lift force F_L and fluid density of air:

$$C_L = \frac{2 \cdot F_L}{\rho_{air} \cdot d \cdot L \cdot V^2}$$

where:

C_L – lift coefficient

F_L – lift force

d – model characteristic length

L - model length

V – flow velocity

ρ_{air} – air density

Moment coefficient C_M was calculated using a similar expression:

$$C_M = \frac{2 \cdot M}{\rho_{air} \cdot d^2 \cdot L \cdot V^2}$$

where:

C_M – moment coefficient

M – aerodynamic moment exerted on the body

In contrast to the fluid lift force detection, the strain gauges signals were subtracted for fluid moment detection.

Data were recorded for different numbers of model angles of attack α and were plotted on a diagram.

4.4 Damping measurements

With semi-circular cross-section model in the test section and elastic beam length l_b = 65 mm, damping value was measured. Model was perturbed in the still air, time trace of the amplitude response was captured using data acquisition board. Logarithmic decrement was calculated using the in house software. From the logarithmic decrement, damping value was calculated as an average value from the five measurements.

Model set-up damping was determined to be $\beta = 1\%$.

4.5 Experimental error

An estimation of the experimental error in measured quantities is presented here.

4.5.1 Error in the flow velocity measurement

Flow velocity was measured using constant temperature anemometer. Signal from the hot wire was calibrated against the Baetz micromanometer and, during experiment, it was read on the voltmeter. Error in the flow velocity measurement ξ_{fv} was estimated as:

$$\xi_{fv} = \sqrt{\xi_{cta}^2 + \xi_{cp}^2 + \xi_{cB}^2 + \xi_v^2}$$

where:

ξ_{cta} = 1% – constant temperature anemometer error, according to Dally et al. (1993).

ξ_{cp} = 2% – calibration error coming from the Pitot static pressure probe, according to United Sensor Corporation, Bulletin 1.

ξ_{cB} = 2.36% – calibration error coming from the Baetz micromanometer resolution, calculated for the 6 m/s flow velocity.

ξ_v = 2% – error in the digital voltmeter read out

Estimated error in the flow velocity measurement for the value of 6 m/s is 4%. Due to the non-linear characteristic of the Baetz micromanometer, error in the flow velocity is higher for the flow velocities below the 6 m/s and was estimated to be 15% for the flow velocity of 2 m/s. However, for the same reason, error for the flow velocities above the 6 m/s was estimated to be 2%.

4.5.2 Error in the amplitude measurement

Estimated calibration error in the amplitude measurement was 6%. For the amplitude higher then 6% *d*, error increased because of the stiffening of the elastic beams effect. The errors due to discretization in the HP analyzer and data acquisition systems were neglected as small values comparing to the calibration error value.

4.5.3 Error in the model angle of attack set-up

One of the model set-up characteristics that had significant influence on the dynamic and static response of the model is angle at which model span was facing the flow, called model angle of attack α.

Angle of attack was possible to set-up with the accuracy of $\alpha \pm 2°$.

Chapter 5

Experimental results

The responses of four different test model cross-sections were analyzed in this investigation:

- open semi-circular cross-section model
- closed semi-circular cross-section model
- semi-elliptical cross-section model
- parabolic cross-section model

The detailed cross-section characteristics were presented in ***Chapter 3***.

Three groups of experiments were performed on the test models:

- experiments with the model elastic axis coinciding with the centre of gravity
- experiments with the model elastic axis positioned 50 mm and 95 mm behind the centre of gravity

- experiments with the model elastic axis positioned 95 mm behind the centre of gravity performed on a modified parabolic cross-section model

Initial experiments in the first group were performed on the closed semi-circular cross-section model. Previously published (Novak and Tanaka, 1974) response tests of the closed semi-circular cross-section model to flow excitation were repeated using the current experimental set-up. Also, lift and moment coefficient values for this cross-section were determined and compared against known values (Novak and Tanaka, 1974). Positive comparison against these previously published results verified the current experimental set-up. These initial experiments were followed by similar experiments performed on the other test models.

Results for the open semi-circular cross-section model were compared with the results for the closed semi-circular cross-section model. Through this comparison, the effect of the open semi-circular cross-section modification on the dynamic and static response was observed.

Further investigation included dynamic i.e. amplitude and frequency, and static i.e. lift and moment coefficients, response of the semi-elliptical and parabolic cross-section test models. These experiments were conducted with the model support set-up where the elastic axis coincided with the centre of gravity.

For the second set of experiments, the model support set-up was changed in a way that the elastic axis was, stream-wise, behind the centre of gravity. Two different elastic

axis positions were investigated, 50 mm and 95 mm behind the model centre of gravity. The change of the elastic axis position introduced a combined rotational and plunge motion, modeling the dynamic response of the mixing blade. Only the dynamic response for the combined plunge and rotation amplitude was investigated since the change in the elastic axis position does not influence the static response.

In the third set of experiments, the parabolic cross-section model was modified with fins added to the separation cross-section points in an attempt to change the model dynamic response.

5.1 Semi-circular cross-section model experimental results

5.1.1 Closed semi-circular cross-section model results

The closed semi-circular cross-section model faced the flow at zero angle of attack, α. The flow velocity was increased from zero to 22 m/s, corresponding to a Reynolds number range from 0 to $9 \cdot 10^4$. The experimental set-up characteristics were:

elastic beam length $l_b = 65$ mm

model mass $m_c = 615$ g

plunge frequency $f_n = 13$ Hz

rocking mode frequency $f_r = 26.25$ Hz

plunge mode stiffness $K = 4100$ N\m

The vortex shedding frequency f_v, plunge mode amplitude A, and rocking mode amplitude A_r, were monitored.

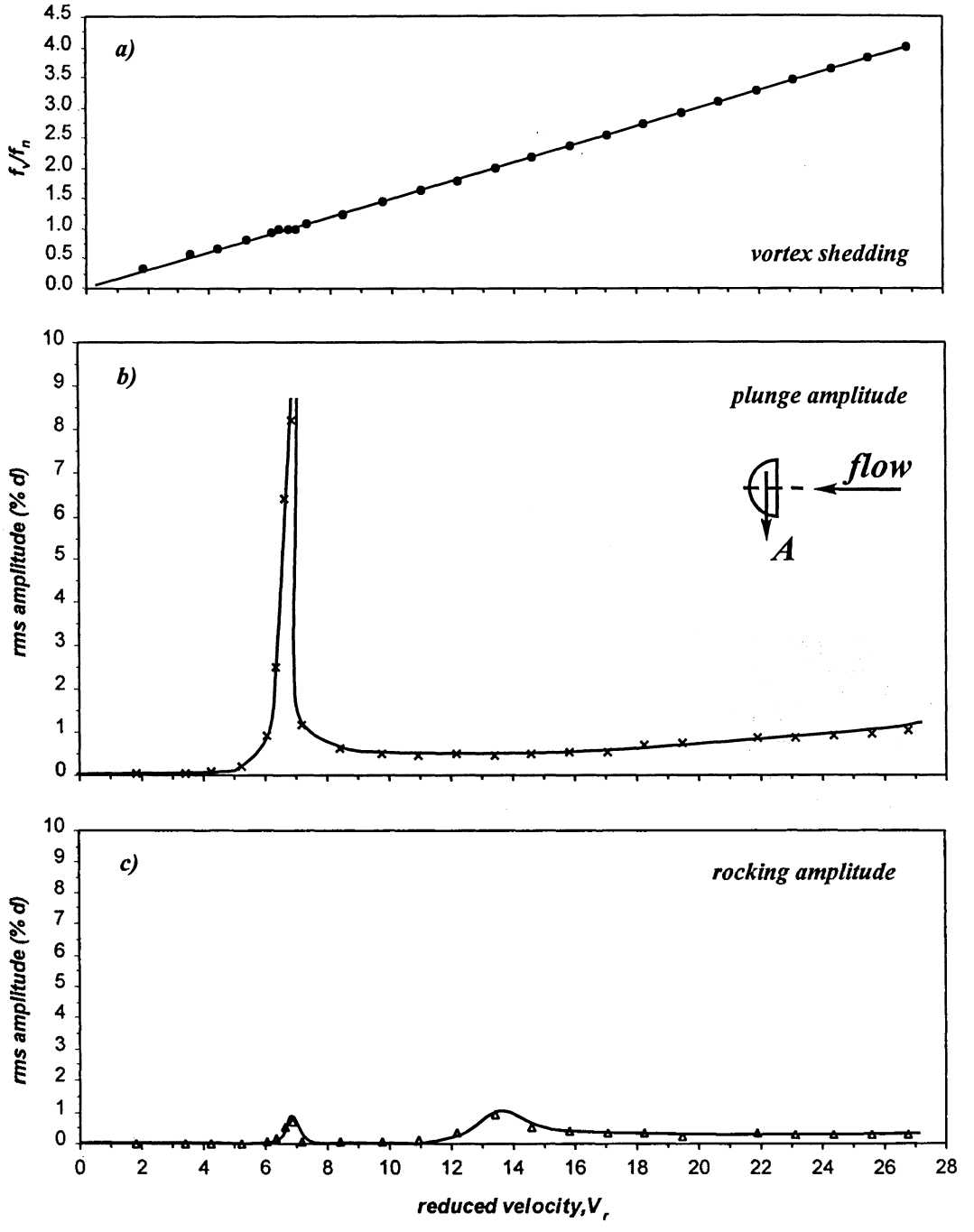

Figure 5.1

Closed semi-circular cross-section model dynamic response

The reduced velocity $V_r = \frac{V}{f_n \cdot d}$ is the horizontal axis in ***Figure 5.1***. In the vortex shedding response diagram, ***5.1(a)***, the vertical axis represents the ratio between vortex shedding frequency f_v and natural plunge mode frequency f_n. In the amplitude diagrams, the vertical axis represents the root-mean-square (rms) oscillating amplitude value as a percentage of the model characteristic width, d.

The vortex shedding frequency increased linearly with flow velocity, as seen in ***Figure 5.1(a)***. When the vortex shedding frequency was close to, or the same as, the natural frequency of any mode, resonance occurred. In the case of the plunge mode, at a reduced velocity $V_r = 6.5$, 10% d amplitude was observed, together with a short range of vortex shedding lock-in. A similar response was observed when the vortex shedding frequency coincided with the rocking mode natural frequency, although no vortex shedding lock-in was observed. At higher flow velocities, the amplitude response was the result of the turbulence present in the flow. Plunge and rocking mode frequency values were separated by factor of two. However, some small coupling of the plunge and rocking modes was observed. No galloping was observed, which is in compliance with results from the literature (Novak and Tanaka, 1974; Parkinson and Brooks, 1961).

An average Strouhal number was calculated from the vortex shedding frequency data. The Strouhal number remained essentially constant within the observed flow velocity range at $S_t = 0.15 \pm 0.003$, as presented in ***Figure 5.2***.

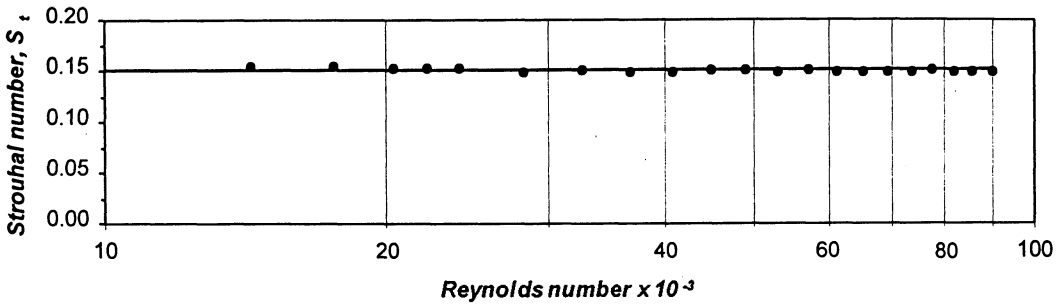

Figure 5.2
Closed semi-circular cross-section model
Strouhal number values for the observed Reynolds number range

The closed semi-circular cross-section model lift and moment coefficients were investigated in static experiments. The lift coefficient, C_L, represents the force perpendicular to the flow direction. The moment coefficient, C_M, was calculated from the fluid moment at the model centre of gravity. The observed values for the lift and moment coefficients, ***Figure 5.3***, agreed reasonably well with the previously published results (Novak and Tanaka, 1974), ***Figure 2.6*** and ***Figure 2.8***. The difference between the results was approximately 10 % at peak values.

The lift and moment coefficient dependence on the flow velocity V and, consequently, the Reynolds number R_e, was noted. Experiments were repeated for several Reynolds numbers over the range $1.85 \cdot 10^4$ to 10^5.

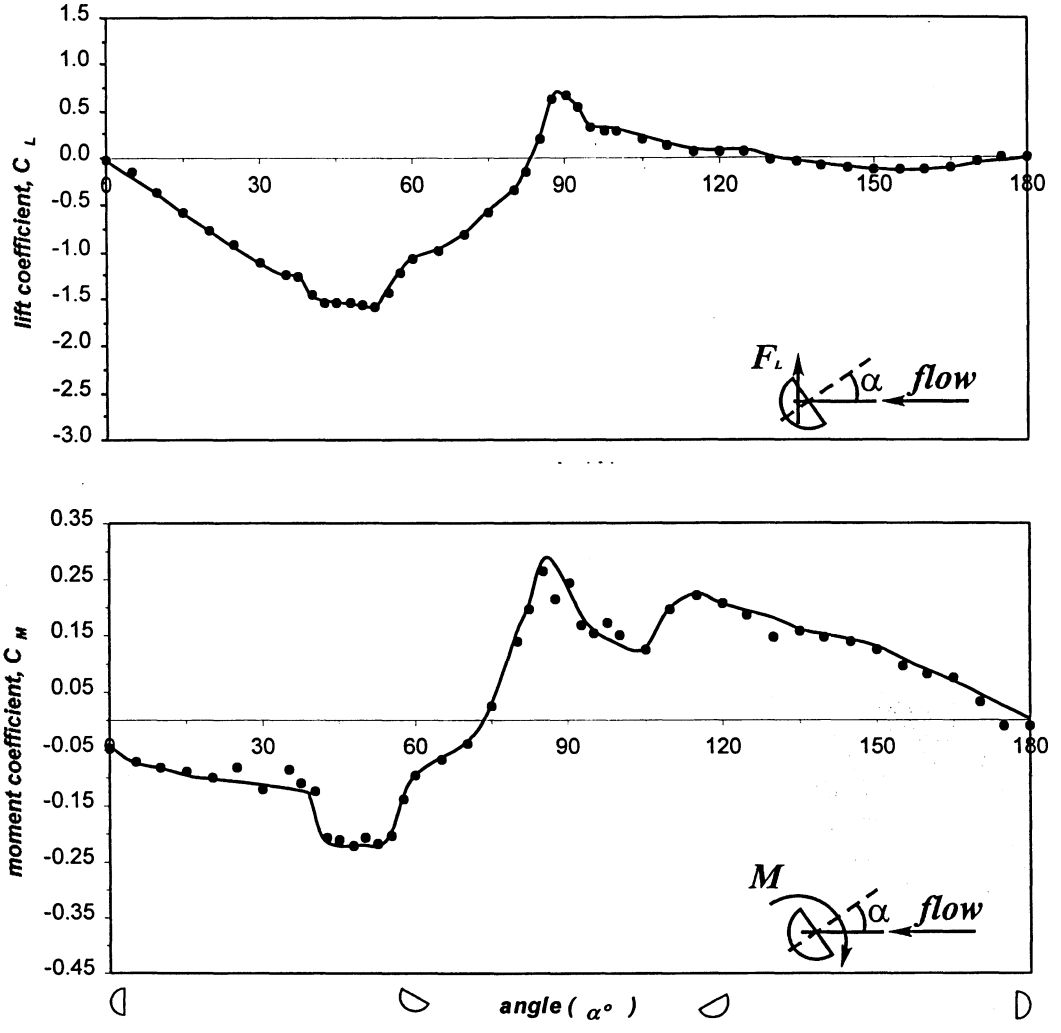

Figure 5.3

Closed semi-circular cross-section lift and moment coefficients

Reynolds number $R_e = 10^5$

The lift coefficient value decreased with increasing Reynolds number, ***Figure 5.4***. The largest difference for the lift coefficient occurred at an angle of attack $\alpha = 45°$ where the difference was 60%.

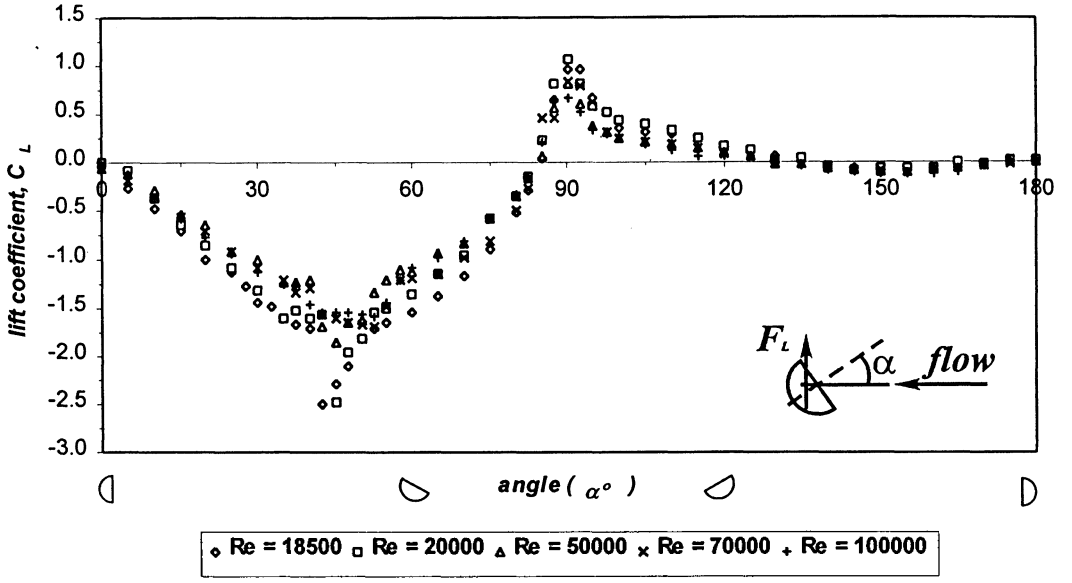

Figure 5.4

Lift coefficient for closed semi-circular cross-section at different Reynolds numbers

In order to compare results from this investigation with those previously published, Strouhal number, lift and moment coefficients were calculated using a constant value of the characteristic width *d*, i.e. 62 mm. When the model was rotated, characteristic width changed with change in the model angle of attack. The Strouhal number, lift and moment coefficients were calculated more accurately when a corrected characteristic width *d'* was used instead of the constant characteristic width, *d*. *d'* represents the model width at the corresponding angle of attack projected on the plane perpendicular to the flow direction. Strouhal numbers corresponding to *d* and *d'*, together with lift and moment coefficients, as functions of the model angle of attack are presented in ***Appendix IV***.

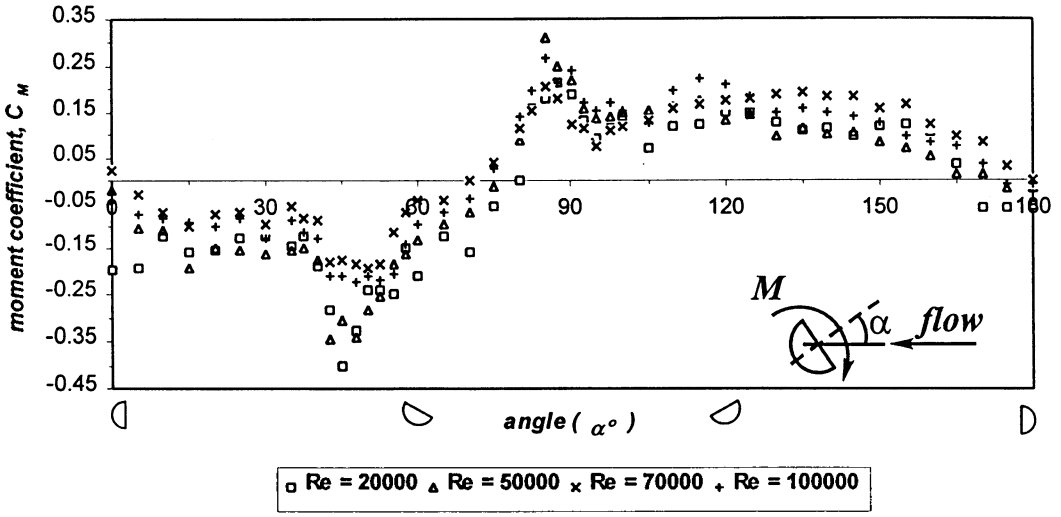

Figure 5.5

Moment coefficient for closed semi-circular cross-section at different Reynolds numbers

Figure 5.6 presents the results obtained for the Strouhal number, S_t, with respect to angle of attack, α, for several Reynolds number, R_e, values. The corrected characteristic width, d', was used in the S_t calculation. Strouhal number was independent of the angle of attack up to $\alpha = 30°$. A strong relationship between the model angle of attack and the Strouhal number existed for angle values greater than 30°. Interestingly, the angle where the abrupt changes in the Strouhal number occurred, coincided with the angle of attack having the peak lift and moment coefficients.

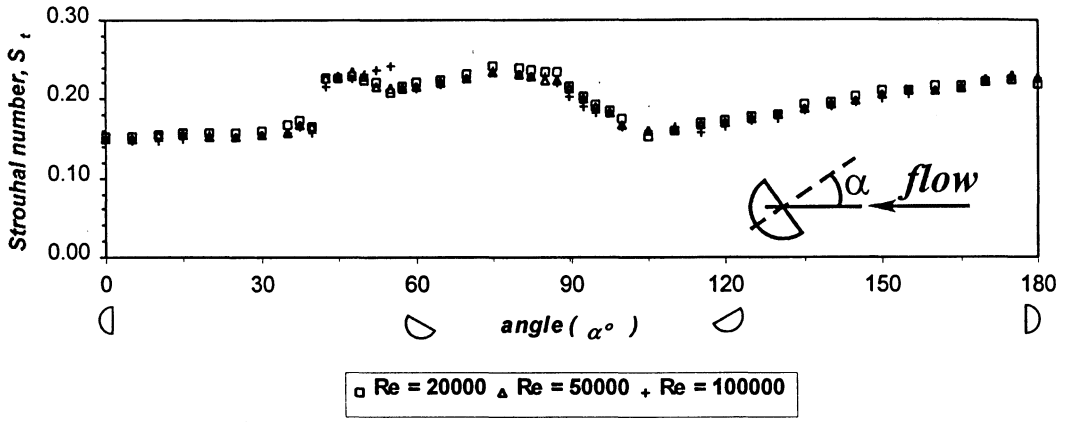

Figure 5.6

Strouhal number as a function of closed semi-circular cross-section model angle of attack for different Reynolds numbers

Diagrams with uncorrected Strouhal numbers are presented in the ***Appendix IV***.

The vortex shedding frequency varied linearly with flow velocity for each angle of attack tested. ***Figure 5.7*** illustrates this linear relationship and the corresponding Strouhal numbers can be read from ***Figure 5.6***.

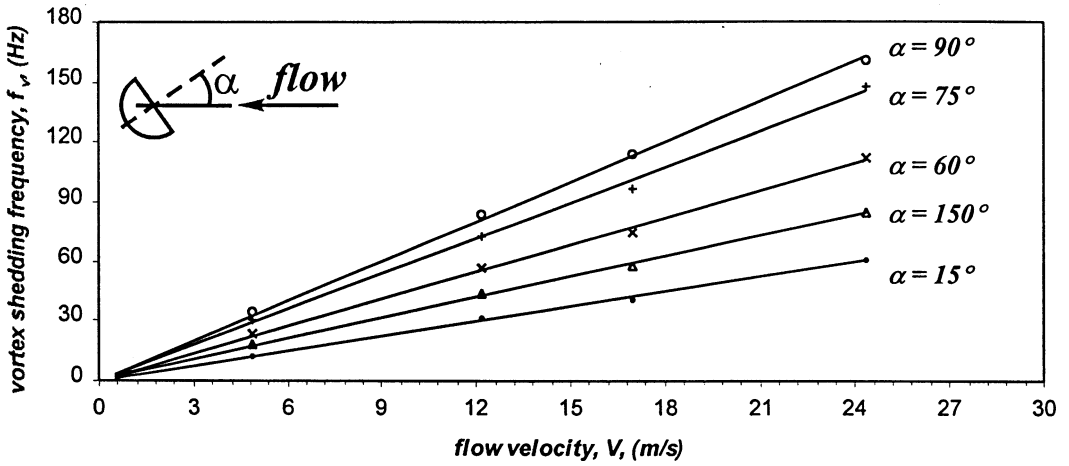

Figure 5.7

Vortex shedding frequency values for several different angles of attack

5.1.2 Open semi-circular cross-section model results

The test set-up characteristics used for the open semi-circular cross-section model experiments were the same as for the closed semi-circular cross-section. Experiments previously performed on the closed semi-circular cross-section were repeated on the open semi-circular cross-section to compare the results between the two.

The open semi-circular cross-section model dynamic response is presented in ***Figure 5.8***. The vortex shedding frequency, f_v, plunge amplitude, A, and rocking amplitude, A_r, were monitored. In the vortex shedding diagram, the vertical axis represents the ratio between vortex shedding f_v and plunge mode f_n natural frequency. The flow velocity is presented as reduced velocity, V_r, in all three diagrams. The amplitude values are expressed as a percentage of the model characteristic width, d.

A similar response to the closed semi-circular cross-section was observed with the open semi-circular cross-section model. The vortex shedding frequency increased linearly with the flow velocity (***Figure 5.8a***). When the vortex shedding frequency value was close to, or the same as, any natural frequency, resonance occurred. For the plunge mode, the amplitude reached 10% of the characteristic width d. The peak was sharp and narrow.

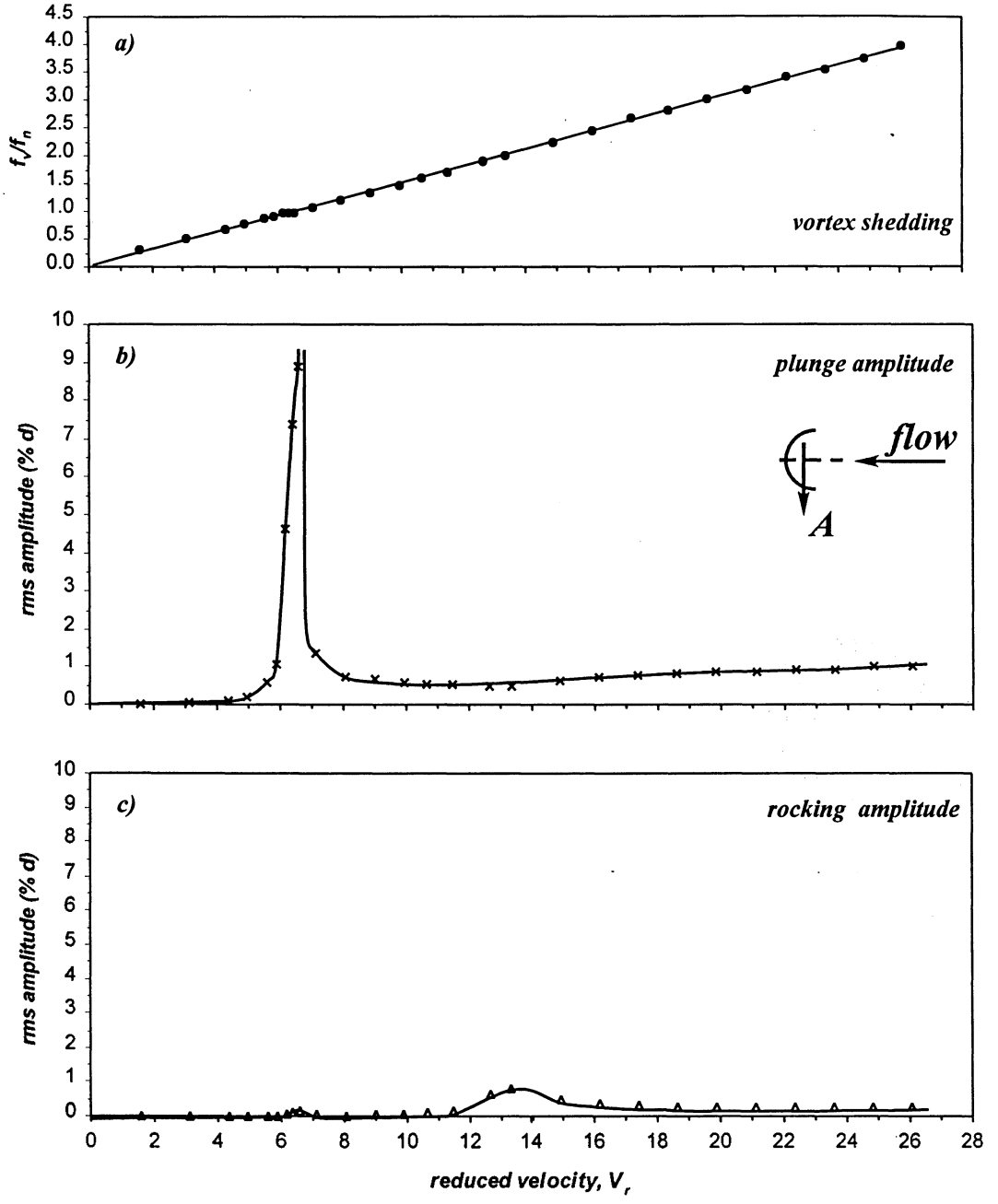

Figure 5.8

Open semi-circular cross-section model dynamic response

The model response was highly flow velocity dependent when the vortex shedding frequency was close to the plunge mode natural frequency. The smallest flow velocity change resulted in a large amplitude change. For this reason the largest amplitude value for the plunge mode could not be determined precisely. As seen for the closed section, a small amount of mode coupling was observed (***Figure 5.8b*** and ***Figure 5.8c***).

An average Strouhal number was calculated from the vortex shedding frequency data. The Strouhal number remained constant within the observed flow velocity range at $S_t = 0.15 \pm 0.002$, as presented in ***Figure 5.9***.

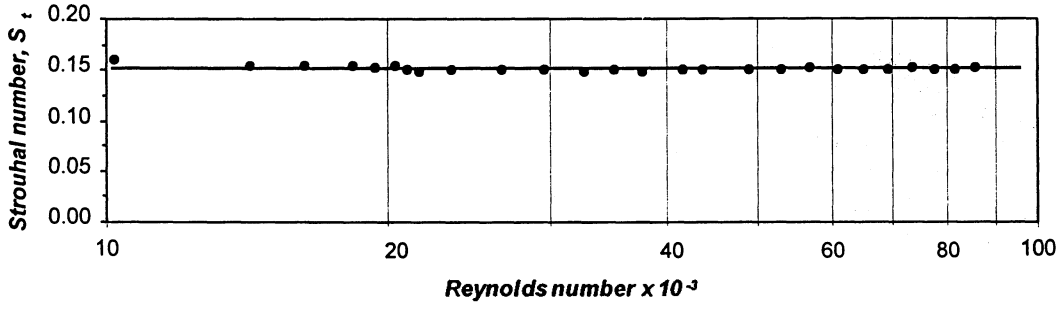

Figure 5.9

Open semi-circular cross-section model

Strouhal number values for the observed Reynolds number range

Figure 5.10 presents the open semi-circular cross-section lift and moment coefficients. For Reynolds numbers close to 10^5, the open semi-circular cross-section lift coefficient follows the same trend as the closed semi-circular cross-section lift

coefficient, with the negative peak value at an angle $\alpha = 45°$ and positive peak value at $\alpha = 90°$.

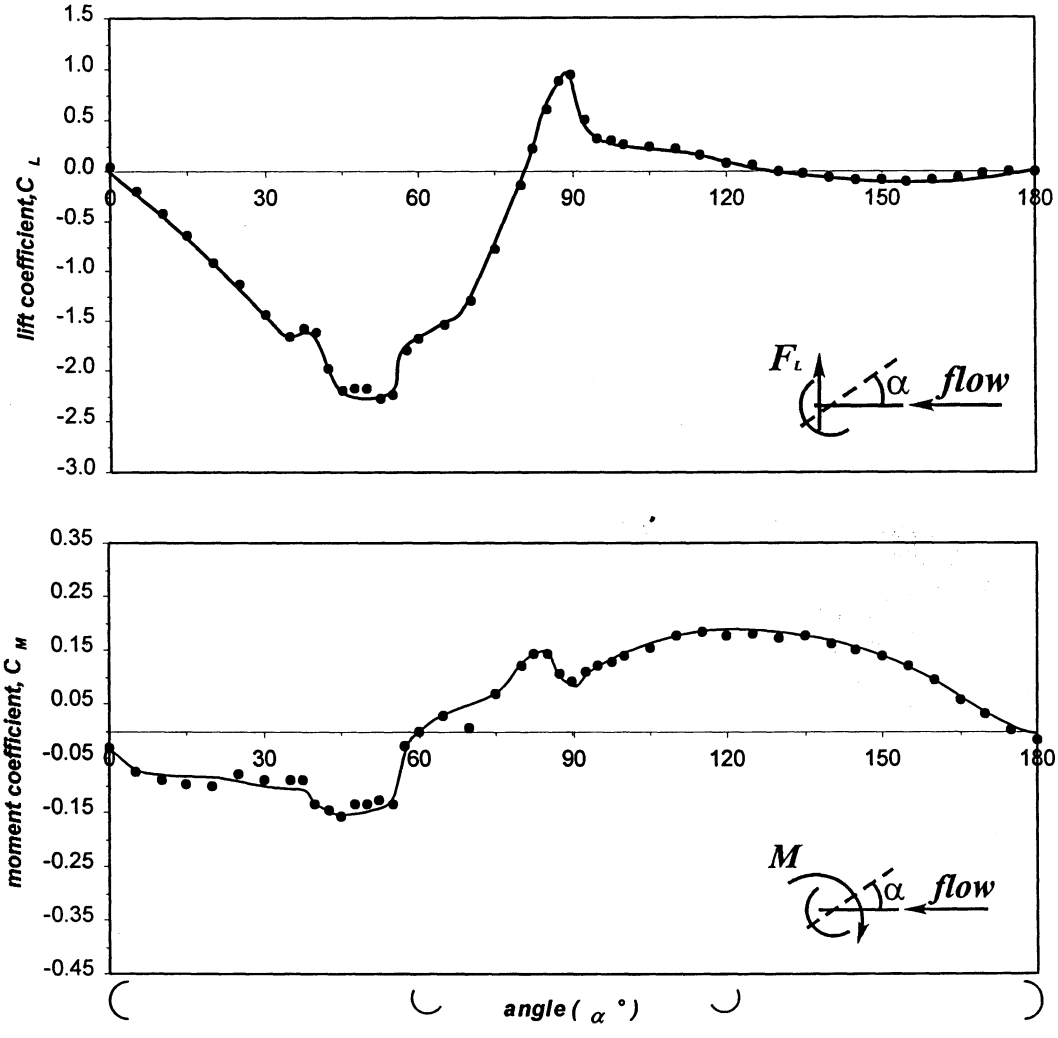

Figure 5.10

Open semi-circular cross-section model lift and moment coefficients

Reynolds number $R_e = 82000$

Opening the semi-circular cross-section significantly increased the lift and moment coefficient peak values. The differences between the open and closed semi-circular cross-section lift and moment coefficients were 30 % and 25%, respectively.

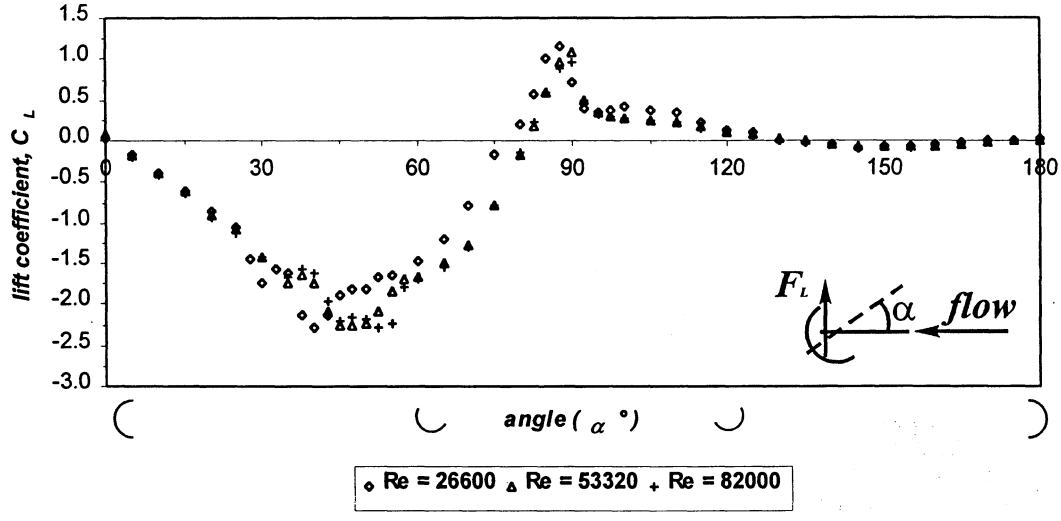

Figure 5.11

Lift coefficient for open semi-circular cross-section at different Reynolds numbers

The lift and moment coefficients for the open semi-circular cross-section were not very dependent on the Reynolds number, within the Reynolds number range as shown in ***Figures 5.11*** and ***5.12***. Similar behaviour was observed by Modi and Slater (1983), (1994), although, open structural angle cross-section model was studied in their experiments.

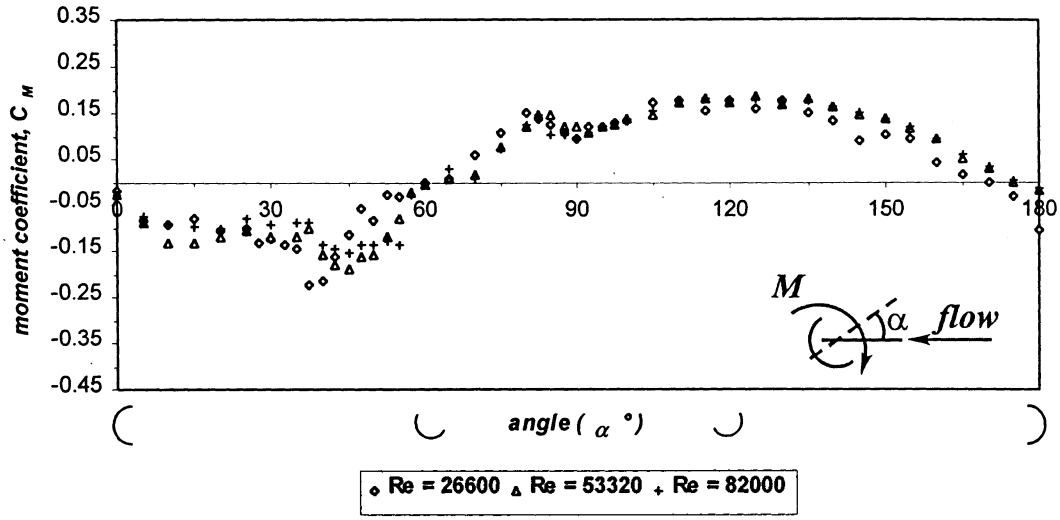

Figure 5.12

Moment coefficient for open semi-circular cross-section at different Reynolds numbers

The open semi-circular cross-section Strouhal number dependence on angle of attack resembles that of the closed semi-circular cross-section, confirming that the change made to the model cross-section did not influence the Strouhal number.

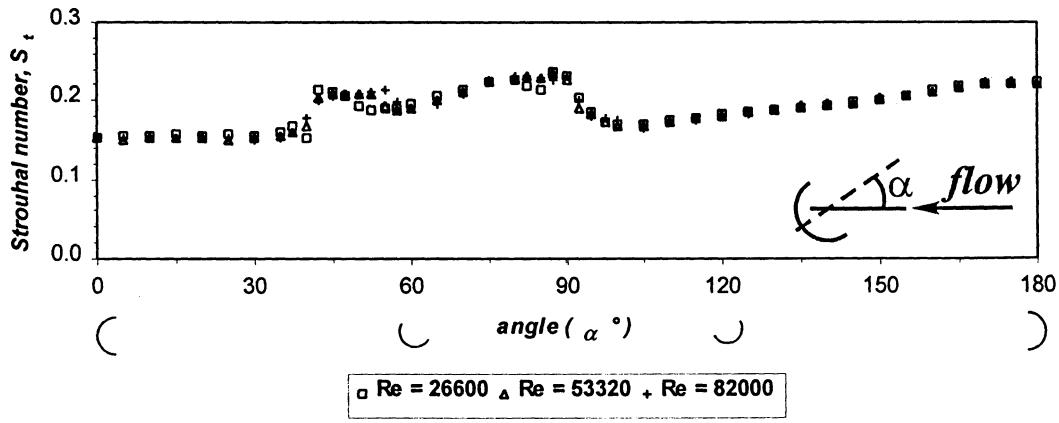

Figure 5.13

Strouhal number as a function of open semi-circular cross-section model angle of attack for different Reynolds numbers

Strouhal number linear dependence on the flow velocity, for the open semi-circular cross-section, was obtained for different angles of attack, as shown in ***Figure 5.14***.

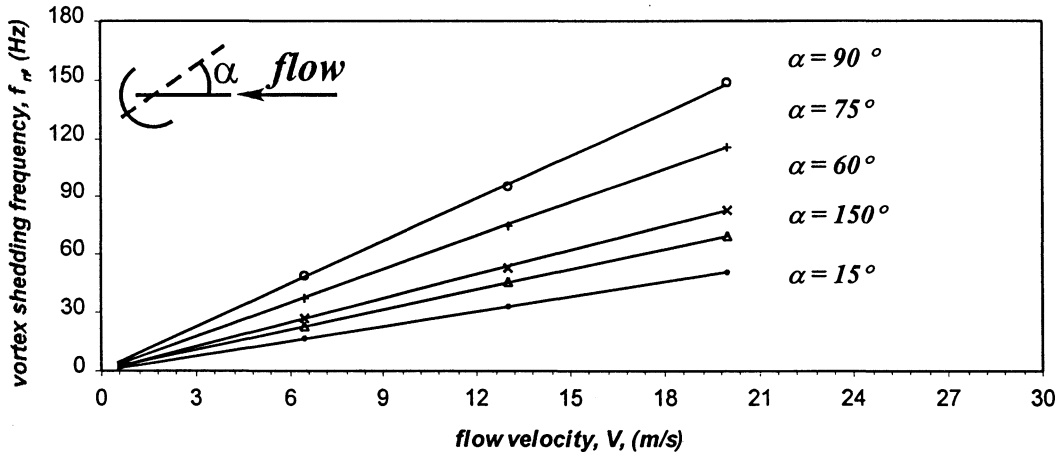

Figure 5.14

Vortex shedding frequency values for several different angles of attack

5.2 Semi-elliptical cross-section model experimental results

The semi-elliptical cross-section model was investigated under the same flow conditions as the semi-circular cross-section model. The semi-elliptical test model had higher mass m_e due to the different shape. Also, because of the different model depth, b, it was possible to use a larger added mass m_{a2}. The mass values for the test set-up components are given in ***Appendix II***.

The test set-up characteristics for the semi-elliptical model were:

elastic beam length $l_b = 63$ mm

model mass $m_e = 665$ g

plunge frequency $f_n = 14$ Hz

rocking mode frequency $f_r = 31.5$ Hz

plunge mode stiffness $K = 5146$ N\m

The same set of variables as for the semi-circular cross-section models were monitored for the semi-elliptic model in the dynamic test experiments. The test results are shown in ***Figure 5.15***. Due to the smaller Strouhal number, the vortex shedding frequency coincides with the plunge mode frequency at a reduced velocity, $V_r = 9$. The resonance peak is wider, but the peak value is lower than the semi-circular model peak values. Although the plunge and rocking modes were separated by more than a factor of (2.25), some rocking mode influence on the plunge mode was present.

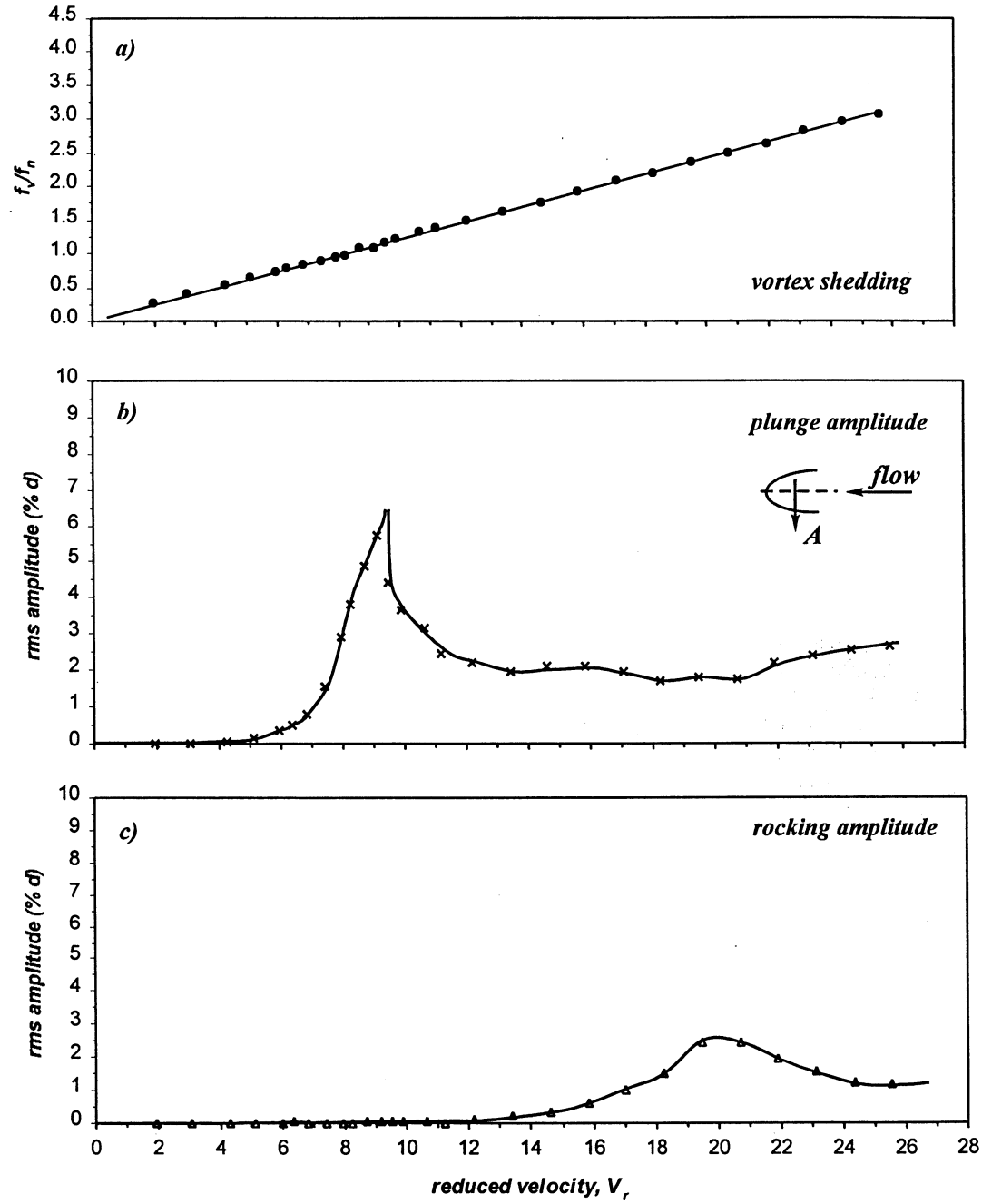

Figure 5.15

Semi-elliptical cross-section model dynamic response

In contrast to the semi-circular models, the amplitude never dropped to insignificant levels (less than 1% *d*) for flow velocities higher than those causing resonance. This difference in post resonance amplitudes is attributed to turbulence excitation on the larger after-body.

At resonance, the observed response had a steady oscillation behaviour. For flow velocities higher than those causing resonance, the response was marked with sudden bursts in amplitude. No galloping was observed for the plunge mode during the dynamic experiments.

As expected, the Strouhal number for the semi-elliptical cross-section model proved to be constant, independent of the flow velocity over the Reynolds number range 10^4-10^5, as shown in ***Figure 5.16.*** The calculated value for the Strouhal number was S_t = 0.12 ± 0.003.

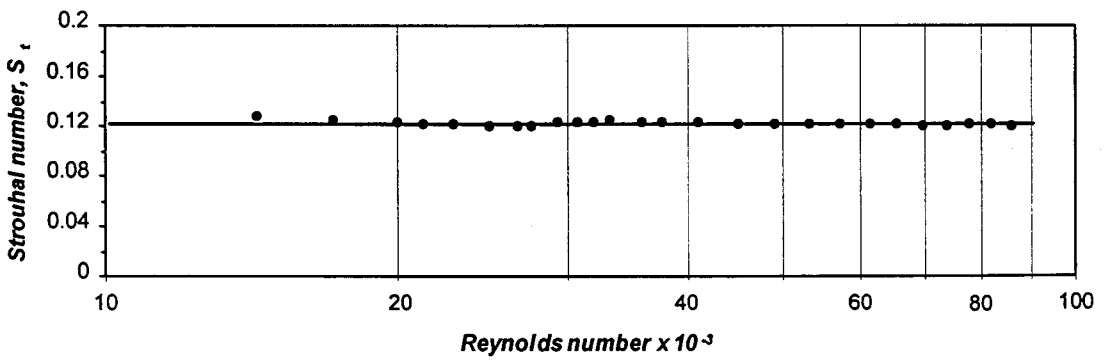

Figure 5.16

Semi-elliptical cross-section model

Strouhal number for the observed Reynolds number range

The lift and moment coefficients for a Reynolds number R_e = 26600 are presented in ***Figure 5.17.***

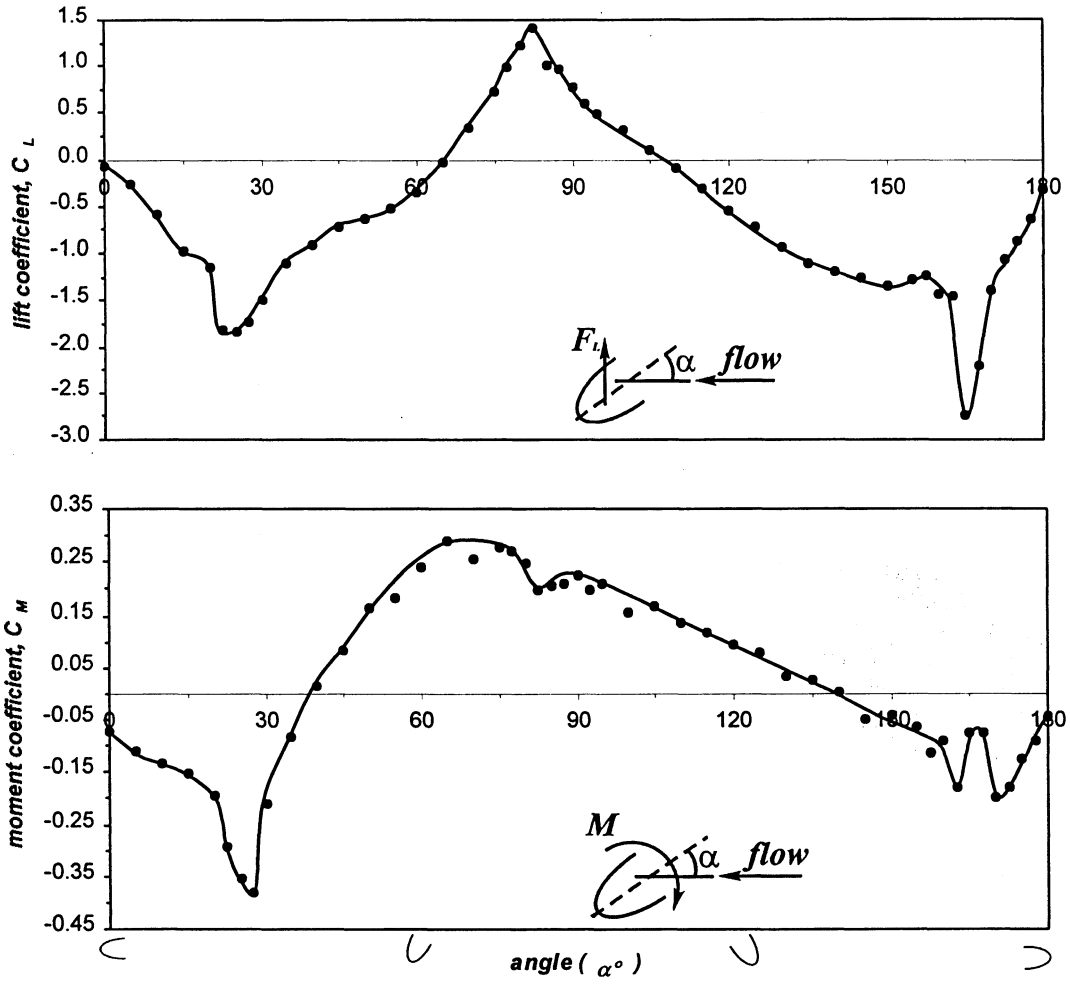

Figure 5.17

Semi-elliptical cross-section model lift and moment coefficients

Reynolds number R_e = 26600

In contrast to the semi-circular cross-section models, the semi-elliptical cross-section model lift and moment coefficients had significantly different trends due to the

large difference in the after-body shape and size. Positive and negative peak values corresponded to the smaller angles of attack, $\alpha = 82.5°$ and $\alpha = 25°$, respectively. Also, there was another negative peak at an angle of attack $\alpha = 165°$. The sudden changes in the lift and moment coefficients at angles of attack $\alpha = 25°$ and $\alpha = 165°$ are attributed to the flow reattachment to the model after-body. The abrupt changes in the Strouhal number occurred at the same angles of attack, as shown in ***Figure 5.18***.

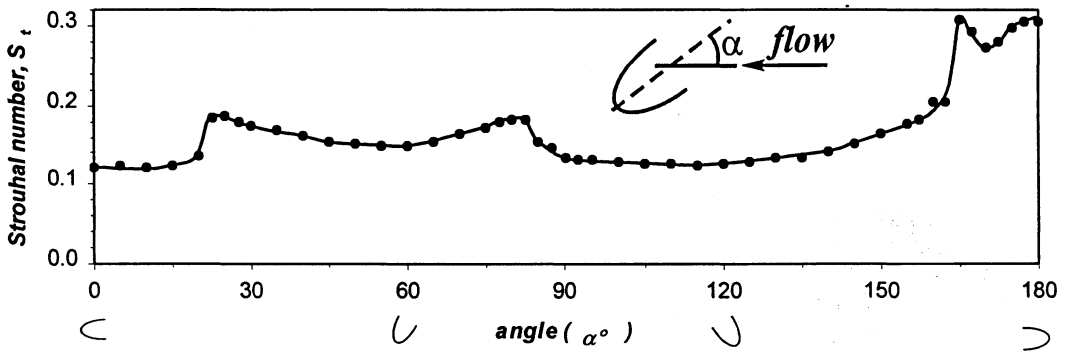

Figure 5.18

Strouhal number as a function of semi-elliptical cross-section model angle of attack for Reynolds number $R_e = 26600$

For the lift coefficient, moment coefficient and Strouhal number calculations, a corrected model characteristic width, *d'*, was used instead of the constant value for the characteristic width, *d*. Strouhal numbers corresponding to *d* and *d'*, together with lift and moment coefficients, as functions of the model angle of attack are presented in ***Appendix IV***.

5.3 Parabolic cross-section model experimental results

The parabolic cross-section model was the scaled version of the mixing blade cross-section. The set-up conditions for the dynamic experiments were the same as for the previously investigated models. With initial model angle of attack α set to 0°, the flow velocity was incrementally increased from 0 m/s to 22 m/s. Plunge and rocking mode amplitudes were monitored together with the wake response.

The test set-up characteristics for the parabolic model were:

elastic beam length	$l_b = 65$ mm
model mass	$m_e = 650$ g
plunge frequency	$f_n = 13.5$ Hz
rocking mode frequency	$f_r = 30.25$ Hz
plunge mode stiffness	$K = 4677$ N\m

The dynamic experiment results for the parabolic cross-section model are presented in ***Figure 5.19***. The horizontal axis represents the dimensionless flow velocity. For the wake response, the vertical axis represents the ratio of the vortex shedding frequency, f_v, to the natural plunge frequency, f_n. In the dynamic response graphs, the vertical axis represents the amplitude expressed as a percentage of the characteristic width d.

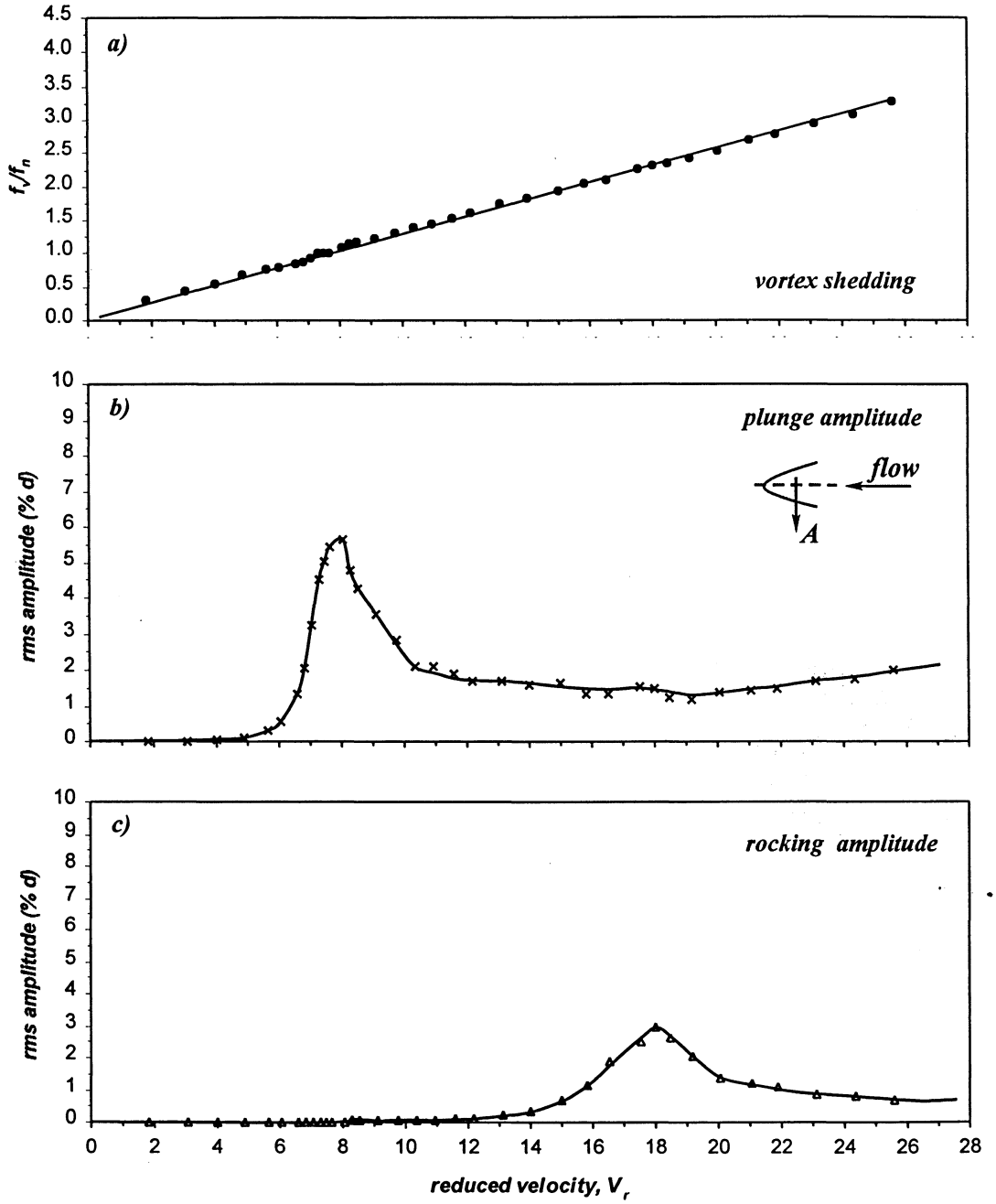

Figure 5.19

Parabolic cross-section model dynamic response

The parabolic cross-section model behaved similarly to the semi-elliptical model. However, in contrast to the latter, the vortex shedding excitation coincided with the natural plunge frequency at a reduced velocity V_r = 8, due to the larger Strouhal number (***Figure 5.19b***). The differences in the plunge amplitude curve between the semi-circular and the parabolic cross-sections were detected. The resonance peak in the parabolic cross-section response was broader, but the maximum resonance amplitude was lower than for the semi-circular cross-section model. Although the plunge and rocking modes were separated by more than a factor of two (2.25), the rocking mode influence on the plunge amplitude was detected over the reduced velocity range from V_r =16 to V_r =21 (***Figure 5.19c***).

Turbulence excitation in the amplitude response was observed for flow velocities above resonance. No galloping of the parabolic cross-section model was observed in the tested flow velocity range.

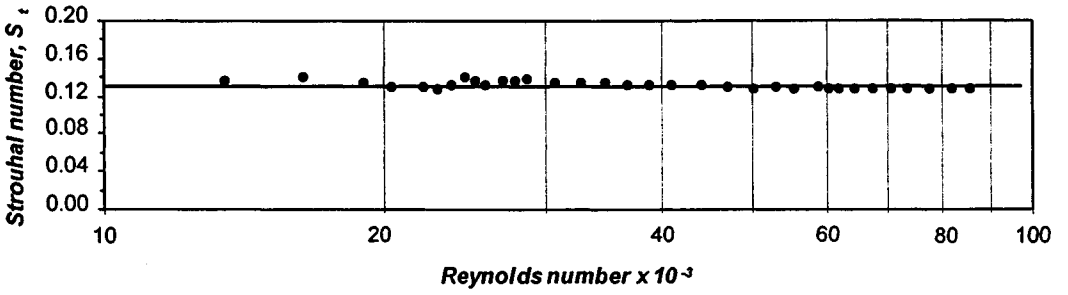

Figure 5.20

Parabolic cross-section model

Strouhal numbers for the observed Reynolds number range

Figure 5.20 presents the calculated Strouhal numbers over the tested flow range for 0° angle of attack. The Strouhal number value was S_t = 0.13 ± 0.004, calculated as an average from the wake response frequency measurements. As expected, the Strouhal number for the parabolic cross-section model was constant over the flow velocity range of the experiments.

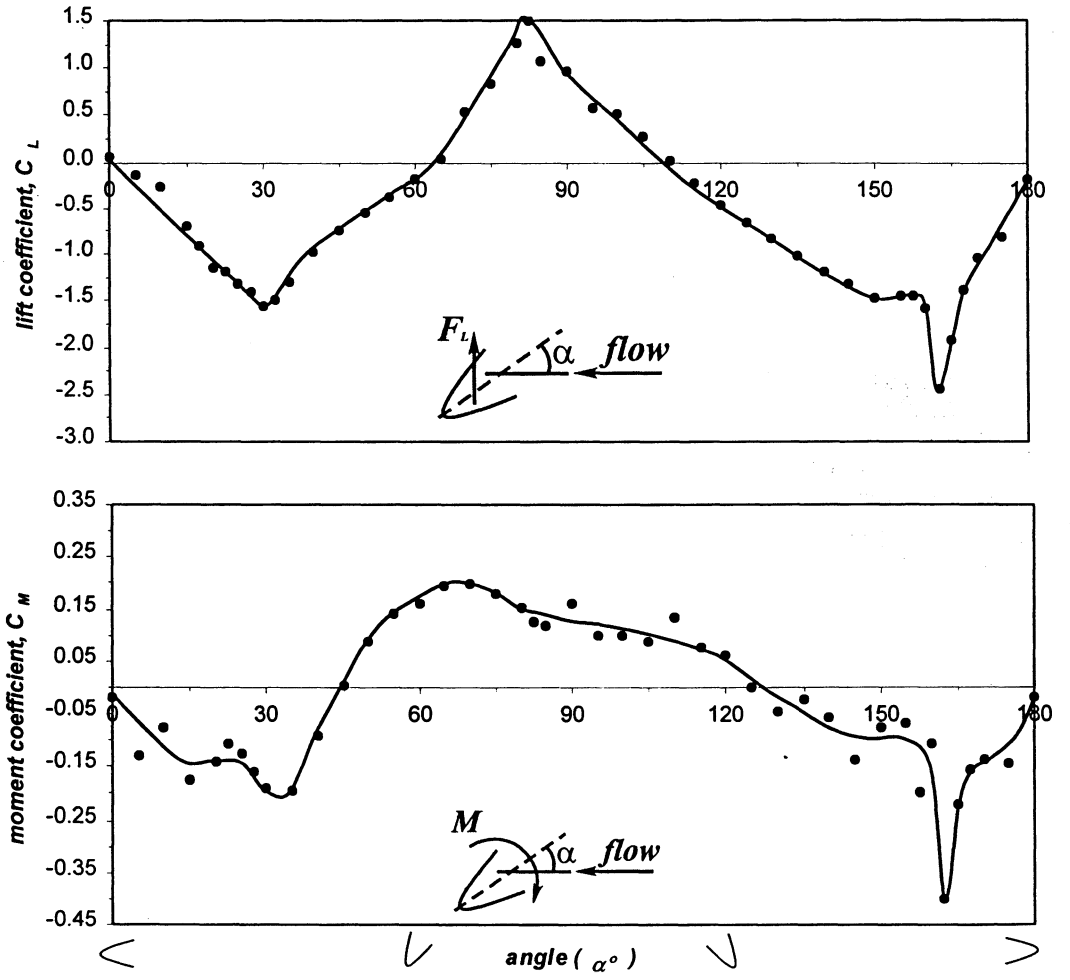

Figure 5.21

Parabolic cross-section model lift and moment coefficients

Reynolds number R_e = 26600

The lift and moment coefficients were measured in 5° increments, with 2.5° increments at the peak points. These results are presented in ***Figure 5.21***. In contrast to the semi-circular cross-section models, the lift and moment coefficients for the parabolic cross-section model had significantly different trends. This was a result of the difference in the after-body shape and size. Positive and negative peak values corresponded to angles of attack, α = 82.5° and α = 30°, respectively. Also, there was another negative peak at the angle of attack α = 162.5°. Sudden changes in the lift and moment coefficients at angles of attack α = 30° and α = 162.5° were attributed to the flow reattachment to the model after-body.

The Strouhal number variation as a function of angle of attack is presented in ***Figure 5.22***. Sudden changes in the Strouhal number were related to the lift and moment coefficient peak values, and, therefore, related to the flow reattachment to the model after-body.

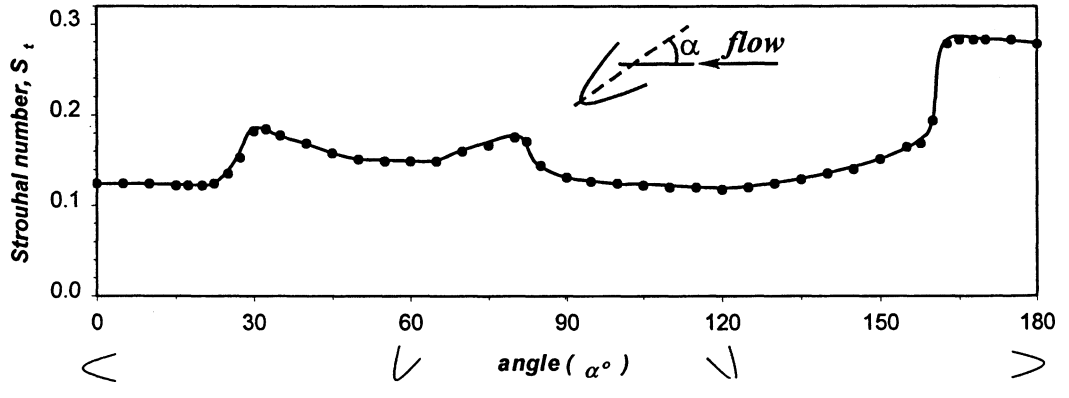

Figure 5.22

Strouhal number as a function of parabolic cross-section model angle of attack for Reynolds number R_e = 26600

5.4 Dynamic response with the model elastic axis behind the centre of gravity

To replicate the mixing blade combined plunge and torsion motion, the model elastic axis position was changed after the first group of the dynamic experiments. For the pure plunge dynamic response investigation, the model elastic axis position coincided with the model centre of gravity. To couple the plunge and rotational motion, the model elastic axis position was moved behind the model centre of gravity, as depicted in ***Figure 3.10***. The change in the elastic axis location resulted in the change of the model motion from the pure plunge to the combined plunge and rotational model motion.

The dynamic experiments were repeated for two different model elastic axis positions, 50 mm and 95 mm behind model centre of gravity, respectively. The 50 mm model elastic axis position corresponded to a point between the mixing blade shear centre and the tip of the mixing blade cross-section. The 95 mm model elastic axis position corresponded stream-wise to the point behind both the mixing blade tip and the mixing blade shear centre.

The open semi-circular, semi-elliptical and parabolic models were investigated in these experiments. Since it was determined that there was no difference in the dynamic response between the open and closed semi-circular cross-section models, the latter was not investigated.

The test set-up characteristics retained the same value for the elastic beam length, 65 mm. The frequencies and stiffness for different models corresponded accordingly.

The combined plunge and rotation mode amplitude and frequency, together with the vortex shedding frequency were monitored.

5.4.1 Open semi-circular cross-section model

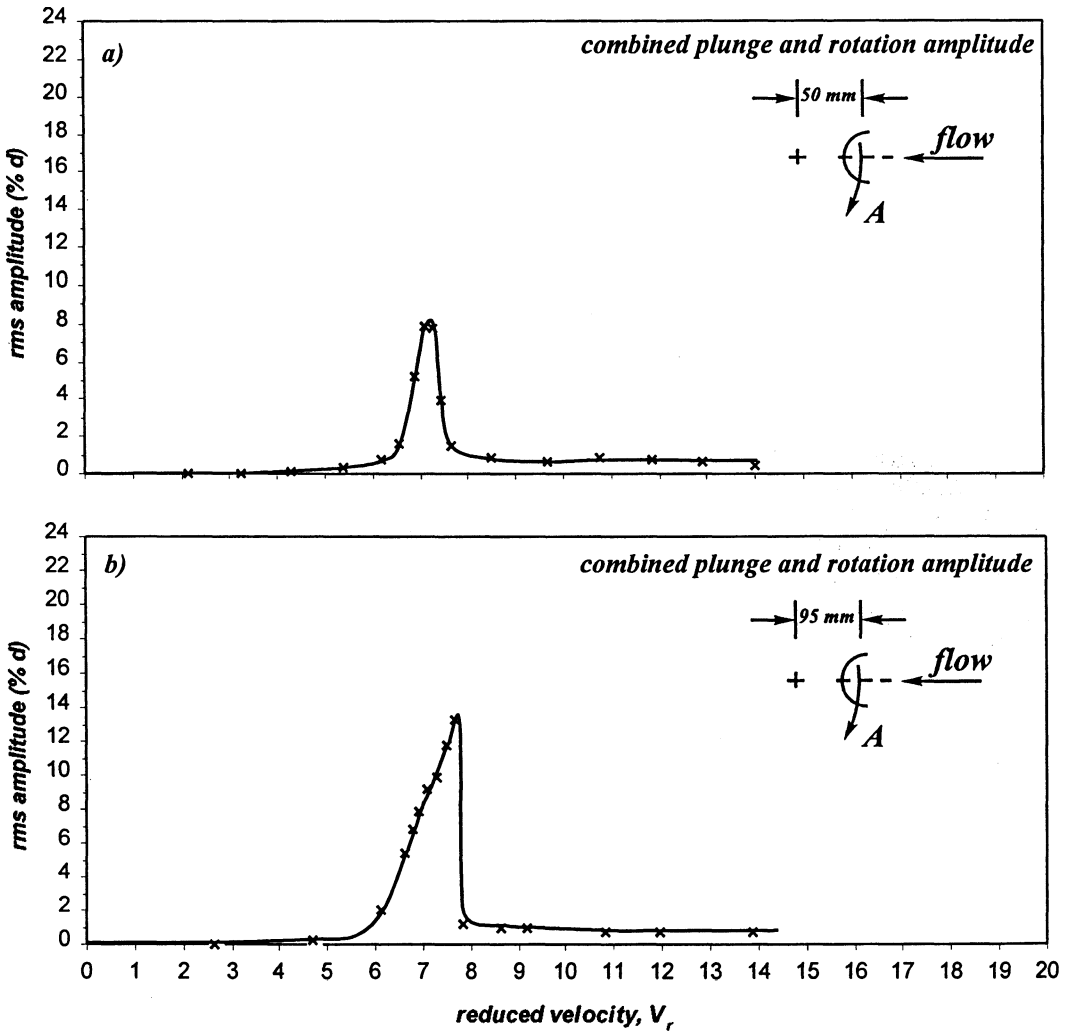

Figure 5.23

Semi-circular cross-section model dynamic response:

a) elastic axis 50 mm behind the centre of gravity,

b) elastic axis 95 mm behind the centre of gravity

Figure 5.23 presents the combined plunge and rotational amplitude response to the flow excitation for two different model elastic axis positions. With the elastic axis 50 mm behind the model centre of gravity, the dynamic response of the semi-circular model did not change significantly compared to the elastic axis position coinciding with the centre of gravity. The amplitude peak value for the reduced velocity V_r = 7, where vortex shedding frequency coincided with the model natural frequency, was 7% of the characteristic width *d*. With the vortex shedding frequency higher than model natural frequency, the amplitude dropped to less than 1% *d*. No galloping was observed for this support set-up.

With the elastic axis position changed to 95 mm behind the model centre of gravity, the vortex shedding resonant amplitude increased to 13% *d*. The dynamic response during resonance was significantly influenced by small changes in the flow velocity. This response might be considered as galloping, triggered by large vortex shedding resonance amplitude. However, with flow increase, the vortex shedding excitation coupled with the cross-section aerodynamic characteristics was not sufficient to support further increase in the amplitude, which suddenly dropped to the turbulence excitation response level. At flow velocities above vortex shedding resonance, the turbulence excitation amplitude was not large enough to trigger galloping.

5.4.2. Semi-elliptical model

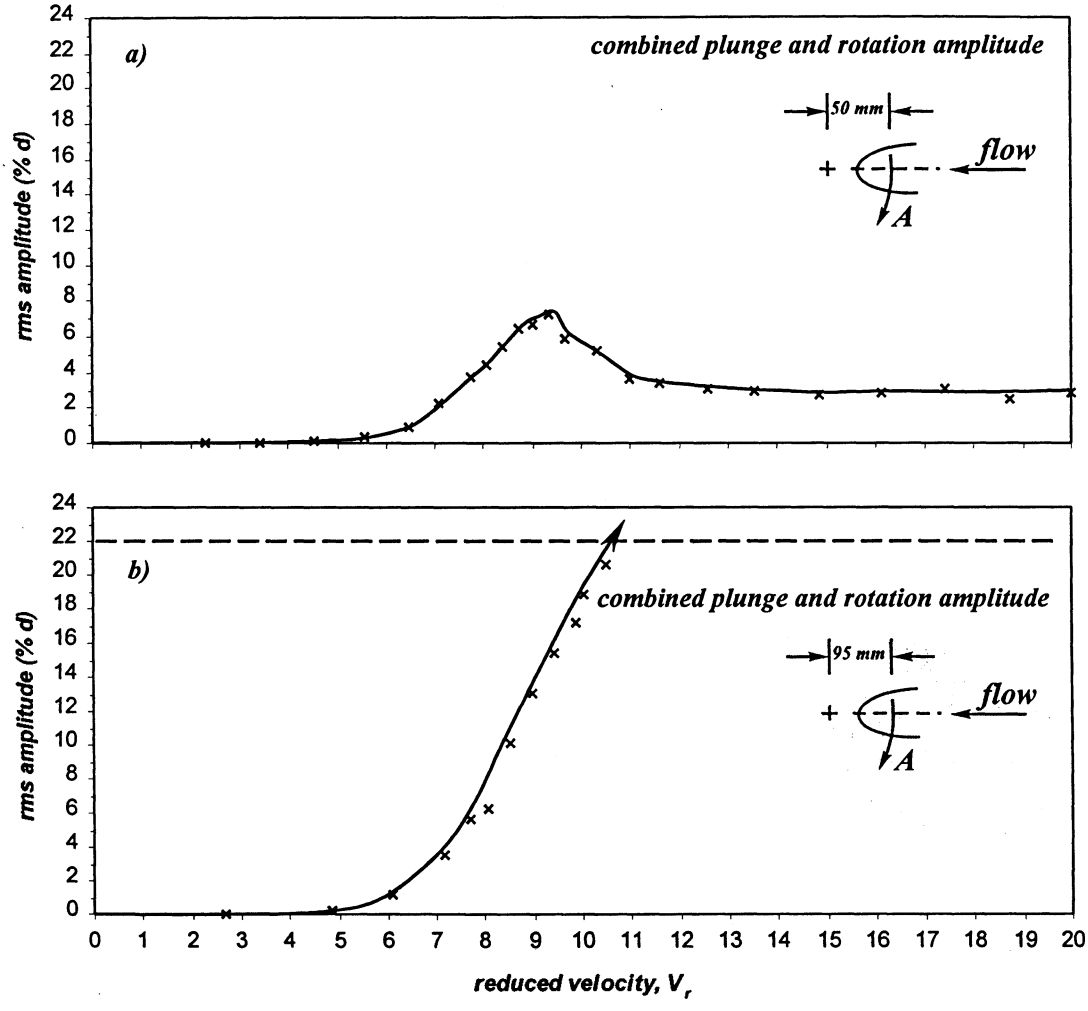

Figure 5.24

Semi-elliptical cross-section model dynamic response:

a) elastic axis 50 mm behind the centre of gravity,

b) elastic axis 95 mm behind the centre of gravity

The semi-elliptical cross-section model was tested under the same conditions as the semi-circular model. The response to the flow excitation is presented in ***Figure 5.24***. The change in the model elastic axis to 50 mm behind the centre of gravity did not induce a significant change in the peak response amplitude at resonance due to vortex shedding. The turbulence excitation for flow velocities exceeding vortex shedding resonance resulted in the amplitude values of approximately 3% *d*. Galloping was not observed for this support set-up. Interestingly, when the model elastic axis position was changed to 95 mm behind the centre of gravity, vortex shedding resonance triggered galloping. With a small increase in flow velocity, the amplitude increased significantly, reaching the test set-up limit of 22% *d* (***Figure 5.24b***).

To further investigate the galloping phenomenon, the experiment was repeated with the model restrained at its initial non-oscillating position. The flow velocity was increased above the value corresponding to the vortex shedding resonance, and then the model was released. Oscillations started from rest and reached the test set-up limit amplitude in seconds, depending on the model mass (with or without the added lead weight). This type of experiment was repeated for several flow velocities up to a reduced velocity of $V_r = 20$. The same model behaviour was detected.

5.4.3 Parabolic model

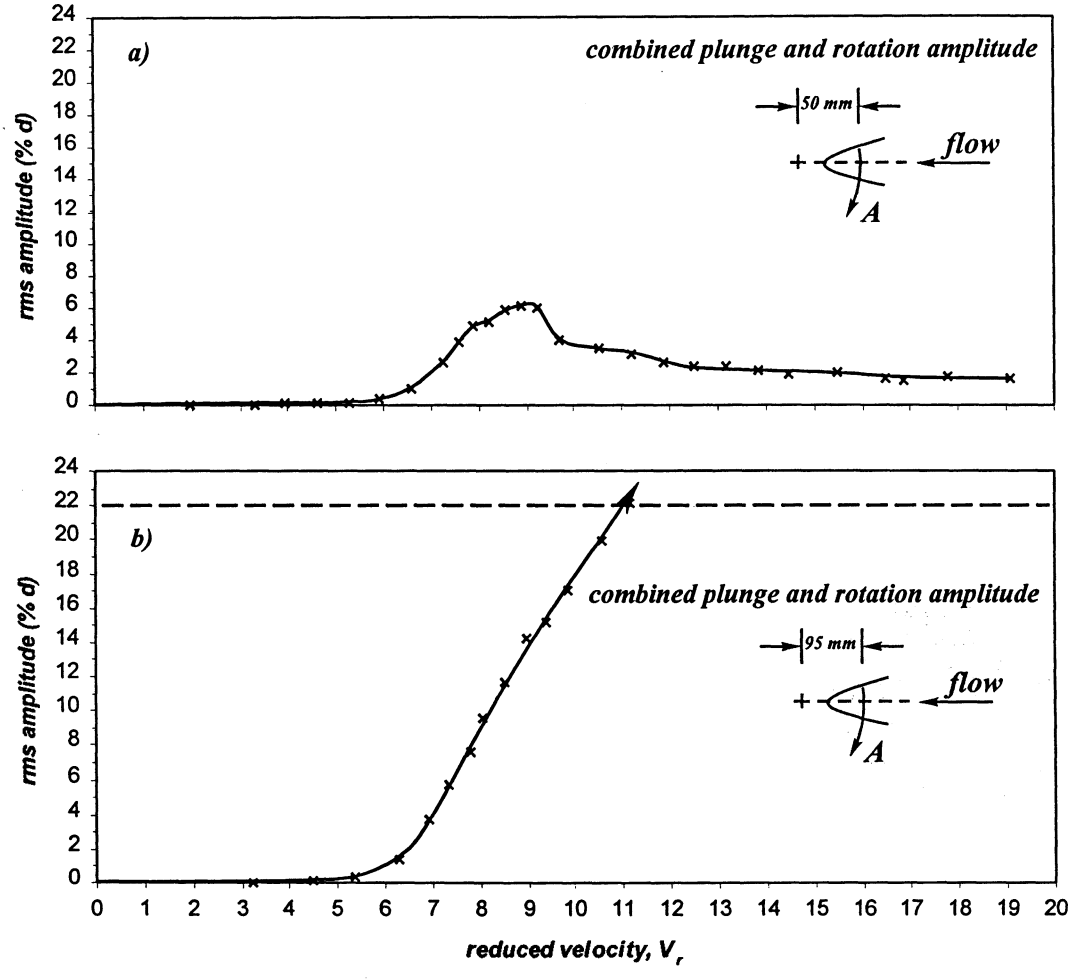

Figure 5.25

Parabolic cross-section model dynamic response:

a) elastic axis 50 mm behind the centre of gravity,

b) elastic axis 95 mm behind the centre of gravity

The parabolic cross-section model response resembled the semi-elliptical cross-section model, as shown in ***Figure 5.25***. For the test set-up where the elastic axis was 50 mm behind the model centre of gravity, significant vortex shedding excitation started at a reduced velocity $V_r = 6$. The vortex shedding resonance peak was broad. When the vortex shedding frequency was close to, or the same as, the model natural frequency, the oscillations were periodic. However, the oscillating motion had amplitude bursts for the flow velocity range above that corresponding to vortex shedding resonance. In the flow velocity range corresponding to values above vortex shedding resonance, the model response amplitude to turbulence excitation was approximately 2.5% *d*. No clear galloping was detected during the experiments for this support set-up.

When elastic axis position was changed to 95 mm behind the model centre of gravity, galloping was induced by the vortex shedding resonance amplitude, as depicted in ***Figure 5.25b***. When the model was set free at flow velocities above vortex shedding resonance, oscillations started from the rest, reaching the test set-up limit of 22% *d*.

There was a significant response difference between the set-up where the model elastic axis coincided with the centre of gravity and the set-up where the model elastic axis was behind the centre of gravity. Unlike the former set-up, the latter resulted in coupling of the rotational and plunge motion. This rotational motion induced a relative angle of attack between the cross-section and the flow direction. Since the change in the model elastic axis position was the only difference between the two set-ups, this suggests that rotational motion combined with a sufficient triggering amplitude provided by vortex shedding resonance excitation was responsible for the galloping.

5.5 Modified parabolic cross-section model dynamic response with the model elastic axis 95 mm behind the centre of gravity

The parabolic cross-section was modified in an attempt to remove galloping from the model dynamic response. The model characteristic width d was increased by 20% and 40%, respectively, by adding fins at the cross-section separation points, as presented ***Figure 3.5***. The purpose of adding the fins was to increase the wake region and prevent reattachment of the flow, thus changing the wake fluid structure sufficiently to eliminate galloping.

The parabolic cross-section model dynamic response for the different fin heights is presented in ***Figure 5.26***. The amplitudes on the diagrams are expressed as a percentage of the modified model characteristic width d_m (120% and 140% d, respectively). Although galloping was not induced by the vortex shedding, oscillation amplitudes of almost 9% d_m were present at the flow velocities above those corresponding to vortex shedding resonance. The amplitudes plotted in this region represent time averaged values as the oscillations were marked with irregular bursts in amplitude. Thus, while the fins prevented galloping response, they did produce large amplitude vortex excited oscillations.

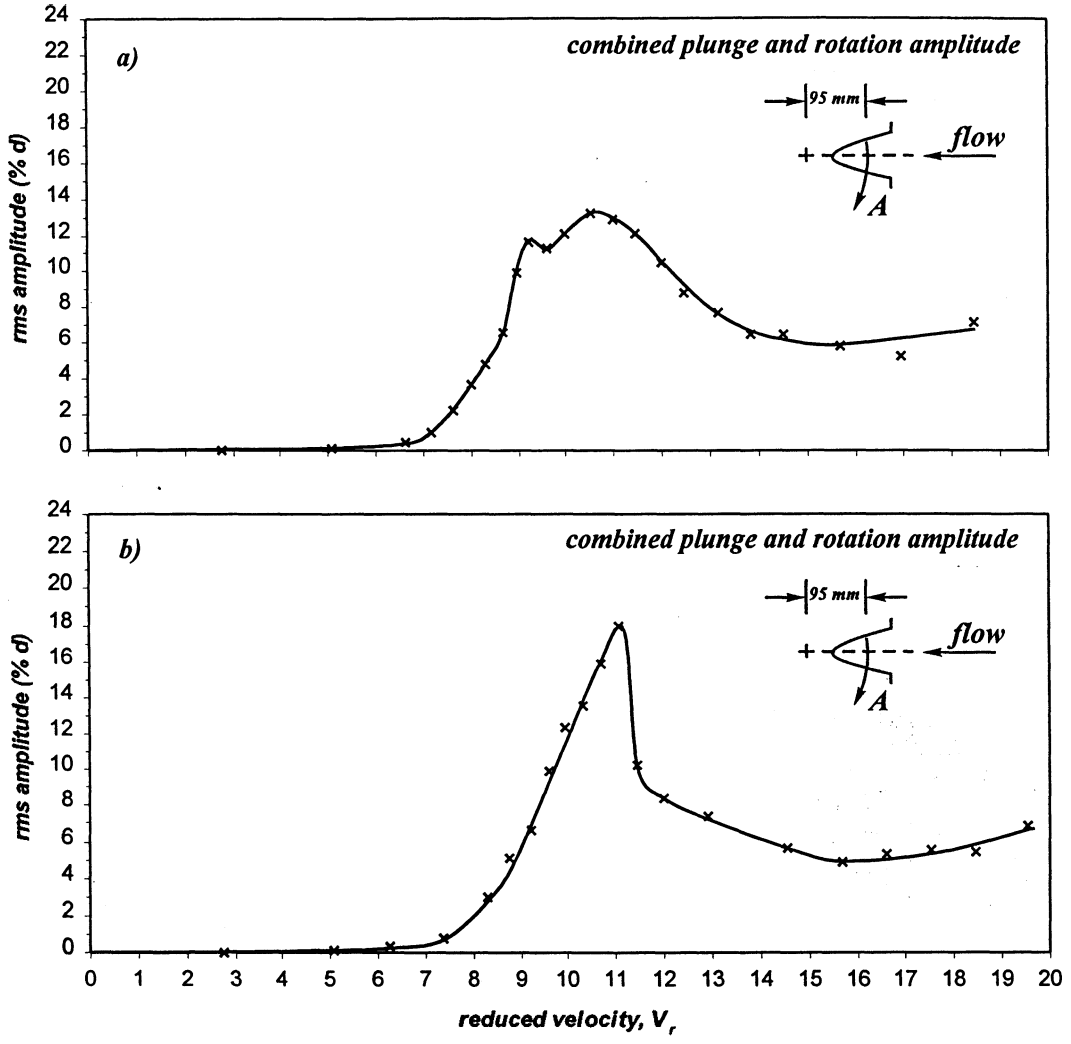

Figure 5.26

Parabolic cross-section model dynamic response

with elastic axis 95 mm behind the centre of gravity:

a) 0.1d fins added to the separating edges,

b) 0.2d fins added to the separating edges

Chapter 6

Conclusions and recommendations

motivated by a problem that occurred in the chemical
ing blade in a large mixing vessel brought attention to the
cross-section to flow-induced vibrations. The intention of
interaction of a parabolic cross-section bluff body with the
ained to alter the dynamical behaviour of the mixing blade.

earch

netric characteristics of the mixing blade motivating the
ross-section models, parabolic, semi-circular and semi-
ed. The results from the semi-circular cross-section model,
d for comparison with results published in the literature.

The semi-elliptical model was compared with the parabolic model to determine the response differences when small geometry changes were introduced to the cross-sectional shape.

In spite of the highly three-dimensional dynamic response of the mixing blade structure, a decision was made to build two-dimensional "sectional" models. This ensured better control over the test model mode shapes and corresponding frequencies as well as eliminated the complex three dimensional flow conditions of the prototype blade. The experimental set-up allowed the model elastic axis to be changed relative to its centre of gravity, consequently enabling a coupled plunge and torsional mode. This set-up feature was necessary to model the mixing blade complex vibration response. Another property that added to the versatility of the experimental set-up was the possibility of changing the model angle of attack to the flow. All these characteristics were used in the dynamic and static experiments performed. During the experiments, the Reynolds number ranged from 10^4 to 10^5.

In the static experiments, the lift force and moment were monitored with respect to the model angle of attack to the incoming flow. Also, under the same conditions, the frequency spectrum of the wake response was monitored. The lift and moment coefficients together with the Strouhal number were calculated from the monitored values.

The dynamic experiments revealed information on the model response to the flow excitation. With the model elastic axis coinciding with the model centre of gravity, the dynamic experiments were conducted on all models. With the elastic axis moved behind

the centre of gravity, the experiments were repeated for the open semi-circular, semi-elliptical and parabolic cross-section models. In the attempt to modify the dynamic response of the parabolic model, its cross-section geometry was modified and the dynamic experiments repeated.

6.2 Conclusions

The following conclusions may be drawn from the experiments preformed on the semi-circular cross-section model:

- The Strouhal number was independent of the Reynolds number for the observed range 10^4-10^5. The closed and open cross-sections had the same Strouhal number value of $S_t = 0.15$. With this Strouhal number, a coincidence between the vortex shedding and the plunge frequency occurred at a reduced velocity $V_r = 6.67$.
- The closed semi-circular lift coefficient values in the vicinity of the angle of attack values $\alpha = 45°$ and $\alpha = 90°$ were found to be highly influenced by a change in the Reynolds number. The lift coefficient value decreased with an increase in the Reynolds number.
- In contrast to the open semi-circular cross-section, the closed semi-circular section lift coefficient values were less dependent on the Reynolds number, although angles of attack associated with abrupt change in these coefficients with Reynolds number were the same.

- With the Reynolds number close to the 10^5, the closed and open semi-circular cross-section lift coefficients near an angle of attack $\alpha = 45°$ differ by about 30%. This is presented in ***Figure 6.1***.

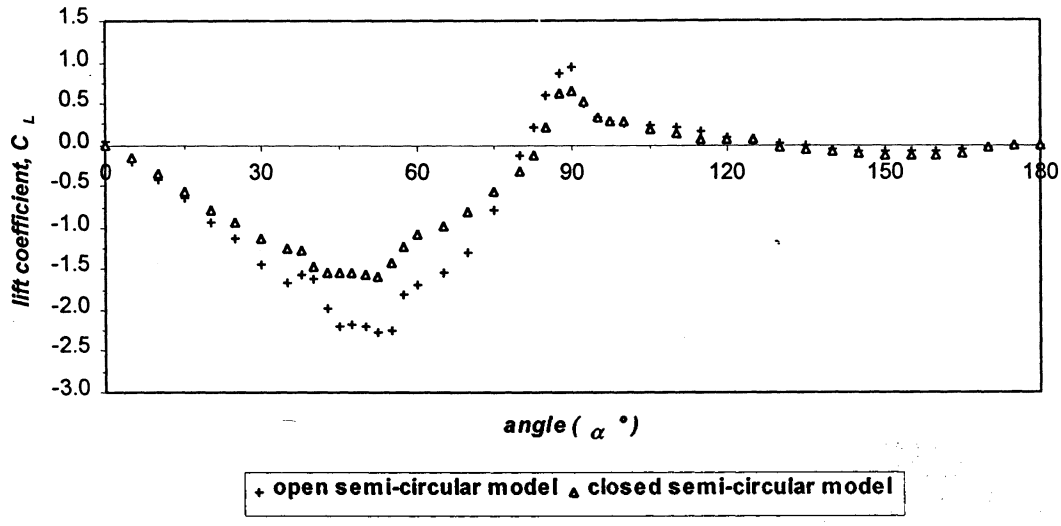

Figure 6.1

Comparison of closed and open semi-circular cross-section model lift coefficients, with the Reynolds number value close to 10^5

- Neither the closed nor the open semi-circular cross-section galloped from rest within investigated flow velocity range, when the model elastic axis coincided with the centre of gravity. Novak and Tanaka (1974), showed that a semi-circular shape in flow behaves like a hard oscillator i.e. it gallops only if sufficient triggering amplitude is introduced above the critical flow velocity.

- With the model elastic axis 95 mm behind the centre of gravity, the open semi-circular model dynamic response showed a limited increase in the oscillating amplitude with flow velocity increase. The oscillation amplitude increased up to 14% d at $V_r = 8$ and then suddenly dropped to 1% d. The lack of a sufficient after-body may have prevented further increase in the oscillation amplitude.

The conclusions drawn from the experiments on the semi-elliptical and parabolic cross-section models are as follows:

- The static experiments showed an insignificant difference in the lift coefficient trend between the semi-elliptical and parabolic section models. However, there was a difference in the moment coefficient trend between the two models (see ***Figure 5.17*** and ***Figure 5.21***).
- The Strouhal numbers for the semi-elliptical and parabolic models differed slightly (0.12 and 0.13 for the elliptical and parabolic section respectively), due to the after-body differences. The Strouhal number was constant, within the Reynolds number range 10^4-10^5.
- In the plain plunge dynamic experiments, galloping did not occur in either of the two models. With the model elastic axis moved 95 mm behind the centre of gravity, both models galloped. The galloping instability coincided with the vortex shedding resonance. With the flow velocity above the corresponding vortex shedding resonance

velocity, galloping started from rest, leading to the conclusion that a combined plunge and torsional motion, introduced by the change in the elastic axis position, was responsible for the onset of galloping.

- The fin modifications that were applied to the parabolic cross-section did not produce the desired effect, i.e. while galloping was prevented, the vortex excited oscillation amplitudes remained at an unacceptable level for the mixing blade design.

6.3 Recommendations

A continuation of the present research would benefit from changes in the current test set-up. The experimentally determined damping value of 1% is in the upper range of the values found in many modern structures. Modi and Slater (1994) changed the critical velocity for the onset of galloping by introducing a different model support damping. This resulted in the separation of vortex-induced and galloping vibrations. This principle could facilitate the separation of the coincident vortex shedding and galloping vibrations in the dynamic experiments with the model elastic axis 95 mm behind the centre of gravity.

Comparison of the semi-circular, semi-elliptical and parabolic model lift coefficients as a function of angle of attack, ***Figure 6.2***, shows that the lift coefficient gradient for the three different models at the angle of attack $\alpha = 0°$ is similar. Since the semi-circular section did not gallop, comparison in ***Figure 6.2*** implies that the semi-

elliptical and parabolic models would also not gallop, as was later observed in the dynamic experiments. Finite-element analysis performed on the mixing blade structure suggested that the flow-induced instability occurs at the reduced velocity order of 1, as opposed to the reduced velocity $V_r = 7.5$ in the present experiments. This suggests there may be an influence on the mixing blade that was not taken into account in the experiments. That influence may be a high level of turbulence present in the mixing vessel fluid environment. Novak and Tanaka (1974), Novak and Davenport (1970), Bokaian and Geoola (1984), showed that turbulence has a large influence on the bluff body response to flow excitation. Repeating the experiments with different levels of turbulence intensity would be beneficial to a better understanding of the problem.

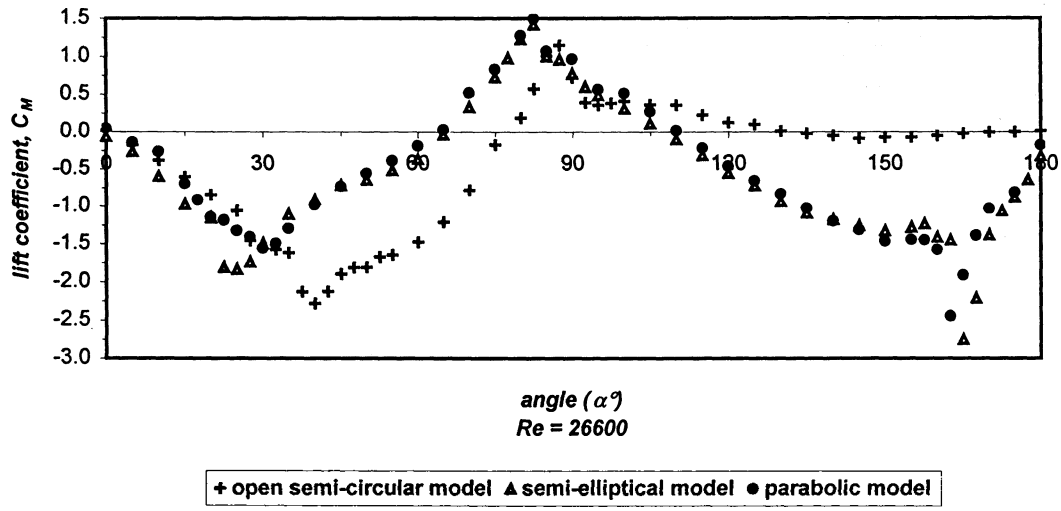

Figure 6.2

The lift coefficients for the open semi-circular, semi-elliptical and parabolic cross-section models at a Reynolds number $R_e = 26600$

Finally, with the introduction of turbulence, it would be useful to monitor force in the drag direction. With known lift, C_L, and drag, C_D, coefficients, the lateral force coefficient C_y for the semi-elliptical and parabolic sections could be determined. With information on the lateral force coefficient C_y and moment coefficient C_M, aerodynamic characteristics of these cross-sections would be complete, providing the information needed for the determination of the galloping, and consequently solving the problem of the flow induced vibrations of the mixing blade.

The present investigation, together with the recommendations for future research, may lead to a better understanding of the problem encountered in industry and increase reliability of the equipment. Thus, it may reduce the repair costs resulting from failures of the mixing blades and increase the efficiency of the chemical mixing process.

Appendix I - Mixing blade drawings

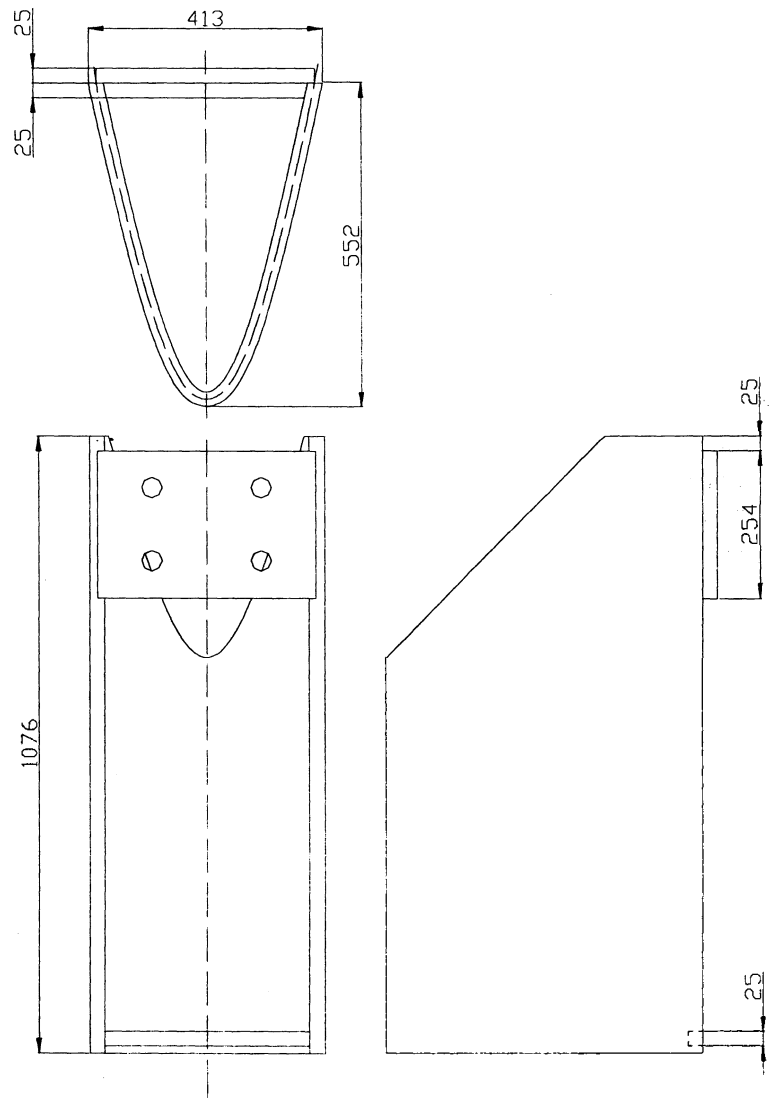

Figure A1.1

Mixing blade drawing with basic dimensions

Appendix II - Masses of the test set-up parts

Test set-up part	units	mass (grams)
semi-circular model	1	58
semi-elliptical model	1	122
parabolic model	1	108.5
endplate	2	16
connecting rod	2	21
supporting bar	2	51
protractor	2	10
angle profiles used for elastic beam clamping	8	2.5
bolts, nuts & other small parts	-	25
added mass, semi-circular model, m_{a1}	1	315
added mass, semi-elliptical & parabolic model, m_{a2}	1	300

Table A2.1

Masses of the test models with the support structure used in the calculations

semi-circular model, m_c	-	615
semi-elliptical model, m_e	-	650
parabolic model, m_p	-	665

Table A2.2

Appendix III - Hot wire and strain gauge calibration curves

Hot wire anemometry was used to measure flow velocity. To reduce error in the flow velocity measurements, hot wire was calibrated after every fifteen experiments. In ***Figure A3.1***, red line presents the calibration before the experiments started. Blue line presents the calibration after fifteen conducted experiments, while green line is the hot wire calibration curve after thirty experiments.

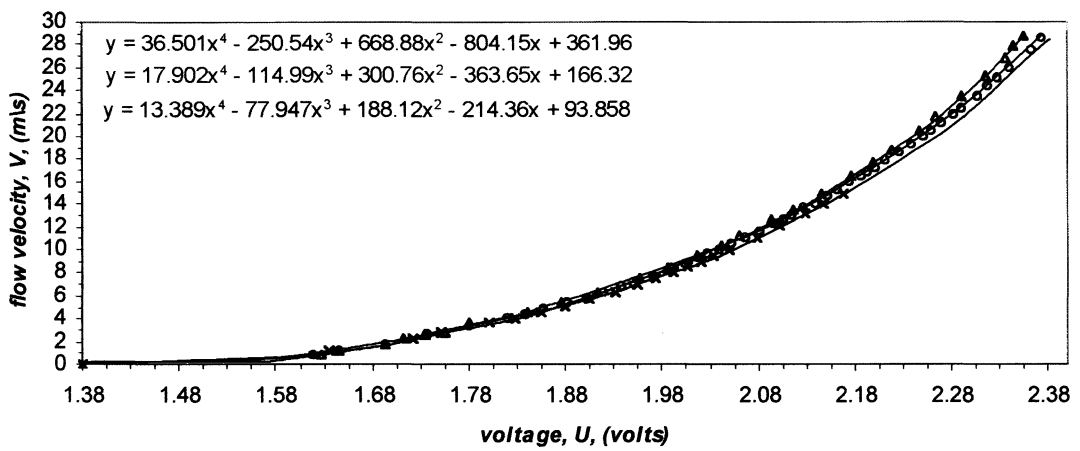

Figure A3.1

Hot wire calibration curves

Strain gauge calibration for dynamic and static experiments is presented on the following pages.

Closed and open semi-circular model

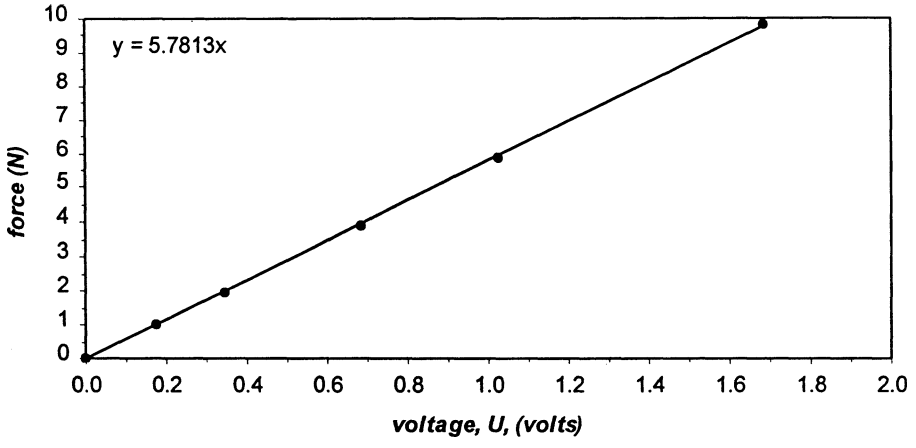

Figure A3.2

Plunge mode calibration curve

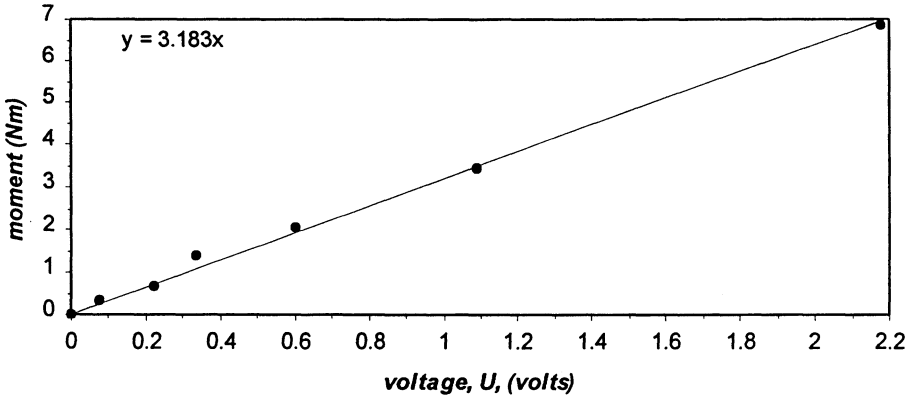

Figure A3.3

Rocking mode calibration curve

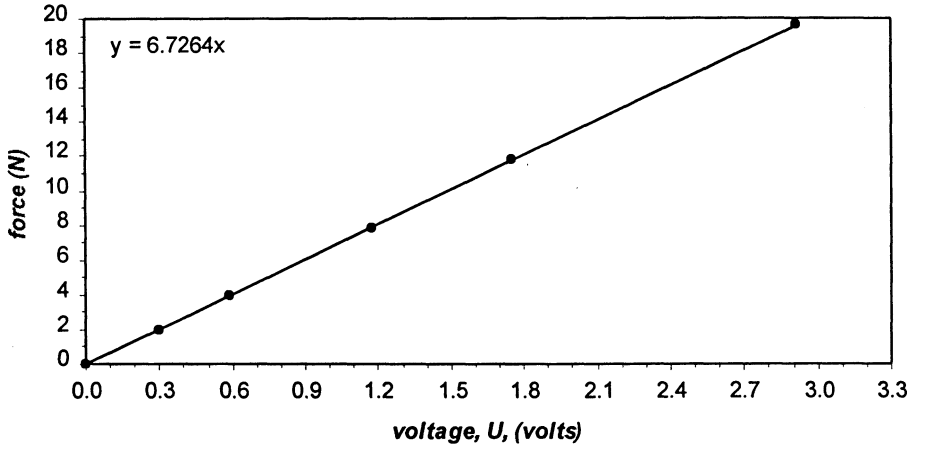

Figure A3.4

Lift force calibration curve, signals from two strain gauges on the same side of the model added and divided by two

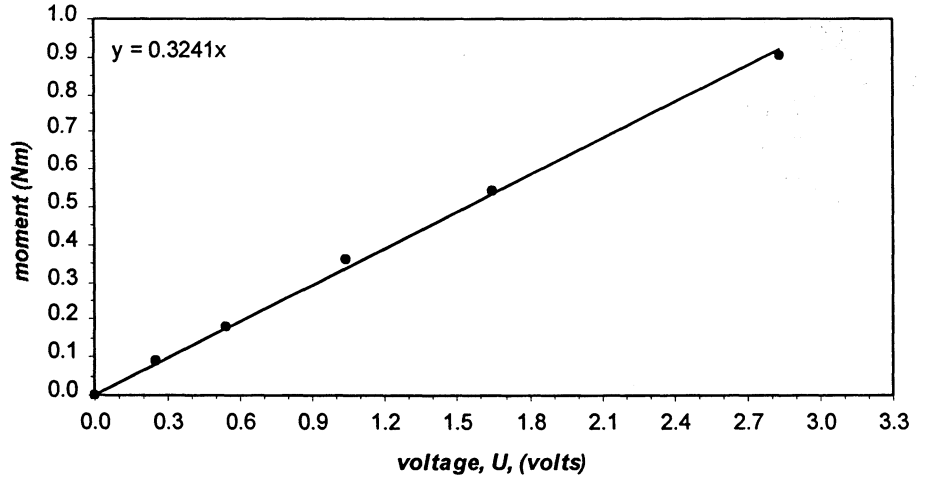

Figure A3.5

Fluid moment calibration curve, signals from two strain gauges on the same side of the model subtracted and divided by two

Semi-elliptic model

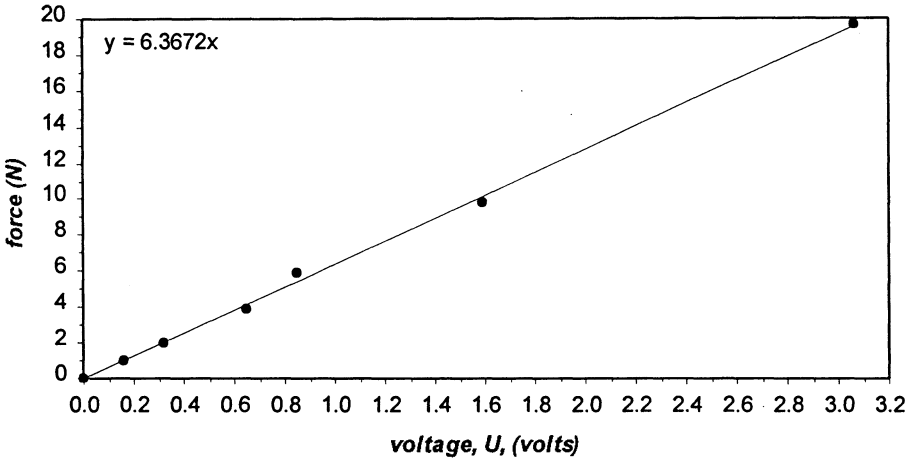

Figure A3.6

Plunge mode calibration curve

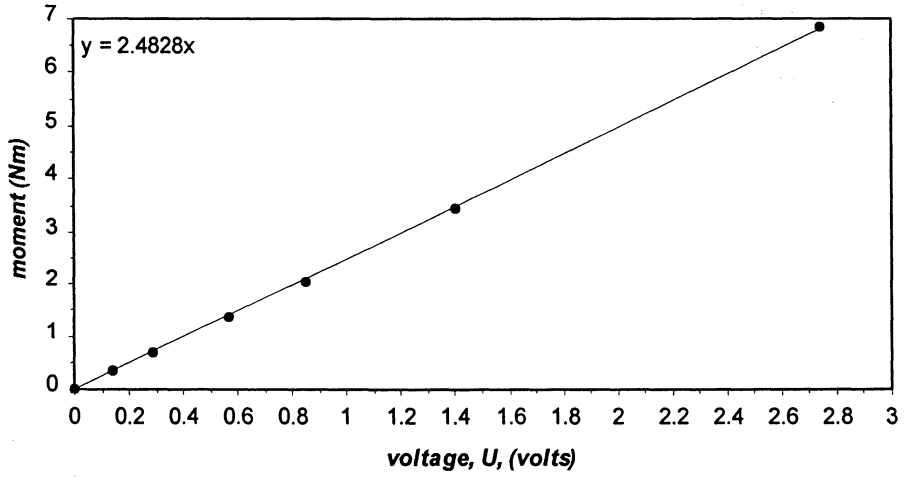

Figure A3.7

Rocking mode calibration curve

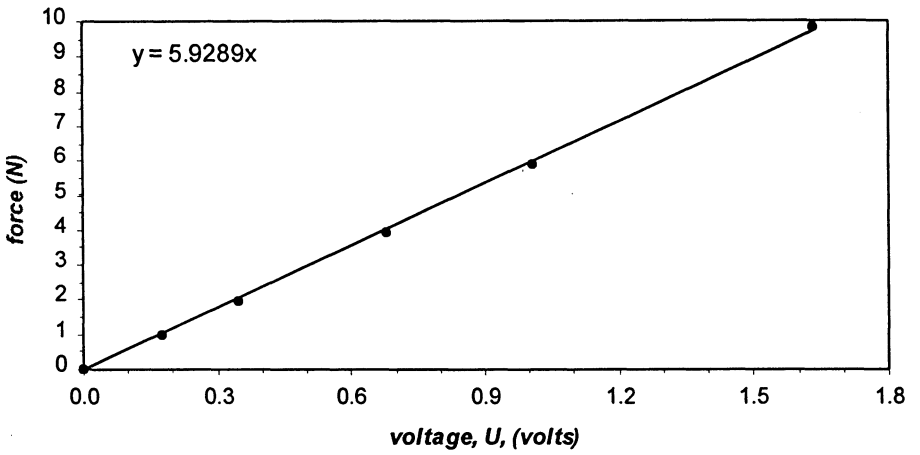

Figure A3.8

Lift force calibration curve, signals from two strain gauges on the same side of the model added and divided by two

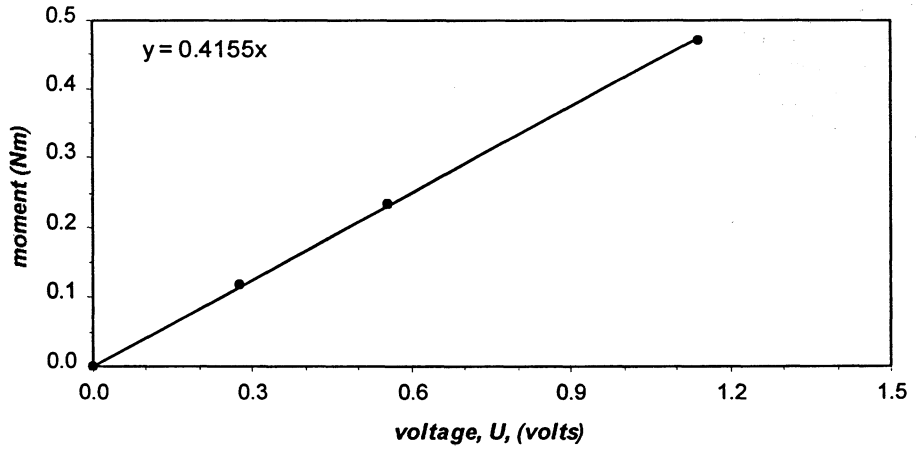

Figure A3.9

Fluid moment calibration curve, signals from two strain gauges on the same side of the model subtracted and divided by two

Parabolic model

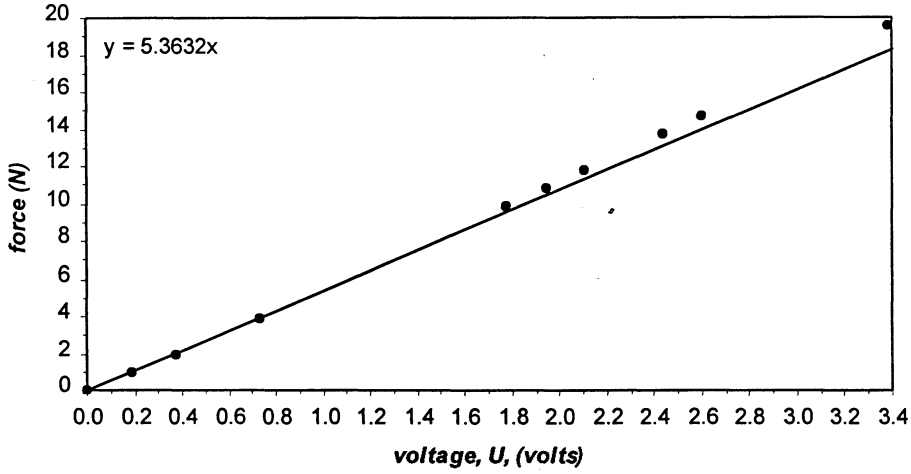

Figure A3.10

Plunge mode calibration curve

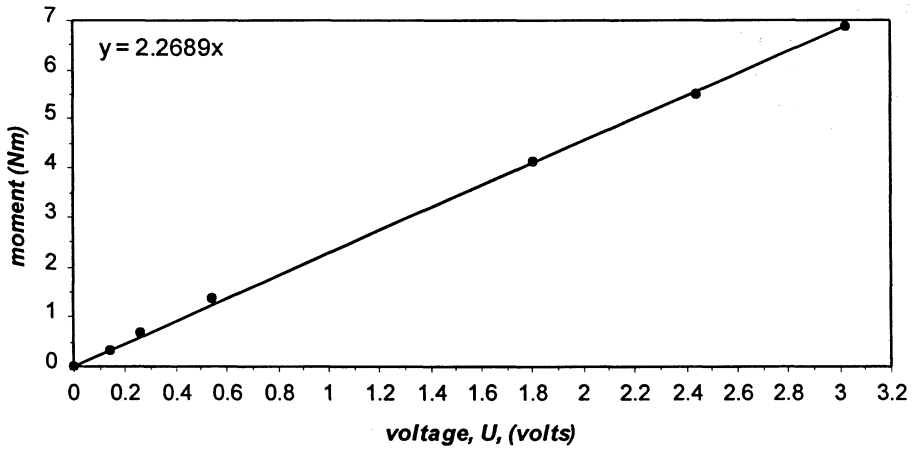

Figure A3.11

Rocking mode calibration curve

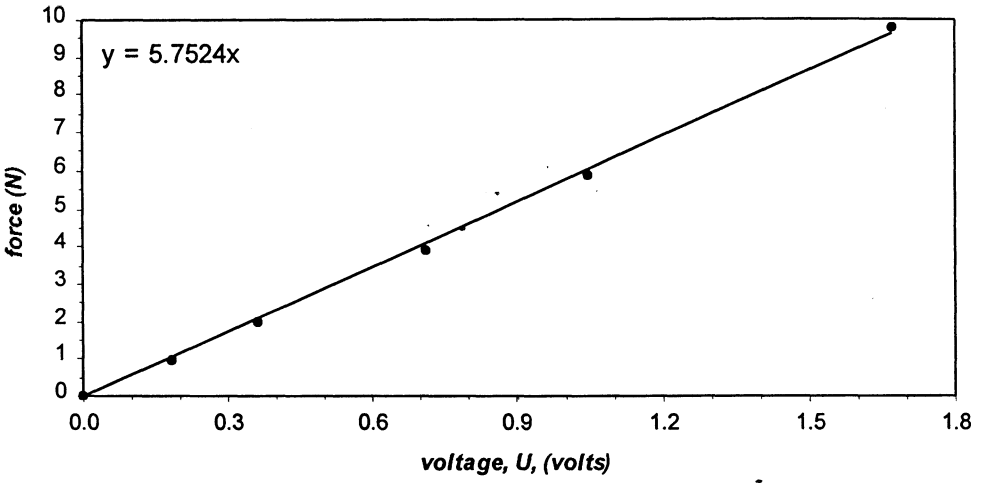

Figure A3.12

Lift force calibration curve, signals from two strain gauges on the same side of the model added and divided by two

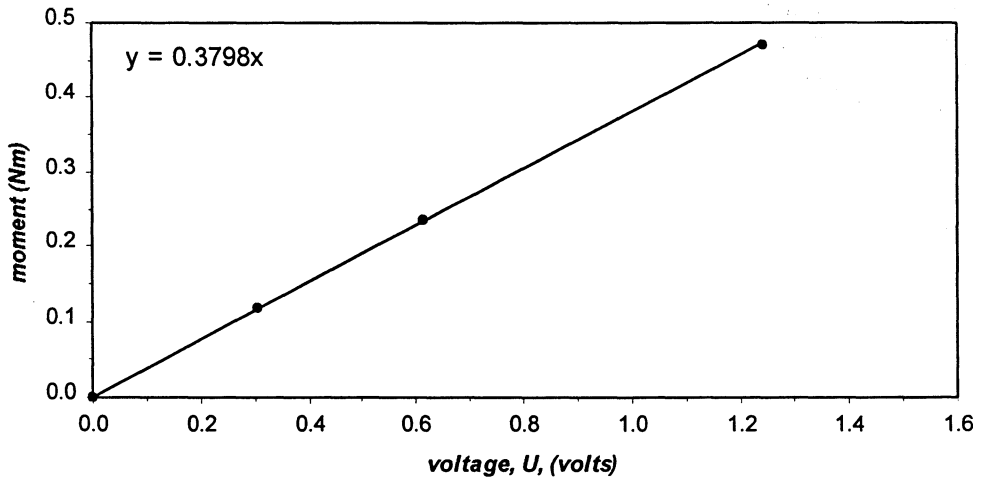

Figure A3.13

Fluid moment calibration curve, signals from two strain gauges on the same side of the model subtracted and divided by two

Appendix IV

Corrected and uncorrected lift and moment coefficients and Strouhal number for the closed and open semi-circular, semi-elliptic and parabolic models are presented here.

Closed semi-circular model

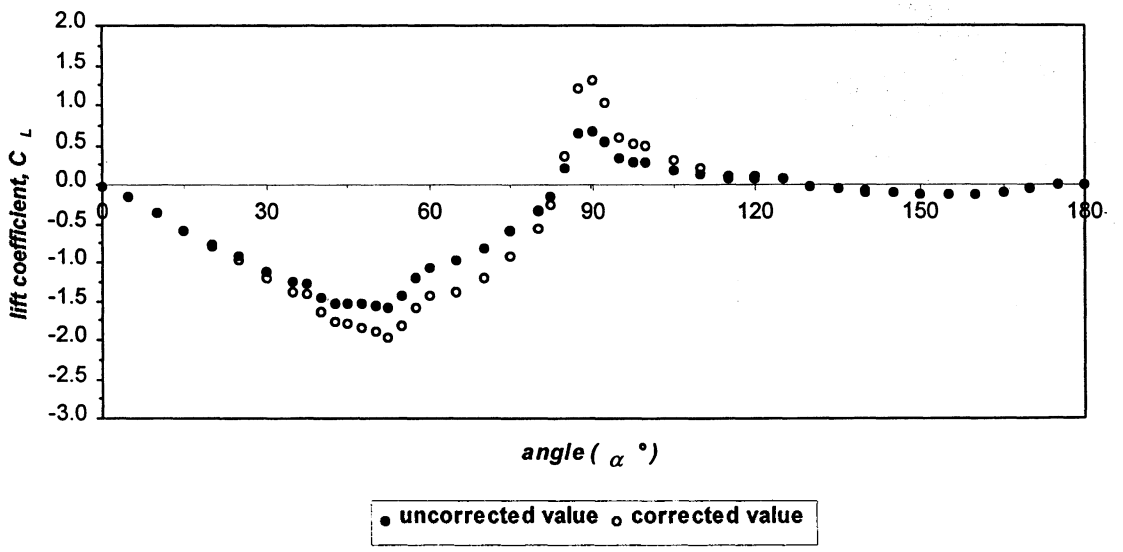

Figure A4.1

Uncorrected and corrected lift coefficient as a function of the model angle of attack at Reynolds number $R_e = 10^5$

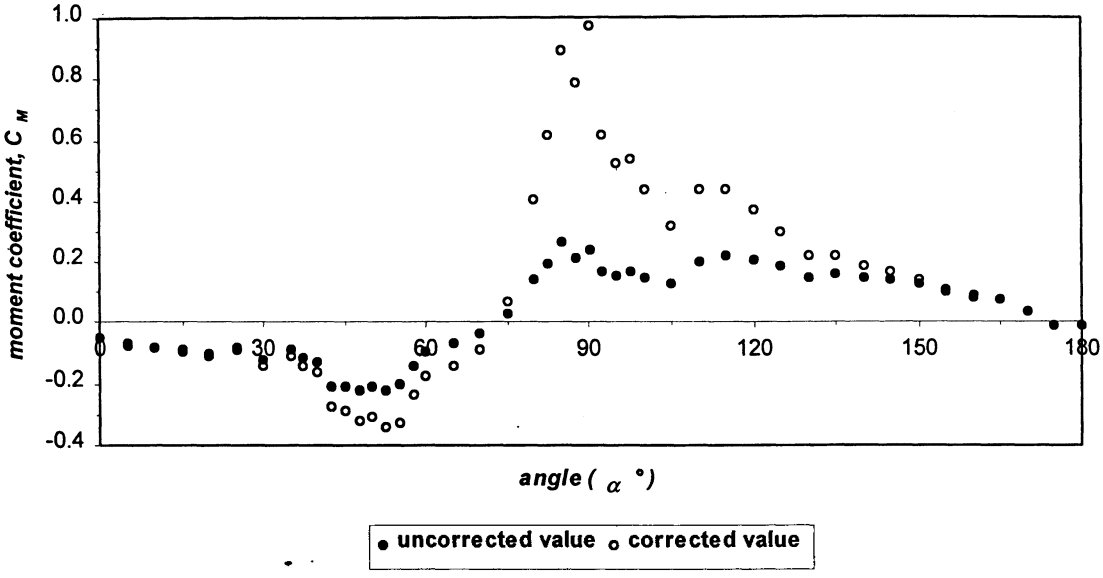

Figure A4.2

Uncorrected and corrected moment coefficient as a function of the model angle of attack at Reynolds number $R_e = 10^5$

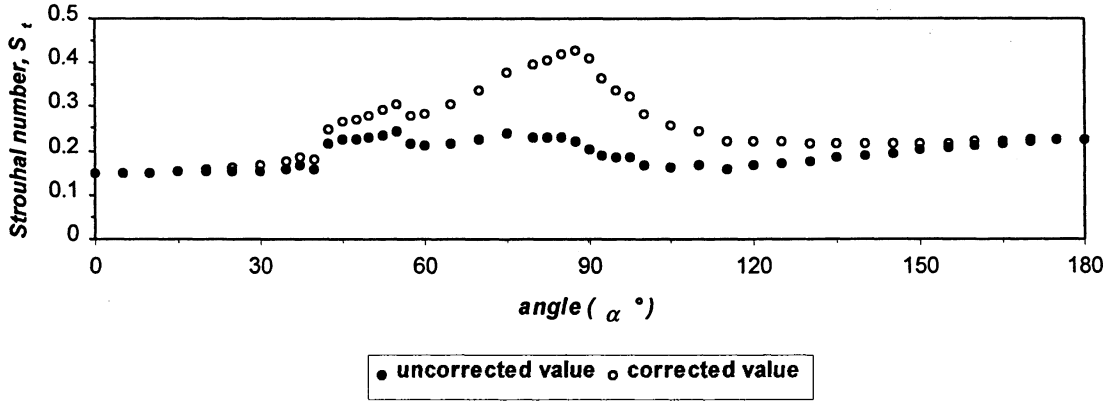

Figure A4.3

Uncorrected and corrected Strouhal number as a function of the model angle of attack at Reynolds number $R_e = 10^5$

Open semi-circular model

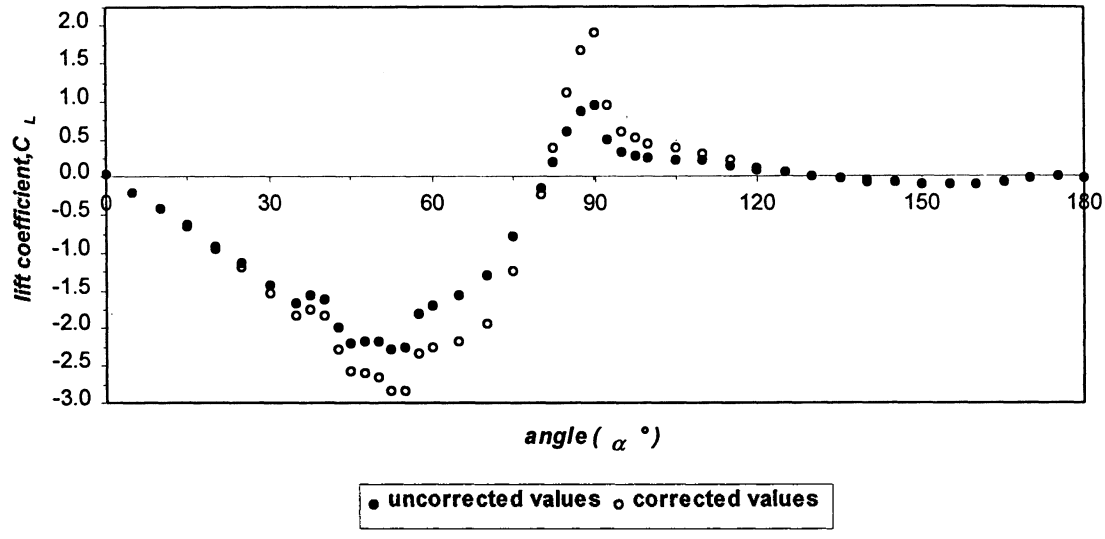

Figure A4.4

Uncorrected and corrected lift coefficient as a function of the model angle of attack at Reynolds number R_e = 82000

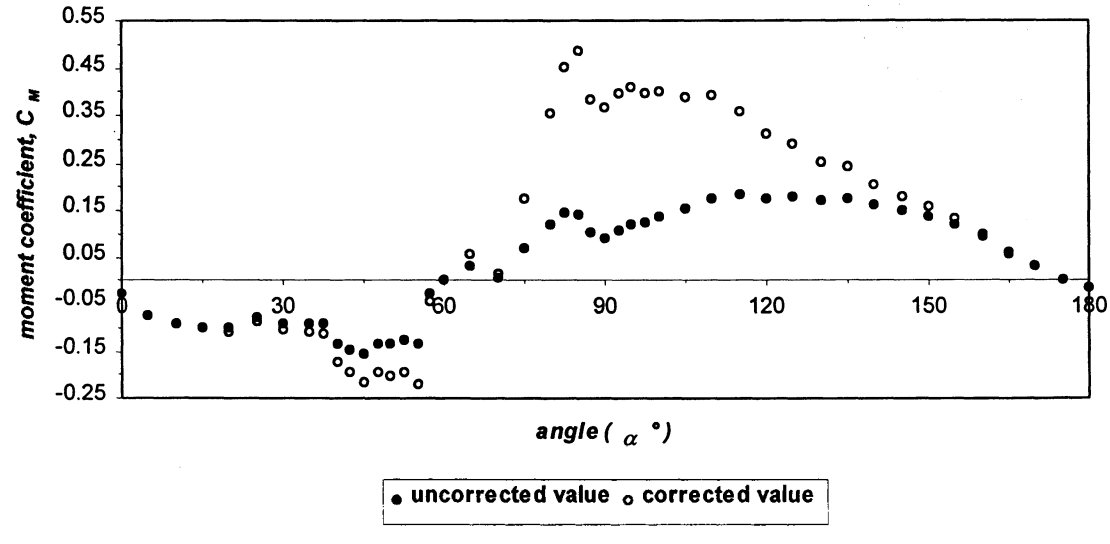

Figure A4.5

Uncorrected and corrected moment coefficient as a function of the model angle of attack at Reynolds number R_e = 82000

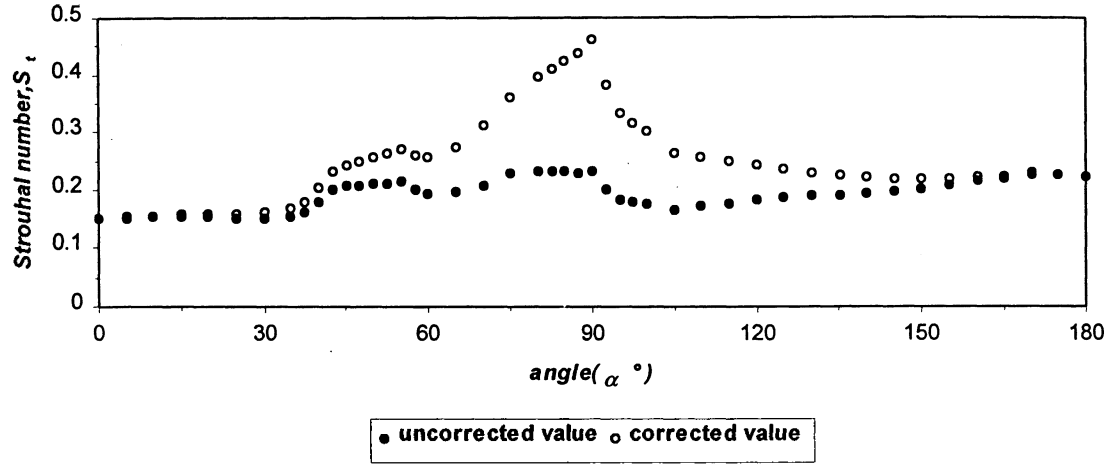

Figure A4.6
Uncorrected and corrected Strouhal number as a function

of the model angle of attack at Reynolds number R_e = 82000

Semi-elliptic model

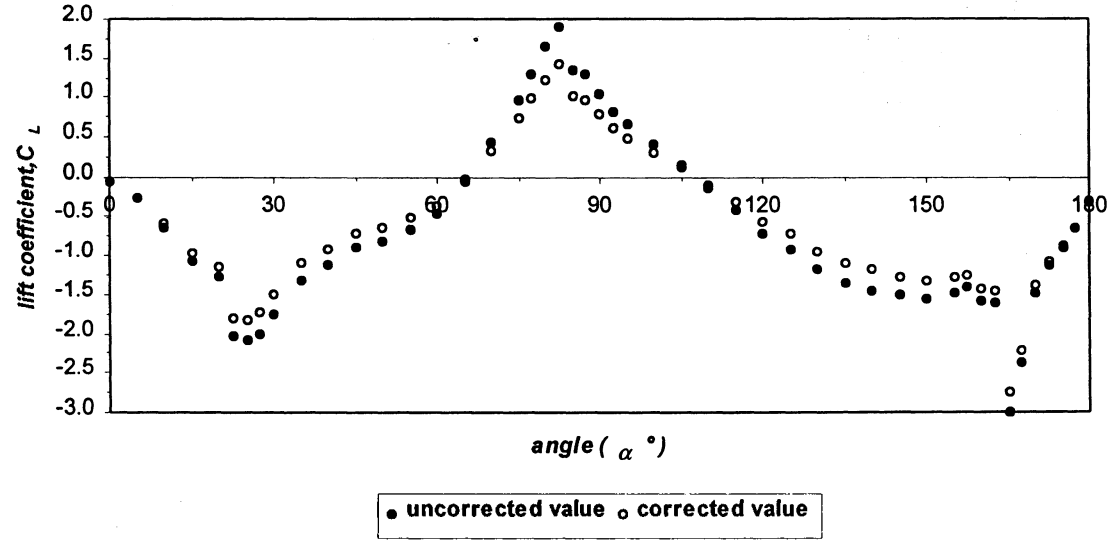

Figure A4.7

Uncorrected and corrected lift coefficient as a function

of the model angle of attack at Reynolds number R_e = 26600

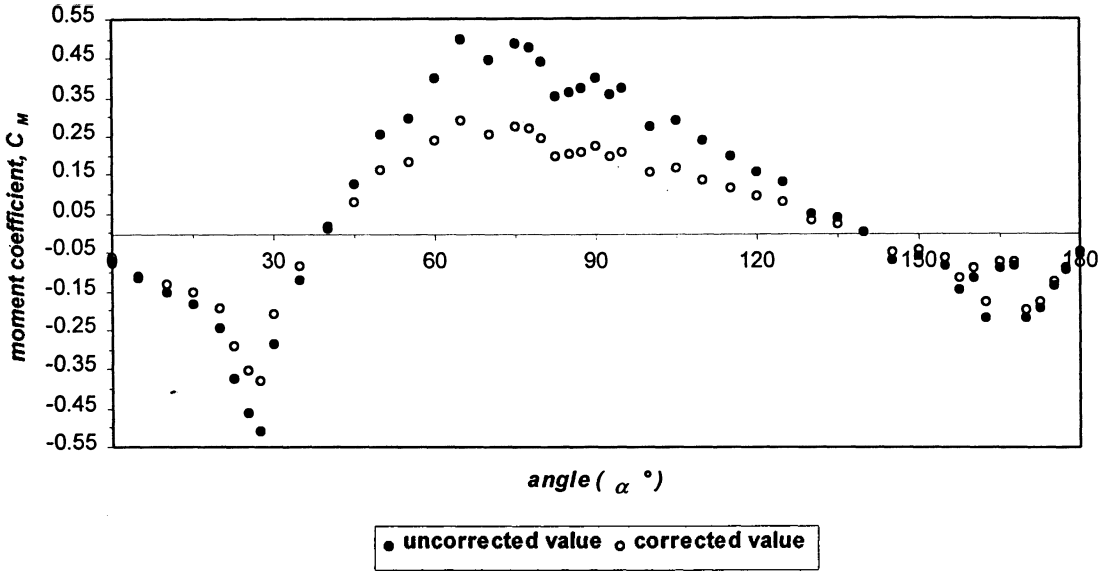

Figure A4.8

Uncorrected and corrected moment coefficient as a function of the model angle of attack at Reynolds number R_e = 26600

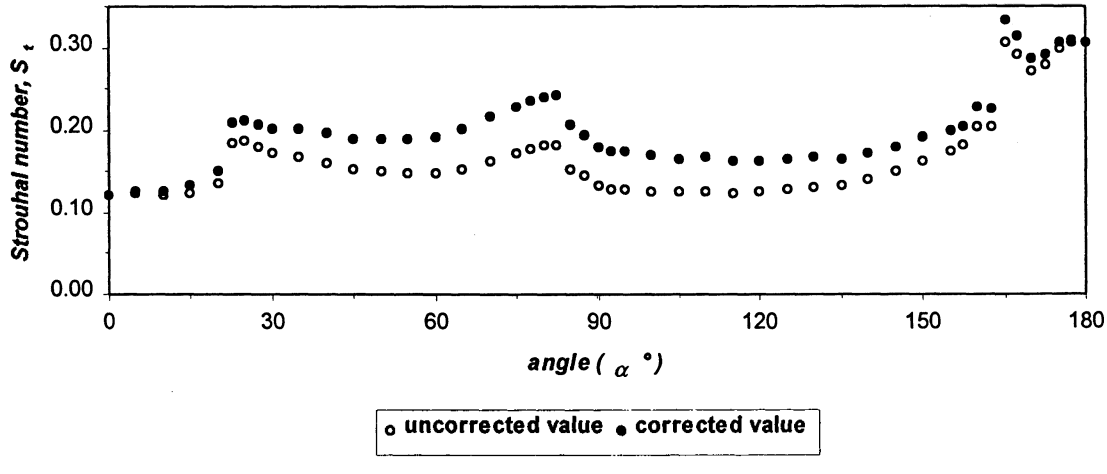

Figure A4.9

Uncorrected and corrected Strouhal number as a function of the model angle of attack at Reynolds number R_e = 26600

Parabolic model

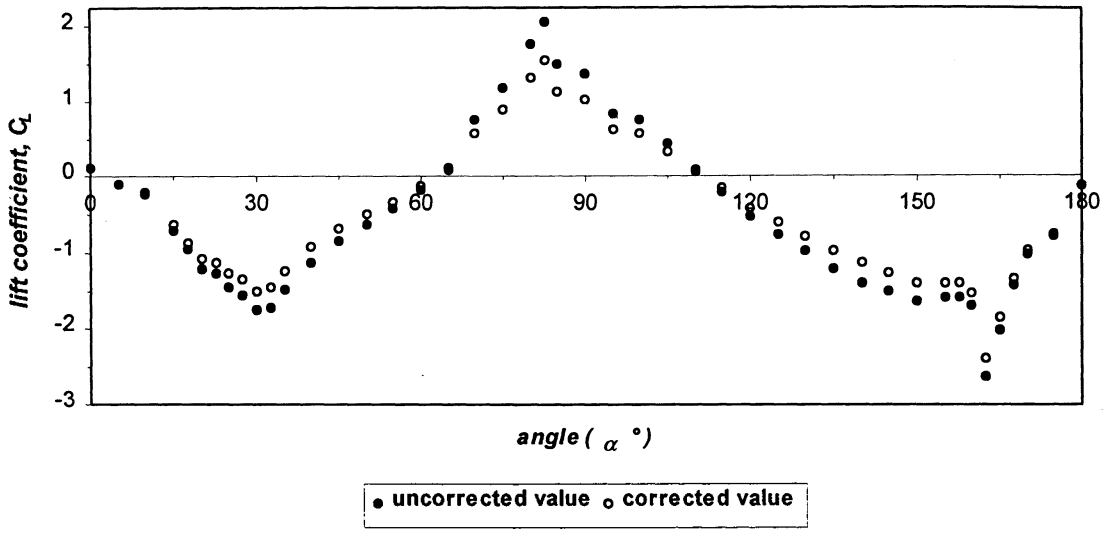

Figure A4.10

Uncorrected and corrected lift coefficient as a function of the model angle of attack at Reynolds number R_e = 26600

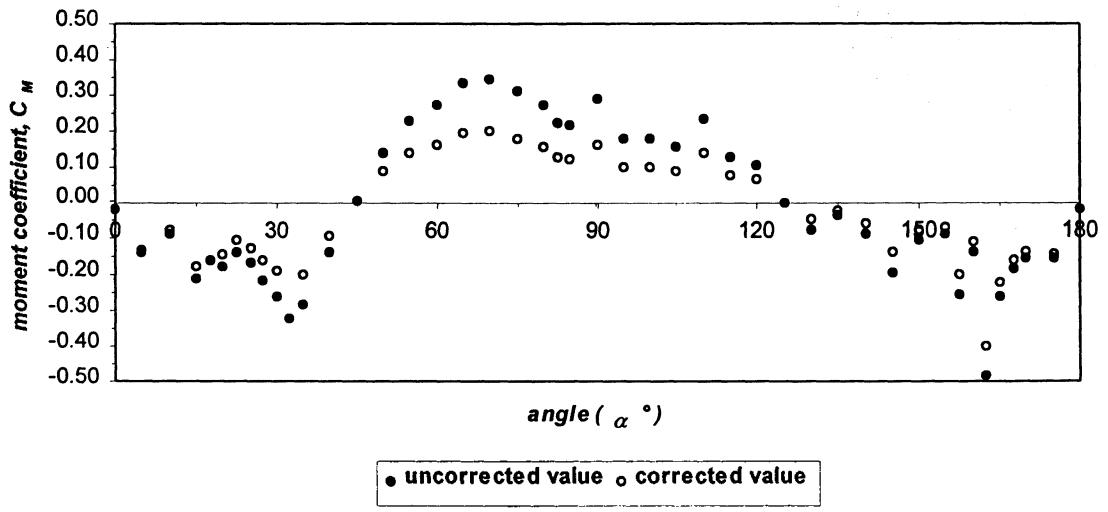

Figure A4.11

Uncorrected and corrected moment coefficient as a function of the model angle of attack at Reynolds number R_e = 26600

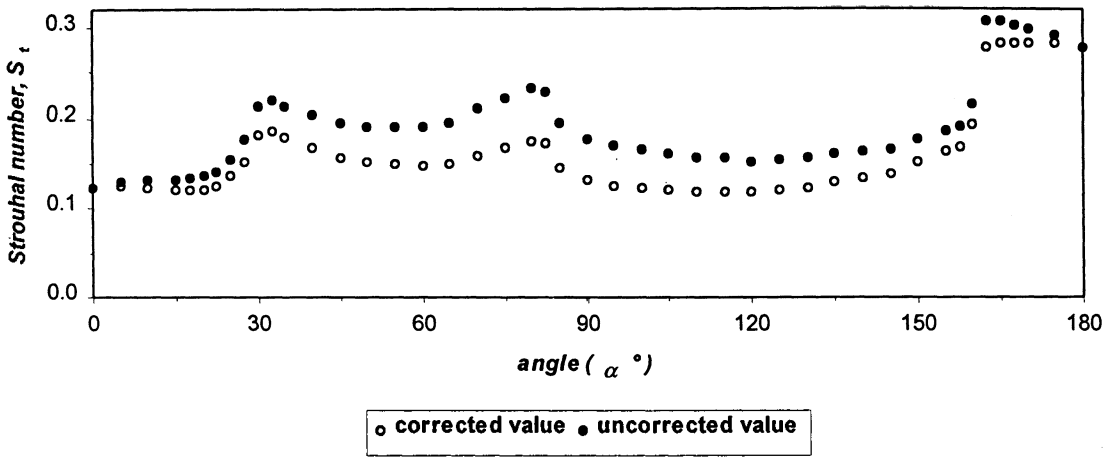

Figure A4.12

Uncorrected and corrected Strouhal number as a function of the model angle of attack at Reynolds number R_e = 26600

Appendix V - Finite element analysis of the mixing blade

Detecting mixing blade dynamic response in the sealed environment of the vessel is almost impossible. However, the mixing blade dynamic characteristics, like mode shapes and frequencies, may provide some answers for the cause of blade failure. Simulation was used to estimate these characteristics. Using software package IDEAS, mixing blade structure was replicated and finite element analysis performed on it. The blade structure was approximated using shell elements, while supporting strut at the end of the blade was approximated with beam elements, as presented in ***Figure A5.1***. The mixing blade model was mashed and constrained conditions were applied. In the ***Figure A5.2***, constrains are presented as arrows. Each point that represents contact between blade and supporting blade (see ***Figure 1.2***) was constrained from moving or rotating in any direction. The model mesh size used in the first iteration was 0.1 m. In each consequent iteration, mesh size was decreased. Finite element analysis was repeated four

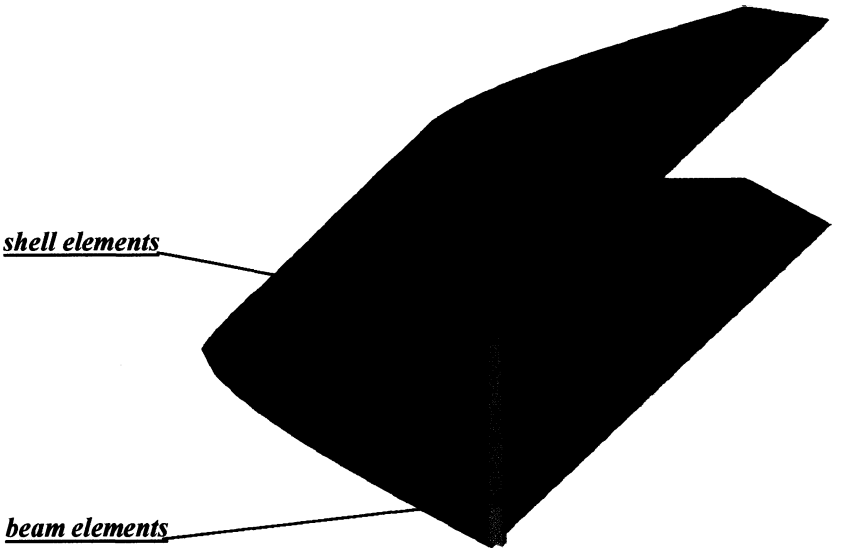

Figure A5.1

Simulation model of the mixing blade

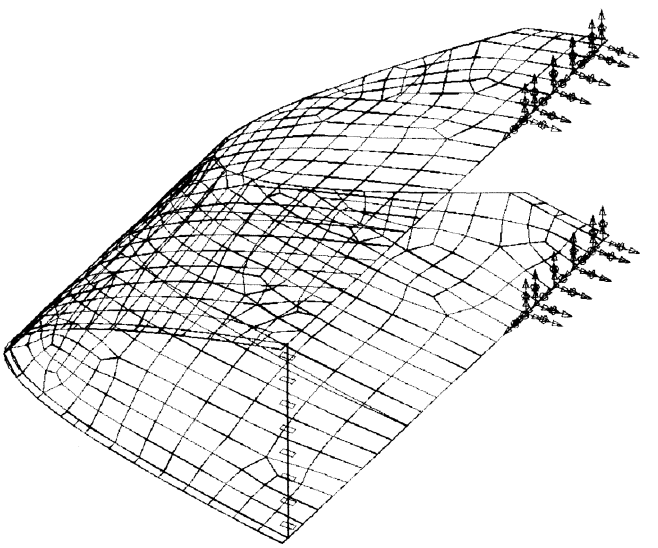

Figure A5.2

Finite element model of the mixing blade

times. With each iteration, results converged closer to a value that would be calculated if the mesh size was infinitivally small. The iteration process stopped when difference between last two calculated values became less then 1%. Model mesh size of maximum 0.02 m per element was presented in ***Figure A5.2.***

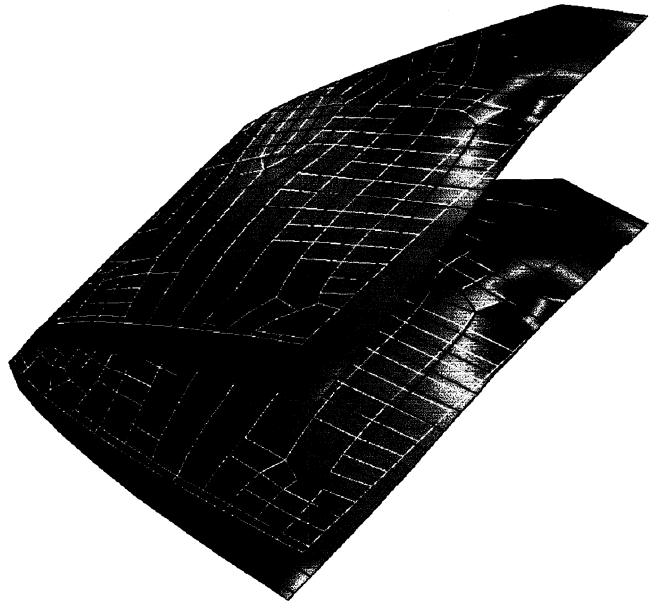

Figure A5.3

First oscillating mode, frequency 30 Hz

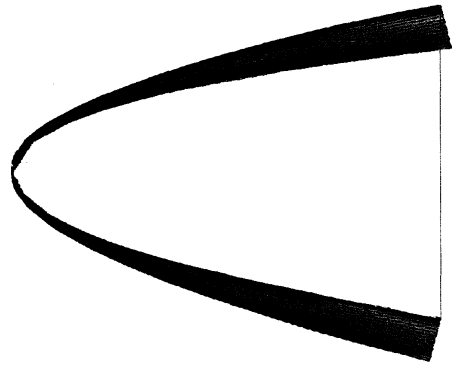

Figure A5.4

Side view of the first oscillating mode, frequency 30 Hz

Results of the simulation are presented in ***Figures A5.3-6***. In ***Figure A5.3*** and ***Figure A5.4***, the first mode shape with frequency of 30 Hz is depicted. The first mode is torsion of the blade around the shear centre. Change in stress is represented as a change in colour. Blue colour represent areas with low stress and red colour marks high stress areas. High stress area is concentrated at of the constrained part of the blade. The position of the high stress area coincides with the position where first cracks occurred, causing the failure of the mixing blade. Stress distribution acquired with finite element dynamic analysis confirmed that breakage of the blade is caused by excessive vibrations. In ***Figure A5.5*** and ***Figure A5.6*** second and third vibration modes are presented with frequency 77 Hz and 99 Hz respectively.

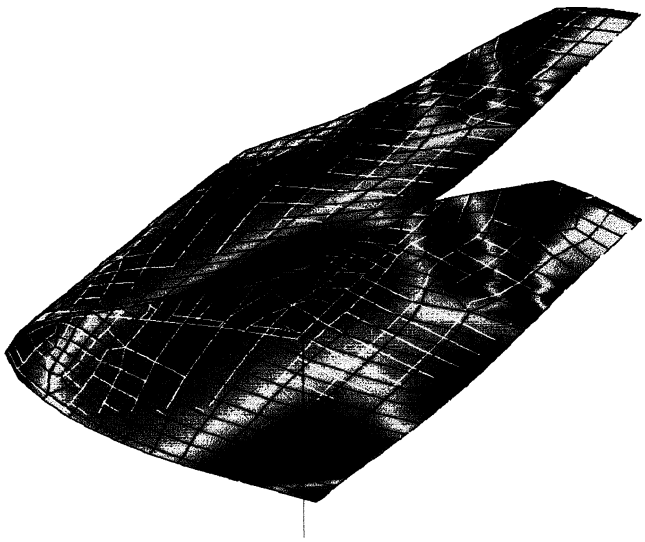

Figure A5.5

Second oscillating mode, frequency 77 Hz

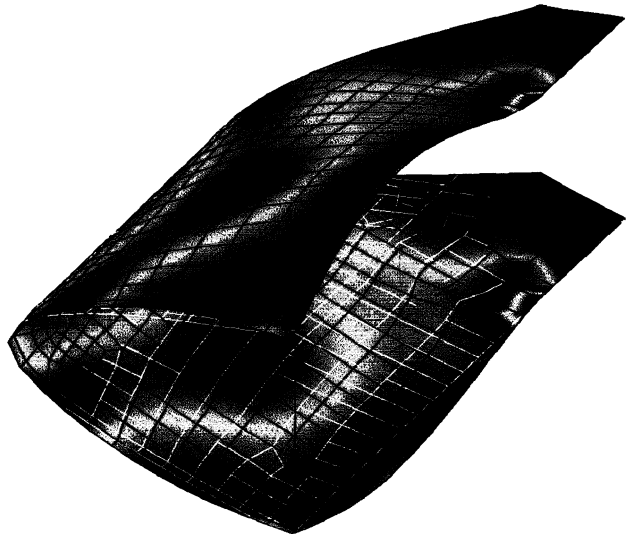

Figure A5.6

Third oscillating mode, frequency 99 Hz

Same software package was used to calculate the shear centre position for the mixing blade parabolic cross-section. Shear centre was calculated to be 0.113 m from the tip of the blade. For the parabolic cross-section model used in the experiments, location of the shear centre corresponds to the elastic axis position of 62 mm behind the model centre of gravity.

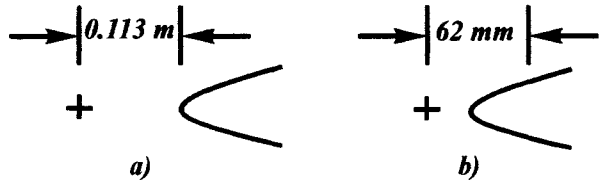

Figure A5.7

Location of the mixing blade shear centre and corresponding position of the model elastic axis from the model centre of gravity: a) shear centre position of the parabolic cross-section, b) elastic axis position in the experimental set-up

Appendix VI - Test section drawings with dimensions

Test set-up drawings are included in this Appendix. Basic dimensions are given and parts of the experimental set-up are marked in all figures. ***Figure A6.1*** depicts test set-up front view, while ***Figure A6.2*** and ***Figure A6.3*** present test set-up top view with the model elastic axis coinciding with the model centre of gravity and the model elastic axis 95 mm behind the model centre of gravity, respectively.

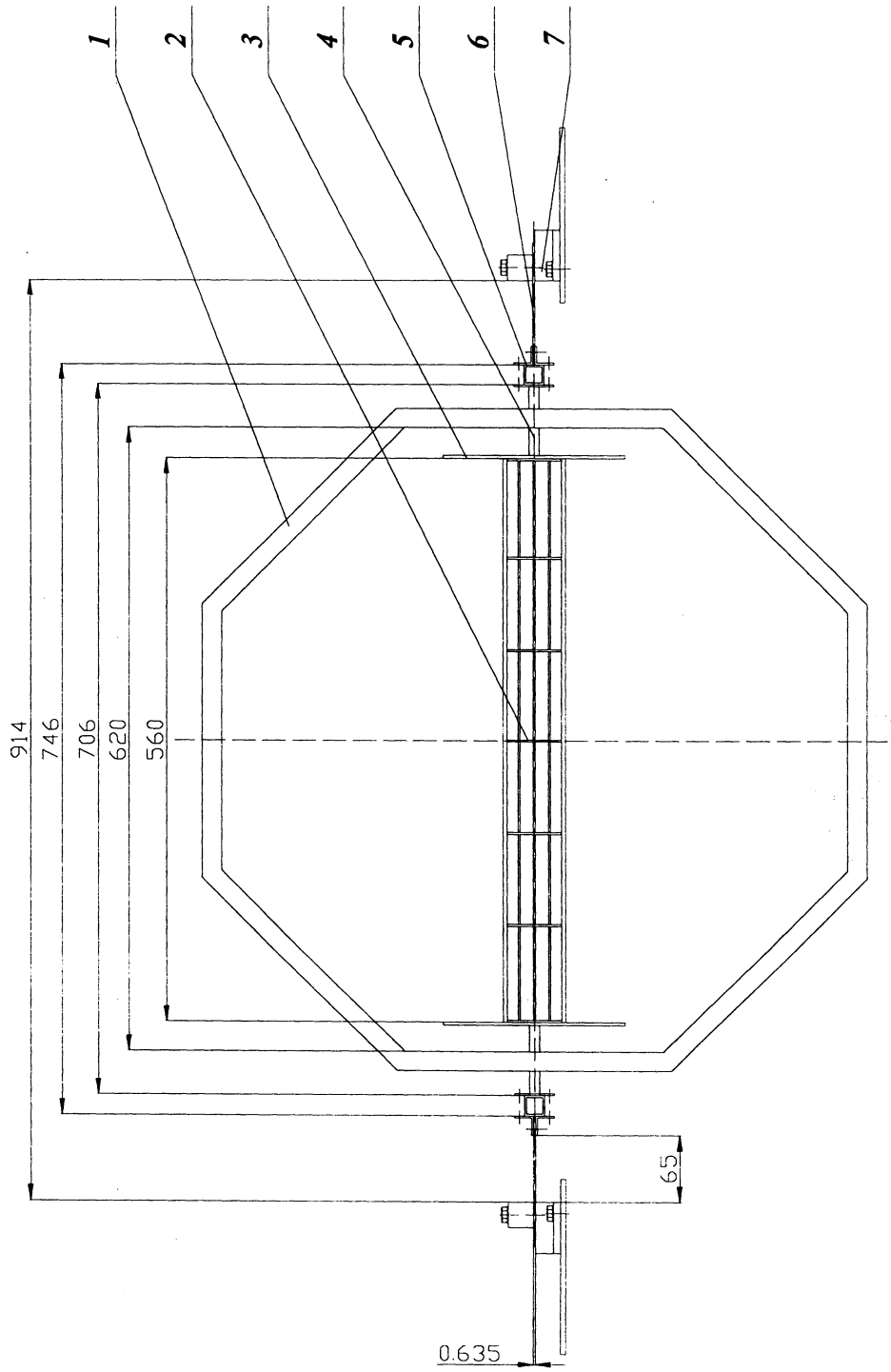

Test set-up front view

1 - test section, 2 - test model, 3 - endplate, 4 - connecting rod, 5 - support, 6 - elastic beams, 7 - rigid support

Figure A6.1

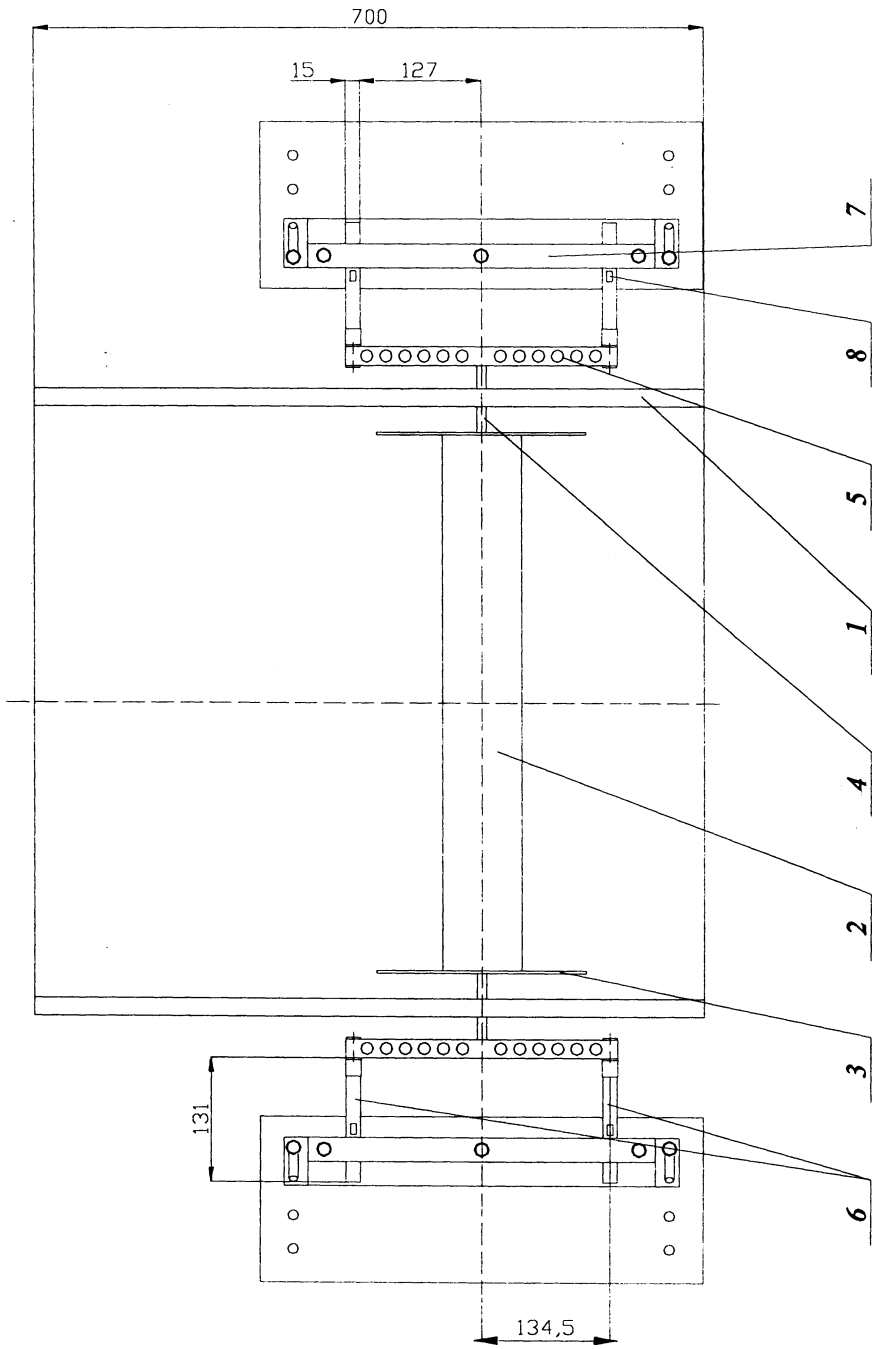

Test set-up top view
centre of gravity coincides with elastic axis
1 - test section, 2 - test model, 3 - endplate, 4 - connecting rod,
5 - support, 6 - elastic beams, 7 - rigid support, 8 - strain gauge

Figure A6.2

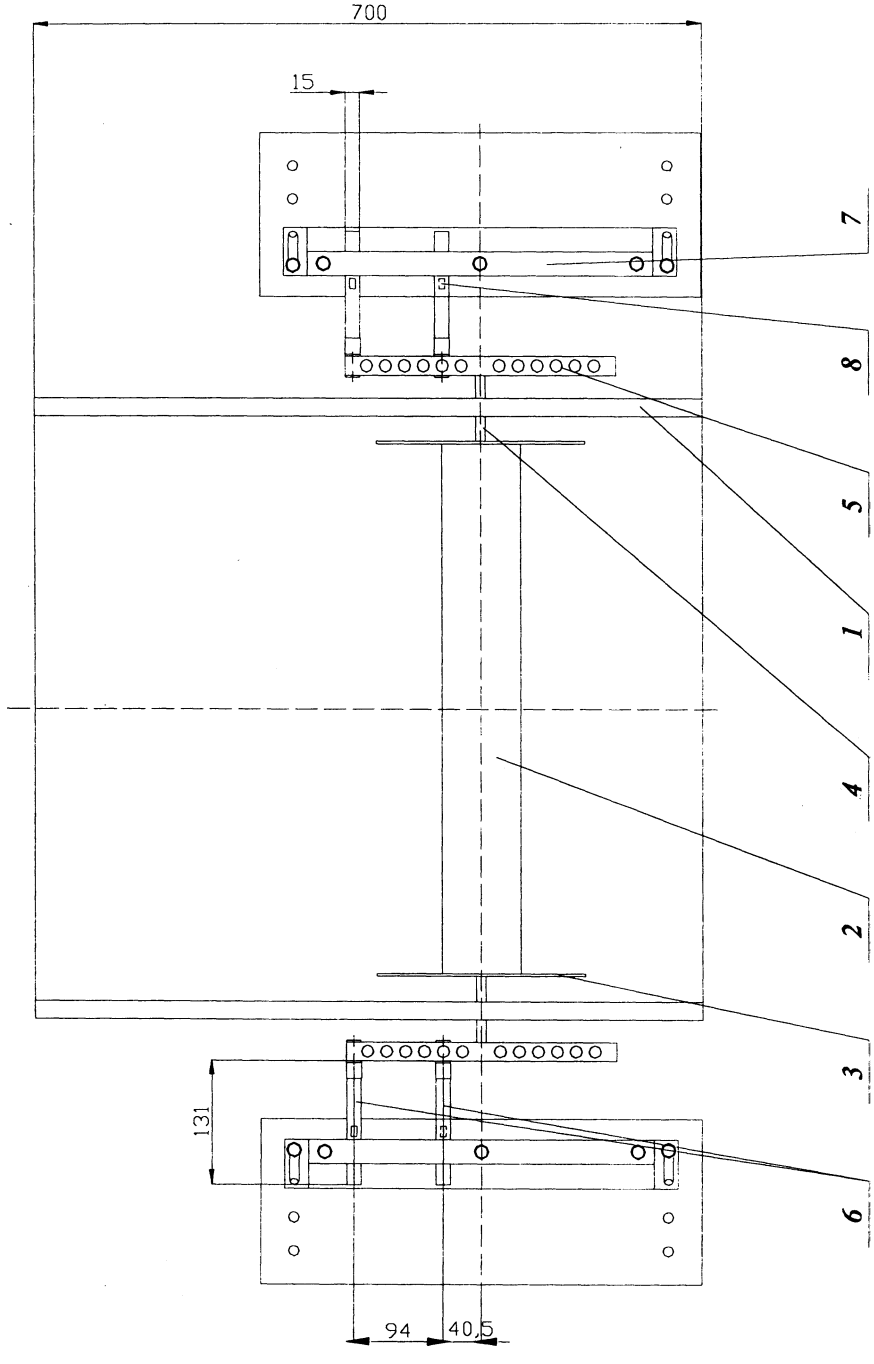

Test set-up top view
elastic axis 95 mm behind the centre of gravity
1 - test section, 2 - test model, 3 - endplate, 4 - connecting rod,
5 - support, 6 - elastic beams, 7 - rigid support, 8 - strain gauge

Figure A6.3

Appendix VII – Photographs of the models and experimental set-up

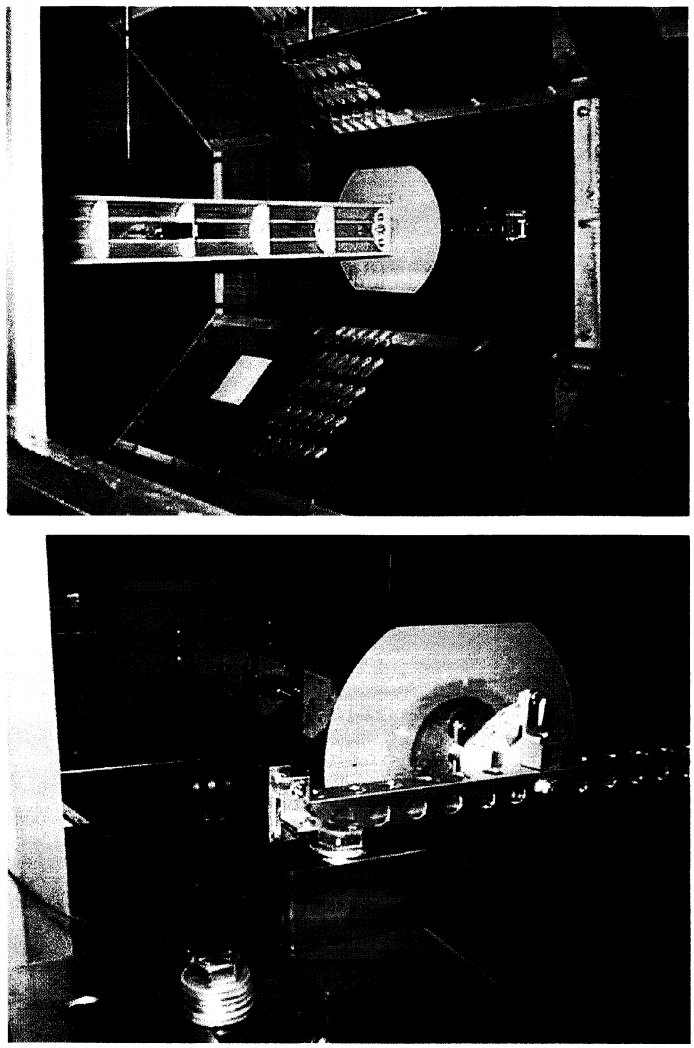

Figure A7.1

The semi-circular cross-section model in the wind tunnel

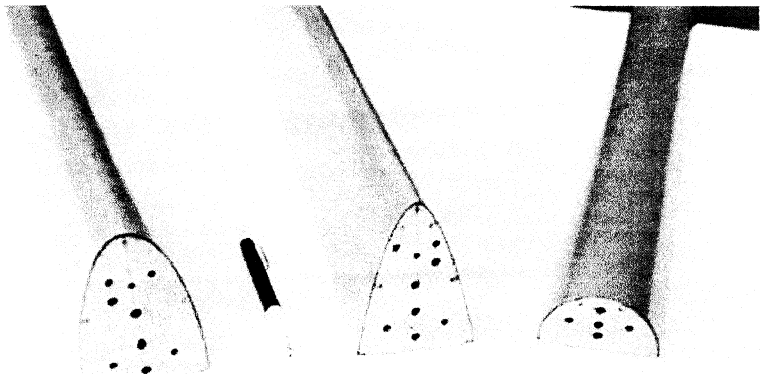

Figure A7.2

The test models used in experiments

References

Bearman, P., W., 1984, "Vortex Shedding from Oscillating Bluff Bodies", *Annual Review of Fluid Mechanics*, vol. 16, pp. 195-222.

Blevins, R., D., 1990, " Flow-Induced Vibrations", 2nd edition, New York, Van Nostrand Reinhold, USA.

Bokaian, A., Geoola, F., 1984, "Effects on Vortex-Resonance on Nearby Galloping Instability", *ASCE Journal of Engineering Mechanics*, vol. 111, pp. 591-609

Corless, R., M., Parkinson, G., V., 1988, " A Model of the Combined Effects of the Vortex-Induced Oscillation and Galloping", *Journal of Fluids and Structures*, vol. 2, pp. 203-220.

Dally, J., W., Riley, W., F., McConnell, K., G., 1993, "Instrumentation for Engineering Measurements", John Wiley & Sons, Inc., USA.

den Hartog, J., P., 1956, "Mechanical Vibrations", McGraw-Hill, New York, USA.

HP 35670A Operator's guide, Decembre 1992, Hewlet-Packard Company, WA, USA.

Kubo, Y., Miyazaki, M., Kato, K., 1989, "Effects of End Plates and Blockage of Structural Members on Drag Forces", *Journal of Wind Engineering and Industrial Aerodynamics*, vol. 32, pp. 329-342.

Modi V. J., Slater J. E., 1983, "Unsteady Aerodynamics and Vortex Induced Aeroelastic Instability of a Structural Angle Section", *Journal of Wind Engineering and Industrial Aerodynamics*, vol. 11, pp. 321-334.

Modi V. J., Slater J. E., 1994, "Unsteady Aerodynamics and Vortex-Induced Aeroelastic Response of a Structural Angle Section", *Journal of Vibration and Acoustics*, vol. 116, pp. 449-456.

Naudascher, E. Rockwell, D., 1994, "Flow-Induced Vibrations: an Engineering Guide", A. A. Balkema, Rotterdam.

Novak, M., Davenport, A., G., 1970, "Aeroelastic Instability of the Prisms in Turbulent Flow", *ASCE Journal of the Engineering Mechanics Division*, vol. 96, pp. 17-39.

Novak, M., 1972, Galloping oscillations of prismatic structures", *ASCE Journal of the Engineering Mechanics Division*, vol. 98, pp, 27-46.

Novak, M., Tanaka, H., 1974, "Effect of the Turbulence on the Galloping Instability", *ASCE Journal of the Engineering Mechanics Division*, vol. 100, pp. 27-47.

Parkinson, G., V., 1989, "Phenomena and Modelling of Flow-Induced Vibrations of Bluff Bodies", *Progress in Aerospace Science*, vol. 26, pp. 169-224.

Parkinson, G., V., Smith, J., D., 1964, "The Square Prism as an Aeroelastic Non-Linear Oscillator", *Quarterly Journal of Mechanics and Applied Mathematics*, vol. 17, pp. 225-239.

Parkinson, G., V., Brooks, N., P., H., 1961, "On the Aeroelastic Instability of Bluff Cylinders", *Journal of Applied Mechanics*, vol. 28, pp. 252-258.

Stansby, P.K., 1974, "The Effects of End Plates on the Base Pressure Coefficient of a Circular Cylinder", *Aeronautical Journal*, vol. 78, pp. 36-37.

United Sensors, "Probes for measuring velocity and flow direction – Pitot static pressure probe" United Sensor Corporation, Bulletin 1, 6 – 83, Amherst NH, USA.

Weaver, D., S., 2000, ME 327 Course Notes, Hamilton, Canada

Window, A., L., Holister, G., S., 1982, "Strain Gauge Technology" Applied Science Publishers, New Jersey, USA